

AD-A194 981

CONFIRMATION OF SLOW-WAVES IN A CROSSTIE OVERLAY
COPLANAR WAVEGUIDE AND I.. (U) TEXAS UUVY AT AUSTIN DEPT
OF ELECTRICAL AND COMPUTER ENGINEER. T HANG ET ALL

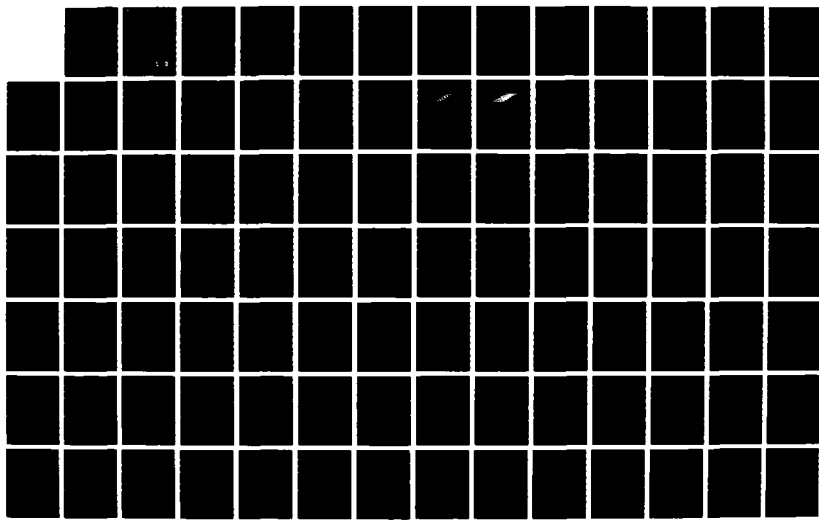
1/2

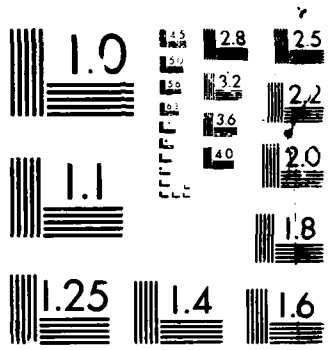
UNCLASSIFIED

MAR 88 ARO-25845. 1-EL DAAL03-88-K-0005

F/G 9/1

NL





MICROGRAPH RESOLUTION TEST CHART
NATIONAL BUREAU OF STANDARDS 1963

DTIC EFILE COPY

ARO 25045.1-EL

(2)

AD-A194 981

MICROWAVE LABORATORY REPORT NO. 88-P-1

CONFIRMATION OF SLOW-WAVES IN A CROSSTIE OVERLAY
COPLANAR WAVEGUIDE AND ITS APPLICATIONS TO
BAND-REJECT GRATINGS AND REFLECTORS

TECHNICAL REPORT

TE-HUI WANG
and

Tatsuo Itoh

MARCH 1988

ARMY RESEARCH OFFICE
CONTRACT DAAL 03-88-K-0005

THE UNIVERSITY OF TEXAS
DEPARTMENT OF ELECTRICAL ENGINEERING
AUSTIN, TEXAS 78712

APPROVED FOR PUBLIC RELEASE
DISTRIBUTION UNLIMITED

DTIC
SELECTED
MAY 10 1988
S **D**
H

88 5 10 164

UNCLASSIFIED

MASTER COPY

FOR REPRODUCTION PURPOSES

SECURITY CLASSIFICATION OF THIS PAGE

REPORT DOCUMENTATION PAGE

1a. REPORT SECURITY CLASSIFICATION Unclassified		1b. RESTRICTIVE MARKINGS	
2a. SECURITY CLASSIFICATION AUTHORITY		3 DISTRIBUTION/AVAILABILITY OF REPORT Approved for public release; distribution unlimited.	
2b. DECLASSIFICATION/DOWNGRADING SCHEDULE			
4. PERFORMING ORGANIZATION REPORT NUMBER(S) Microwave Laboratory Report No. 88-P-1		5 MONITORING ORGANIZATION REPORT NUMBER(S) ARO 25045.1-E4	
6a. NAME OF PERFORMING ORGANIZATION The University of Texas	6b OFFICE SYMBOL (If applicable)	7a. NAME OF MONITORING ORGANIZATION U. S. Army Research Office	
6c. ADDRESS (City, State, and ZIP Code) Dept. of Electrical and Computer Engineering Austin, Texas 78712	7b. ADDRESS (City, State, and ZIP Code) P. O. Box 12211 Research Triangle Park, NC 27709-2211		
8a. NAME OF FUNDING/SPONSORING ORGANIZATION U. S. Army Research Office	8b. OFFICE SYMBOL (If applicable)	9 PROCUREMENT INSTRUMENT IDENTIFICATION NUMBER Contract DAAL 03-88-K-0005	
8c. ADDRESS (City, State, and ZIP Code) P. O. Box 12211 Research Triangle Park, NC 27709-2211		10 SOURCE OF FUNDING NUMBERS	
		PROGRAM ELEMENT NO	PROJECT NO
		TASK NO	WORK UNIT ACCESSION NO
11 TITLE (Include Security Classification) Confirmation of Slow-Waves in a Crosstie Overlay Coplanar Waveguide and Its Applications to Band-Reject Gratings and Reflectors			
12 PERSONAL AUTHOR(S) Te-Hui Wang and Tatsuo Itoh			
13a. TYPE OF REPORT Technical	13b. TIME COVERED FROM _____ TO _____	14. DATE OF REPORT (Year, Month, Day) March 1988	15 PAGE COUNT 155
16. SUPPLEMENTARY NOTATION The view, opinions and/or findings contained in this report are those of the author(s) and should not be construed as an official Department of the Army position, policy, or decision unless so designated by other documentation			
17 COSATI CODES		18. SUBJECT TERMS (Continue on reverse if necessary and identify by block number) Crosstie overlay coplanar waveguide, Band-reject gratings, Ohmic loss, Incremental inductance rule, Slow-wave	
19 ABSTRACT (Continue on reverse if necessary and identify by block number) The slow-wave propagation along a new crosstie overlay slow-wave coplanar waveguide has been investigated both theoretically and experimentally. A slow-wave factor observed agrees reasonably well with the theoretical prediction. This structure is used from construction of a frequency-selective distributed Bragg reflectors (DBR's) with a compact size. The effect of conductor loss is considered. A doubly-periodic band-reject grating has been created from the DBR's and the band-reject phenomenon was observed as predicted. To improve passband characteristics of the grating, a monolithic slow-wave Chebyshev reflector was designed and fabricated. Agreement between theory and preliminary experiment has been confirmed. Based on this theory, a new slow-wave reflector with improved characteristics is proposed and examined. A respectable slow-wave factor and a drastic reduction of conductor loss have been obtained.			
20. DISTRIBUTION/AVAILABILITY OF ABSTRACT <input checked="" type="checkbox"/> UNCLASSIFIED/UNLIMITED <input type="checkbox"/> SAME AS RPT <input type="checkbox"/> DTIC USERS		21. ABSTRACT SECURITY CLASSIFICATION Unclassified	
22a. NAME OF RESPONSIBLE INDIVIDUAL Tatsuo Itoh		22b. TELEPHONE (Include Area Code) (512) 471-1072	22c. OFFICE SYMBOL

MICROWAVE LABORATORY REPORT NO. 88-P-1

CONFIRMATION OF SLOW-WAVES IN A CROSSTIE OVERLAY
COPLANAR WAVEGUIDE AND ITS APPLICATIONS TO
BAND-REJECT GRATINGS AND REFLECTORS

TECHNICAL REPORT

TE-HUI WANG
and

Tatsuo Itoh

MARCH 1988

ARMY RESEARCH OFFICE

CONTRACT DAAL 03-88-K-0005

THE UNIVERSITY OF TEXAS
DEPARTMENT OF ELECTRICAL ENGINEERING
AUSTIN, TEXAS 78712

APPROVED FOR PUBLIC RELEASE
DISTRIBUTION UNLIMITED

CONFIRMATION OF SLOW-WAVES IN A CROSSTIE OVERLAY COPLANAR WAVEGUIDE AND ITS APPLICATIONS TO BAND-REJECT GRATINGS AND REFLECTORS

The slow-wave propagation along a new crosstie overlay slow-wave coplanar waveguide has been investigated both theoretically and experimentally. A slow-wave factor observed agrees reasonably well with the theoretical prediction. This structure is used for construction of a frequency-selective distributed Bragg reflectors (DBR's) with a compact size. The effect of conductor loss is considered. A doubly-periodic band-reject grating has been created from the DBR's and the band-reject phenomenon was observed as predicted. To improve passband characteristics of the grating, a monolithic slow-wave Chebyshev reflector was designed and fabricated. Agreement between theory and preliminary experiment has been confirmed. Based on this theory, a new slow-wave reflector with improved characteristics is proposed and examined. A respectable slow-wave factor and a drastic reduction of conductor loss have been obtained.



Accession For	
NTIS GRA&I	<input checked="" type="checkbox"/>
DTIC TAB	<input type="checkbox"/>
Unannounced	<input type="checkbox"/>
Justification	
By _____	
Distribution/ _____	
Availability Codes	
Dist	Avail and/or Special
A-1	

TABLE OF CONTENTS

	<u>Page</u>
LIST OF FIGURES	ix
LIST OF TABLES	xv
CHAPTER	
1 INTRODUCTION	1
1.1 Background and objectives	1
1.2 Thesis organization	9
2 CROSSTIE OVERLAY SLOW-WAVE COPLANAR WAVEGUIDE	10
2.1 Transmission line candidates for new slow-wave mechanism implementation	10
2.2 Slow-wave principle and waveguide structure for the new crosstie overlay slow-wave coplanar waveguide	12
2.3 Formulation of spectral domain analysis	13
2.3.1 Propagation constant	14
2.3.2 Characteristic impedance	34

2.3.3	Choice of basis functions	36
2.4	Floquet's theorem and a periodic crosstie overlay slow-wave coplanar waveguide	40
2.5	Propagation characteristics of a crosstie overlay slow-wave coplanar waveguide with lossless conductors	44
2.5.1	General dispersive characteristics of the constituent sections	45
2.5.2	Effects of the cross-sectional configuration of a coplanar waveguide and the thickness of the dielectric overlay	45
2.5.3	Effect of substrate thickness	52
2.5.4	Effect of the lengths of the constituent sections	58
2.6	Conductor loss estimation	63
2.7	Propagation characteristics of a crosstie overlay slow-wave coplanar waveguide with lossy conductors	72
2.8	Experimental confirmation of slow-wave propagation in a crosstie overlay coplanar waveguide	82
3	A BAND-REJECT GRATING MADE OF CROSSTIE OVERLAY SLOW-WAVE COPLANAR WAVEGUIDES	93

3.1 A doubly-periodic grating structure and the transmission-line equivalent circuit	95
3.2 Characterization of the reflection and transmission properties of a band-reject grating	97
3.3 Predicted characteristics of a band-reject grating	102
3.4 Experimental results for a band-reject grating	108
4 SLOW-WAVE CHEBYSHEV REFLECTOR DESIGN USING NEW CROSSTIE OVERLAY SLOW-WAVE COPLANAR WAVEGUIDES	117
4.1 Synthesis of slow-wave Chebyshev reflector prototypes	117
4.2 Realization of a slow-wave Chebyshev reflector from a transmission-line prototype	128
4.3 Preliminary experimental results for the slow-wave Chebyshev reflector	132
4.4 A modified crosstie overlay slow-wave coplanar waveguide and its application to a new slow-wave Chebyshev reflector	137
4.5 Predicted characteristics of the new slow-wave Chebyshev reflector	138

5	CONCLUSIONS	146
5.1	Achievements	146
5.2	Suggestions for future work	147

LIST OF FIGURES

	<u>Page</u>
Fig.1.1 MIS slow-wave structures. (a) MIS microstrip line, (b) MIS coplanar waveguide.	2
Fig.1.2 Schottky contact slow-wave structures. (a) Schottky microstrip line, (b) Schottky coplanar waveguide.	4
Fig.1.3 Crosstie coplanar waveguide (CTCPW) slow-wave structure (by Hasegawa).	5
Fig.1.4 Crosstie overlay CPW and microstrip slow-wave structures. (a) CPW, (b) Cross-section of CPW, (c) Cross-section of microstrip.	6
Fig.2.1 Transmission lines in MMIC's. (a) Microstrip, (b) Slotline, (c) Coplanar waveguide, (d) Coplanar strips.	11
Fig.2.2 Cross-sectional view of general constituent sections in the crosstie overlay slow-wave coplanar waveguide.	15
Fig.2.3 Coordinate transformation.	29
Fig.2.4 Transverse equivalent circuits for crosstie overlay CPW.	30
Fig.2.5 Field distribution of the first four basis functions.	39
Fig.2.6 Periodic transmission line model of a crosstie overlay slow-wave CPW.	41
Fig.2.7(a) Normalized propagation constant versus frequency of sections A and B in a crosstie overlay slow-wave CPW.	46
Fig.2.7(b) Characteristic impedance versus frequency of sections A and B in a crosstie overlay slow-wave CPW.	47

Fig.2.8(a) Normalized propagation constant versus aspect ratio of Section A with different overlay thicknesses.	48
Fig.2.8(b) Characteristic impedance versus aspect ratio of Section A with different overlay thicknesses.	49
Fig.2.9(a) Normalized propagation constant versus aspect ratio of Section B with different overlay thicknesses.	50
Fig.2.9(b) Characteristic impedance versus aspect ratio of Section B with different overlay thicknesses.	51
Fig.2.10(a) Normalized propagation constant versus aspect ratio of Section A with different substrate thicknesses.	53
Fig.2.10(b) Characteristic impedance versus aspect ratio of Section A with different substrate thicknesses.	54
Fig.2.11(a) Normalized propagation constant versus aspect ratio of Section B with different substrate thicknesses.	55
Fig.2.11(b) Characteristic impedance versus aspect ratio of Section B with different substrate thicknesses.	56
Fig.2.12 Slow-wave factor versus aspect ratio of crosstie overlay slow- wave CPWs with different overlay thicknesses.	57
Fig.2.13(a) Slow-wave factor versus aspect ratio of crosstie overlay slow- wave CPWs with different substrate thicknesses.	59
Fig.2.13(b) Characteristic impedance versus aspect ratio of crosstie overlay slow-wave CPWs with different substrate thicknesses.	60

Fig.2.14(a) Slow-wave factor versus frequency of crosstie overlay slow-wave CPWs with different periodicities.	61
Fig.2.14(b) Characteristic impedance versus frequency of crosstie overlay slow-wave CPWs with different periodicities.	62
Fig.2.15 Slow-wave factor versus duty cycle of crosstie overlay slow-wave CPWs with different overlay thicknesses.	64
Fig.2.16 Recession of conducting walls of crosstie overlay slow-wave CPW. (a) Section A, (b) Section B using "Incremental Inductance Rule".	66
Fig.2.17(a) Ohmic attenuation constant versus aspect ratio of Section A with different overlay thicknesses ($A_u=1.5\mu m$).	73
Fig.2.17(b) Ohmic attenuation constant versus aspect ratio of Section A with different overlay thicknesses ($A_u=3.0\mu m$).	74
Fig.2.18(a) Ohmic attenuation constant versus aspect ratio of Section B with different overlay thicknesses ($A_u=1.5\mu m$).	75
Fig.2.18(b) Ohmic attenuation constant versus aspect ratio of Section B with different overlay thicknesses ($A_u=3.0\mu m$).	76
Fig.2.19 Ohmic attenuation constant of crosstie overlay slow-wave CPW with different overlay thicknesses.	78
Fig.2.20 Quality factor versus aspect ratio of crosstie overlay slow-wave CPWs with different overlay thicknesses.	79
Fig.2.21 Ohmic attenuation constant versus duty cycle of crosstie	

overlay slow-wave CPWs with different overlay thicknesses.	80
Fig.2.22 Quality factor versus duty cycle of crosstie overlay slow-wave CPWs with different overlay thicknesses.	81
Fig.2.23(a) Ohmic attenuation constant versus aspect ratio of Section A with different cross-sectional sizes of CPWs.	83
Fig.2.23(b) Ohmic attenuation constant versus aspect ratio of Section B with different cross-sectional sizes of CPWs.	84
Fig.2.24(a) Slow-wave factor versus aspect ratio of crosstie overlay slow- wave CPWs with different cross-sectional sizes of CPWs.	85
Fig.2.24(b) Ohmic attenuation constant versus aspect ratio of crosstie overlay slow-wave CPWs with different cross-sectional sizes of CPWs.	86
Fig.2.25 Quality factor versus aspect ratio of crosstie overlay slow-wave CPWs with different cross-sectional sizes of CPWs.	87
Fig.2.26 Photograph of the disassembled crosstie overlay slow-wave CPW in experiment.	89
Fig.2.27 Slow-wave factor versus frequency for a crosstie overlay slow-wave CPW.	90
Fig.2.28 Attenuation constant versus frequency for a crosstie overlay slow-wave CPW.	91
Fig.3.1 K- β diagram of a grating structure. (a) Wave coupling neglected, (b) Surface-wave stopband.	94
Fig.3.2 Schematic and equivalent circuit of doubly-periodic band-reject grating.	96

Fig.3.3 Transmission line equivalent circuit for characterizing transmission and reflection properties of a symmetrical doubly-periodic band-reject grating.	98
Fig.3.4 Impedance transforms for input impedance calculation for a doubly- periodic band-reject grating.	101
Fig.3.5(a) Insertion loss and return loss of a doubly-periodic band-reject grating with lossless conductors and 5.5 periods.	103
Fig.3.5(b) Insertion loss and return loss of a doubly-periodic band-reject grating with lossless conductors and 7.5 periods.	104
Fig.3.5(c) Insertion loss and return loss of a doubly-periodic band-reject grating with lossless conductors and 9.5 periods.	105
Fig.3.6(a) Real part of the input impedance of a doubly-periodic band-reject grating with lossless conductors and 9.5 periods.	106
Fig.3.6(b) Imaginary part of the input impedance of a doubly-periodic band-reject grating with lossless conductors and 9.5 periods.	107
Fig.3.7(a) Insertion loss of a doubly-periodic band-reject grating with lossy conductors and 9.5 periods.	109
Fig.3.7(b) Return loss of a doubly-periodic band-reject grating with lossy conductors and 9.5 periods.	110
Fig.3.8(a) Real part of the input impedance of a doubly-periodic band-reject grating with lossy conductors and 9.5 periods.	111
Fig.3.8(b) Imaginary part of the input impedance of a doubly-periodic band-reject grating with lossy conductors and 9.5 periods.	112

Fig.3.9 Photograph of the disassembled doubly-periodic band-reject grating in experiment.	113
Fig.3.10 Measured and calculated insertion loss for the doubly-periodic band-reject grating.	115
Fig.3.11 Measured and calculated return loss for the doubly-periodic band-reject grating.	116
Fig.4.1 Equal-electrical-length step-impedance transmission-line equivalent circuit for slow-wave Chebyshev reflector prototype.	118
Fig.4.2 Idealized attenuation response for a slow-wave Chebyshev reflector.	120
Fig.4.3 Photograph of the slow-wave Chebyshev reflector. (a) Device chip, (b) Device and test jig.	134
Fig.4.4 Insertion loss of the preliminary slow-wave Chebyshev reflector.	135
Fig.4.5 Return loss of the preliminary slow-wave Chebyshev reflector.	136
Fig.4.6 Modified crosstie overlay CPW and microstrip slow-wave structures. (a) CPW, (b) Cross-section of CPW, (c) Cross-section of microstrip.	139
Fig.4.7 Predicted insertion loss of the modified slow-wave Chebyshev reflector.	142
Fig.4.8 Predicted return loss of the modified slow-wave Chebyshev reflector.	143
Fig.4.9 Real part of the input impedance of the modified slow-wave Chebyshev reflector.	144
Fig.4.10 Imaginary part of the input impedance of the modified slow-wave Chebyshev reflector.	145

LIST OF TABLES

	<u>Page</u>
Table 4.1 Detailed information for Z, l _A , l _B and L of the slow-wave Chebyshev reflector and quarter-wave impedance transformer	133
Table 4.2 Detailed information for Z, l _A , l _B and L of the modified slow-wave Chebyshev reflector.	143

CHAPTER 1: INTRODUCTION

1.1 BACKGROUND AND OBJECTIVES

Circuit integration at microwave frequencies is based on the use of (1) planar transmission lines as the transmission medium, (2) distributed circuit elements or lumped elements in planar form, (3) microwave solid-state devices compatible with the planar transmission lines, and (4) hybrid technology, particularly thin-film techniques, for fabrication. With these features, microwave integrated circuits (MIC's) offer several advantages over waveguide and coaxial circuits - namely, reduction in size and weight, ease of mass production with improved reproducibility, and potentially lower cost. Monolithic microwave integrated circuits (MMIC's) technology offers the further advantage of combining multicircuit functions without any interconnecting wires, thus permitting compact integrated modules with highly reliable performance.

Recently, remarkable progress has been achieved in GaAs MMIC's [1]. In MMIC design, one of the most important things is to minimize the monolithic circuit size. The conventional printed line circuits cannot reduce the guide wavelength λ_g by more than $\sqrt{\epsilon_r}$ (ϵ_r is the relative dielectric constant of the transmission medium) from free space wavelength λ_0 . A slow-wave transmission line provides a possible remedy. MIS slow-wave microstrip line introduced by Hasegawa [2] and MIS coplanar waveguide (CPW) [3],[4] have the capability to realize a slow-wave factor λ_0/λ_g (or β/β_0 , where β and β_0 are the phase constants in the waveguide and in free space, respectively) of more than 20 (Fig.1.1). Similar wavelength reduction can be

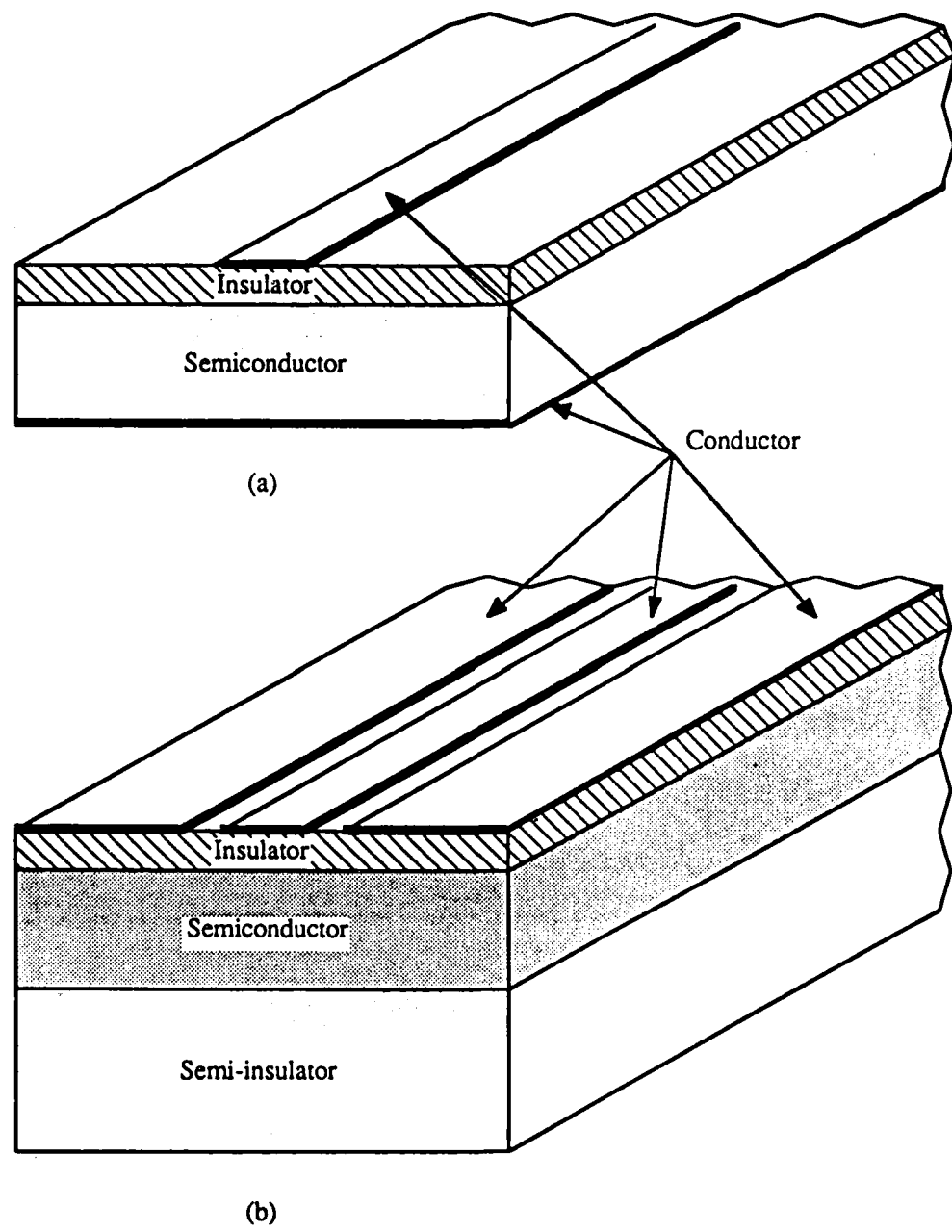


Fig.1.1 MIS slow-wave structures. (a) MIS microstrip line, (b) MIS coplanar waveguide.

realized by a Schottky contact microstrip line and CPW [3],[5] (Fig.1.2). The Schottky contact structures have an added advantage that the slow-wave factor can be controlled by the dc bias applied to the wave-propagating electrode. More recently, a CPW slow-wave structure with GaAs plasma layer controlled optically has been proposed by Neikirk and Itoh [6].

In all of these structures, the slow-wave mechanism is generated by spatial separation of the electric and magnetic energy. Most of the electric energy is located in the lossless insulator layer or a depletion region whereas the magnetic field penetrates deep into the lossy layer and semi-insulating layer. Since the spatial separation is accomplished by the existence of the lossy layer, these slow-wave lines are inherently lossy. One remedy to reduce loss has been proposed by Fukuoka and Itoh [7] in which a CPW created on a periodically doped substrate is used. Recently, Hasegawa proposed a new crosstie coplanar waveguide (CTCPW) (Fig.1.3) slow-wave structure in which the wave attenuation is due predominantly to the conductor loss [8]. Hasegawa reported the realization of slow-wave factor (λ_0/λ_g) as high as 15 both theoretically and experimentally. A similar structure has also been used by Bastida and Donzelli [9].

In this study, we have suggested a modification of Hasegawa's CTCPW and proposed a different crosstie overlay slow-wave structure (see Fig.1.4) which is more adaptable for monolithic circuit integration. Instead of buried crossties, overlay crossties were used. As shown in Fig.1.4, both CPW and microstrip versions of the new slow-wave structure can be realized by the overlay technique. The structure has several useful features. (1) Fabrication of the structures proposed

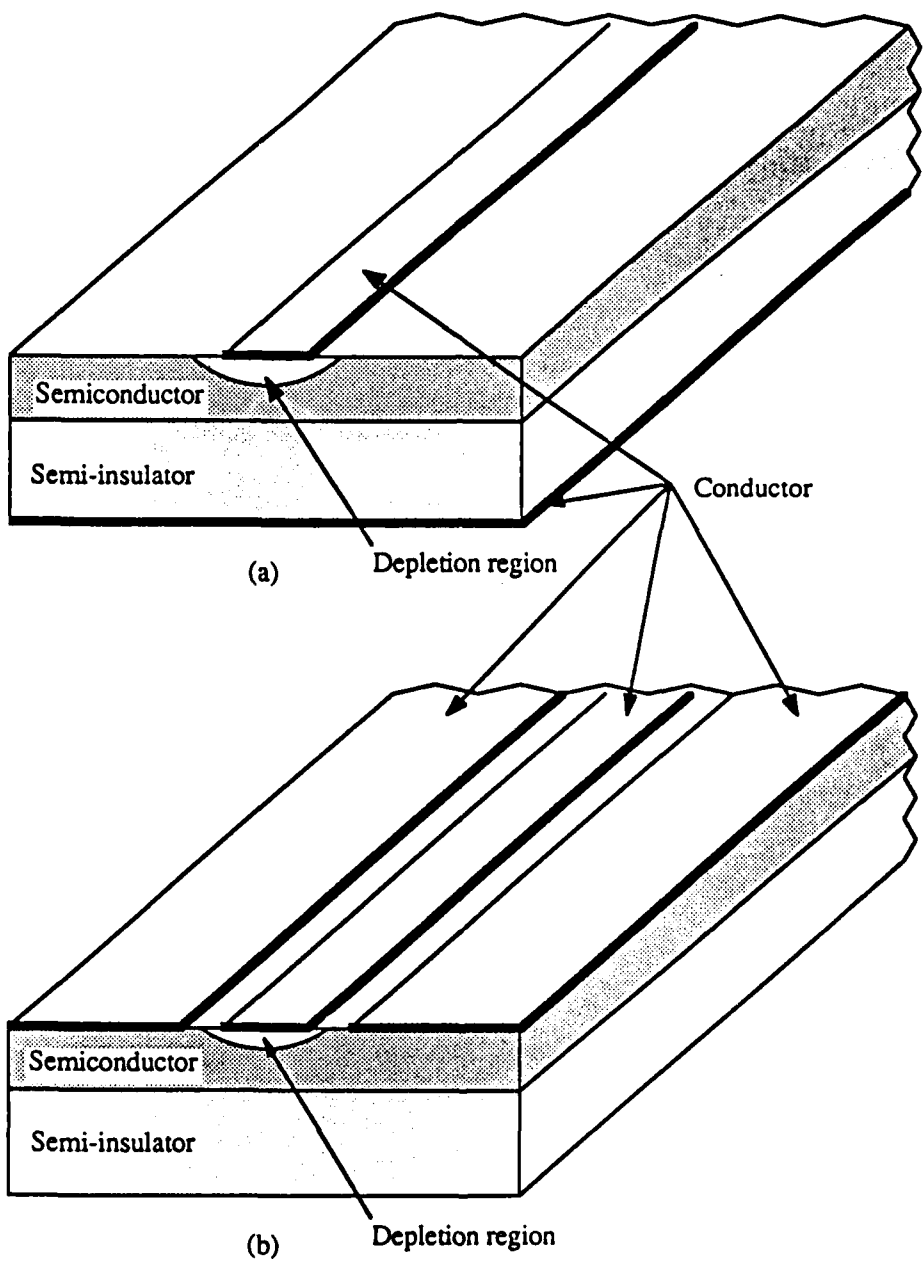


Fig.1.2 Schottky contact slow-wave structures. (a) Schottky microstrip line,
(b) Schottky coplanar waveguide.

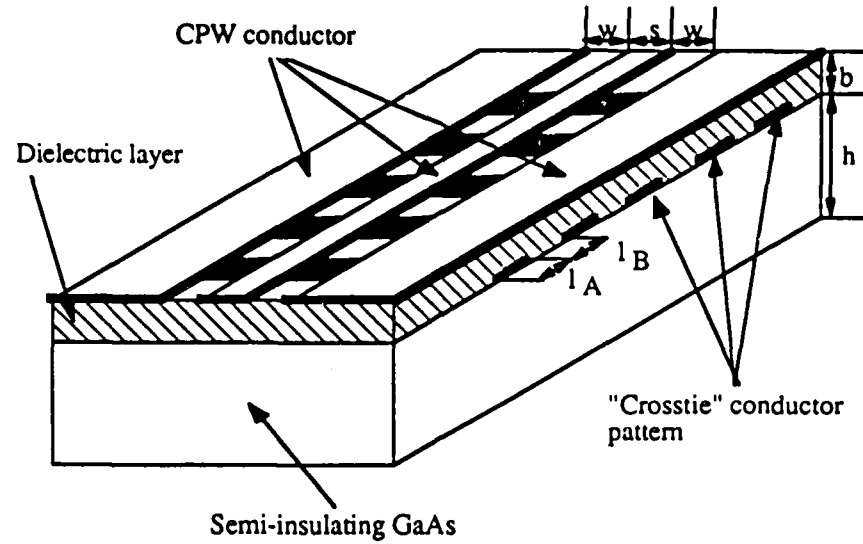
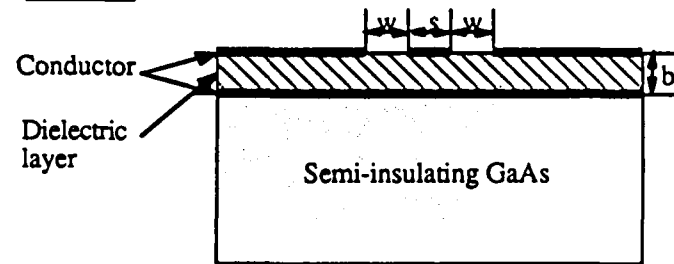
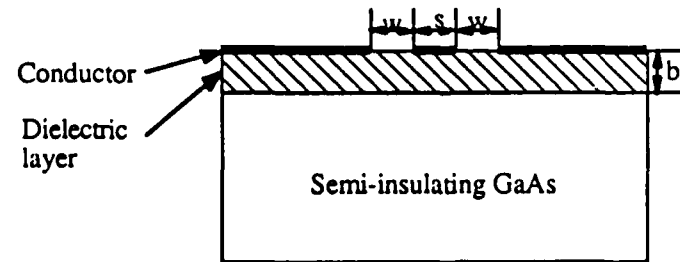
Section ASection B

Fig.1.3 Crosstie coplanar waveguide (CTCPW) slow-wave structure (by Hasegawa).

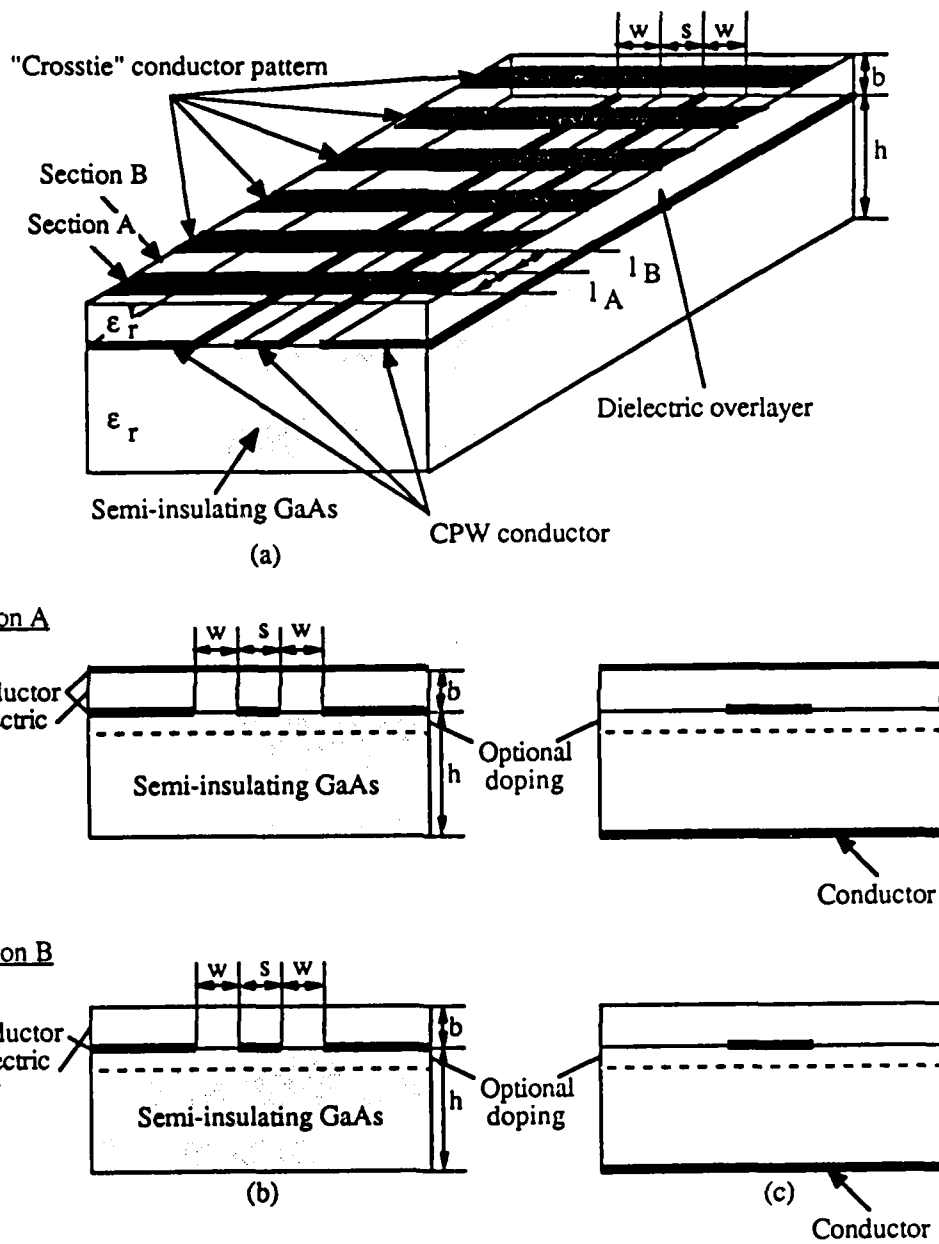


Fig.1.4 Crosstie overlay CPW and microstrip slow-wave structures. (a) CPW, (b) Cross-section of CPW, (c) Cross-section of microstrip.

here is easier. In fact, it is fairly common to provide a dielectric overlay on the MMIC's for protection. The metal crossties are periodically evaporated on the dielectric overlay. The crossties may be connected to the ground planes of the CPW at some distance away from the center conductor. (2) The new slow-wave structures can be made free of dielectric loss in principle if no tuning is required, although minimization of the conductor loss is still important. (3) It is possible to combine this new crosstie overlay mechanism with a Schottky slow-wave mechanism by providing a doped layer before the CPW electrodes or the microstrip is created on a semi-insulating GaAs substrate. In such a structure, the attenuation introduced by the doped layer should be minimized while some bias tunability of a Schottky slow-wave mechanism is retained. Periodic doping [7] may be one candidate. Because two slow-wave mechanisms are combined, the loss can be smaller even before optimization.

Grating structures are found useful in millimeter-wave integrated circuit applications such as band-reject filters [10][11] and distributed Bragg reflector (DBR) oscillators [12]. In such applications, the gratings would be operated in stopbands, corresponding to Bragg reflection, in order to produce strong reflections. Because the band-reject filters or DBR structures made of the conventional dielectric waveguide and printed line tend to be electrically and physically long, they are not very suitable for monolithic integrated circuits. However, if such periodic structures can be made of the proposed crosstie slow-wave structures, the physical size of the grating can be made smaller while the electrical length is still long enough to observe grating effects. In this study, first, the dispersive characteristics of the new crosstie

slow-wave CPW were confirmed experimentally. Second, the distributed Bragg reflectors (DBR's) were made of the new overlay crosstie mechanism to realize a slow-wave band-reject grating with a physically short dimension. From the transmission and reflection characteristic measurements, a band-reject phenomenon was confirmed. Although such frequency-selective band-reject gratings can give strong stopbands, their passbands may have ripples which are excessive for many applications. In order to obtain better control of the passband ripple at a reasonably low level, we created a slow-wave reflector from the new crosstie overlay CPW's which has a prescribed stopband and also prescribed Chebyshev passbands. A monolithic slow-wave Chebyshev reflector has been designed and fabricated. After the conductor loss was taken into account, good agreement between theory and preliminary experiments was observed. Based on the same theory, a new slow-wave reflector created from a modified crosstie overlay CPW is proposed and examined. A respectable slow-wave factor and a drastic reduction of conductor loss have been obtained.

In conclusion, let us summarize the objectives of this study :

1. Develop a new planar low-loss slow-wave structure amenable to monolithic integration.
2. Based on the new slow-wave structure in which the guide wavelength is extremely small, compact grating structures are found for use as a frequency selective DBR. The DBR's are exploited to facilitate band-reject grating implementation.
3. Create a slow-wave Chebyshev reflector by use of the new slow-wave structures

in order to get a better control in the passband ripple size and the stopband shape.

1.2 THESIS ORGANIZATION

Following the present introductory Chapter 1 of the thesis, the propagation characteristics of the new crosstie overlay slow-wave CPW's are analyzed theoretically based on the spectral domain method and Floquet's theorem in Chapter 2. The effect of conductor loss is included. The predicted and experimental results are presented. In Chapter 3, we consider the use of these new slow-wave CPW's for the creation of band-reject gratings. The calculated and measured band-reject grating properties are presented. Chapter 4 describes the systematic design procedure of a slow-wave Chebyshev reflector made of the new crosstie overlay slow-wave CPW's. The theoretical and the preliminary experimental results are shown. A new slow-wave reflector based on a modified crosstie overlay CPW is proposed for the reduction of conductor loss. Chapter 5 summarizes the contributions of this study, presents some recommendations, and proposes some related problems for future research. Finally, a list of references ends the thesis.

CHAPTER 2 : CROSSTIE OVERLAY SLOW-WAVE COPLANAR WAVEGUIDE

2.1 TRANSMISSION LINE CANDIDATES FOR NEW SLOW-WAVE MECHANISM IMPLEMENTATION

At microwave frequencies, the interconnections between elements on a high dielectric constant substrate such as GaAs, where considerable wavelength reduction occurs, must be treated as wave guiding structures. On a planar substrate, transmission line media have been intensively and extensively studied over a spectral band spanning the HF, UHF, microwave, millimeter-wave, and optical regions. The configurations (Fig.2.1) that have received the most attention are microstrip line (Fig.2.1(a)), slot line (Fig.2.1(b)), coplanar waveguide (Fig.2.1(c)), and coplanar strip (Fig.2.1(d)). Of the four transmission lines, microstrip line and oplanar waveguide are considered to be the most suitable for MMIC's based on the considerations of chip yield and electrical performance [1]. As shown in Fig.1.4, both CPW and microstrip line can be viable candidates for the new crosstie overlay slow-wave structure implementation.

In this study, however, coplanar waveguide has been adopted as the new slow-wave transmission line building block due to the two major advantages it offers over microstrip line in the design of a complex MMIC. (1) The source groundings of the active devices are done easily without the use of via holes. This allows for thick substrates offering easier handling and a reduced number of processing steps, leading to increased yield. (2) Since a ground plane exists between any two adjacent

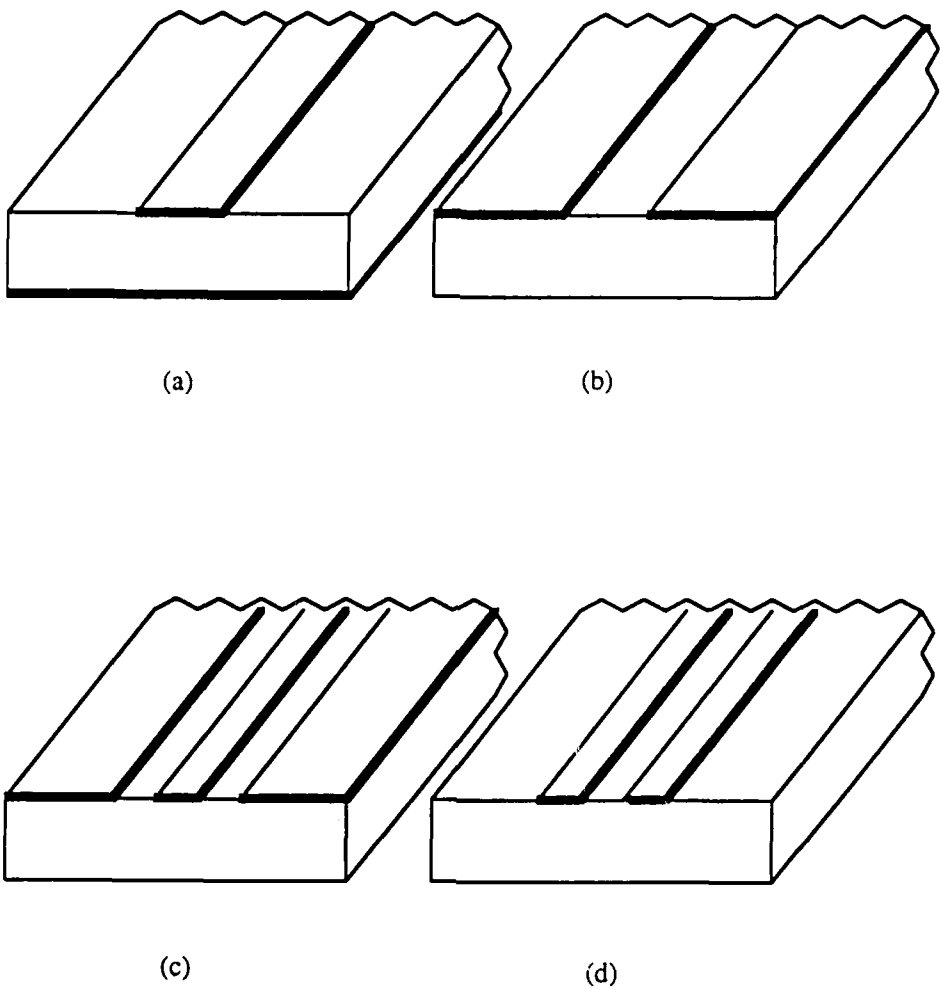


Fig.2.1 Transmission lines in MMICs. (a) Microstrip, (b) Slotline, (c) Coplanar waveguide, (d) Coplanar strips.

transmission lines, coupling problems are reduced resulting in potentially more compact designs.

In a coplanar waveguide, the top substrate surface is used for both a signal line and the ground plane. The normal propagation mode on this structure is quasi-TEM and is referred to as the odd mode. In this mode, the electric field vectors in the two slots of the line point in opposite directions [13]. Another propagation mode is the even mode, in which the electric fields in the slots point in the same direction. This is a non-TEM mode and generally needs to be suppressed. Suppressing the even mode as well as connecting all the grounded regions are achieved by the introduction of airbridges across the line, connecting the ground planes on both sides of the center conductor. This effectively increases the cutoff frequency of the even mode, leading to single-mode operation. In the new crosstie overlay slow-wave CPW, metal crossties can also serve this purpose.

2.2 SLOW-WAVE PRINCIPLE AND WAVEGUIDE STRUCTURE FOR THE NEW CROSSTIE OVERLAY SLOW-WAVE COPLANAR WAVEGUIDE

The basic operating principle of how the crosstie structure works as a slow-wave transmission line is a spatial separation of electric and magnetic energy. As shown in Fig.1.4, in the section 1A with a crosstie strip, the capacitance is significantly increased, whereas the section 1B with only the dielectric overlay is more inductive. The spatial separation of energy is therefore accomplished in a periodic manner. This structure is essentially a grating. However, we do not use this

structure as a grating. By making the period $l_A + l_B$ in Fig. 1.4 sufficiently smaller than the operating wavelength, the operating point is far from the stopband and this structure models a uniform transmission line with its propagation constant and characteristic impedance calculable from the periodic dispersion relation.

The theoretical treatment of the new slow-wave CPW consists of using Floquet's theorem for periodic transmission lines. To do this, accurate values of both propagation constant and characteristic impedance of the constituent sections l_A and l_B need to be calculated. Using standard spectral domain analysis [14], these values can be calculated and the periodic slow-wave CPW can be analyzed.

In the following Section 2.3, the procedures of spectral domain analysis are presented in more depth. In Section 2.4, the information about propagation characteristics for each constituent section has been used in Floquet's theorem to derive the periodic dispersion relation for the new crosstie slow-wave CPW's. The effect of conductor loss is considered in Section 2.5. Finally, an experiment has been conducted to confirm the predicted dispersive characteristics of the crosstie overlay slow-wave CPW's in Section 2.6.

2.3 FORMULATION OF SPECTRAL DOMAIN ANALYSIS

The spectral domain method has been developed for efficient numerical analysis for various printed transmission lines [15],[16],[17],[18]. Unlike quasi-static approximations, this method is a full-wave analysis which can predict the frequency-dependent line properties required in broadband design. It is superior to

other numerical methods because of the efficiency of numerical calculation and the ease of formulation [14].

2.3.1 PROPAGATION CONSTANT

The cross-sectional view of the general constituent sections A and B (defined in Fig.1.4) in the new crosstie overlay slow-wave CPW are given in Fig.2.2. The coordinate system is defined in a manner such that wave propagation takes place in the z-direction.

In conventional space domain analysis [19], this structure may be analyzed by first formulating the following coupled homogeneous integral equations and then solving for the unknown propagation constant :

$$\int \left[Y_{xx}(x-x,\beta)E_x(x) + Y_{xz}(x-x,\beta)E_z(x) \right] dx = J_x(x) \quad (2.1a)$$

$$\int \left[Y_{zx}(x-x,\beta)E_x(x) + Y_{zz}(x-x,\beta)E_z(x) \right] dx = J_z(x) \quad (2.1b)$$

where E_x , E_z , J_x , and J_z are unknown electric field and current components on the boundary $y=h$ and the Green's functions (admittance functions) Y_{xx} , etc., are functions of the propagation constant β . The boundary conditions at $y=h$ require that E_x and E_z be zero at the infinitesimally thin and perfect conductor except on the slots where J_x and J_z are required to be zero. Therefore, these equations may be solved provided that Y_{xx} , etc., are given. However, for the inhomogeneous structures, the Green's functions are not available in closed form.

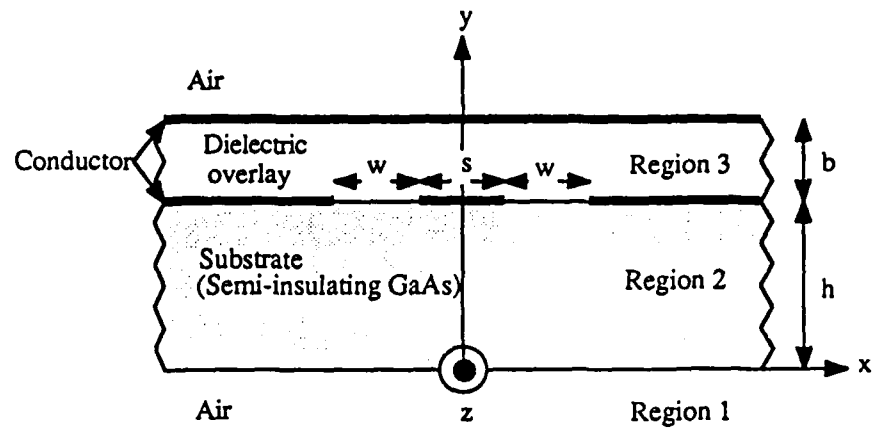
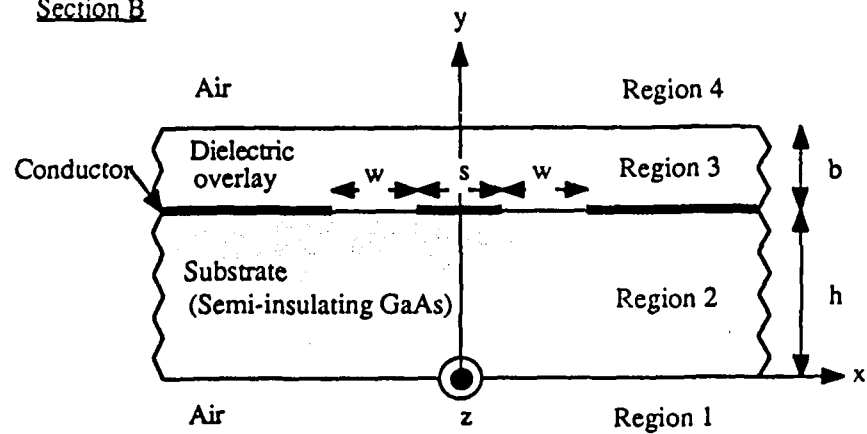
Section ASection B

Fig.2.2 Cross-sectional view of general constituent sections in the crosstie
overlay slow-wave coplanar waveguide.

In the spectral domain formulation, the convolutional type of coupled integral equations (2.1a,b) are Fourier transformed to yield the algebraic equations:

$$\tilde{Y}_{xx}(\alpha, \beta) \tilde{E}_x(\alpha) + \tilde{Y}_{xz}(\alpha, \beta) \tilde{E}_z(\alpha) = \tilde{J}_x(\alpha) \quad (2.2a)$$

$$\tilde{Y}_{zx}(\alpha, \beta) \tilde{E}_x(\alpha) + \tilde{Y}_{zz}(\alpha, \beta) \tilde{E}_z(\alpha) = \tilde{J}_z(\alpha) \quad (2.2b)$$

where the quantities with a tilde (~) are Fourier transforms of the corresponding quantities. The Fourier transform is defined as

$$\tilde{\phi}(\alpha) = \int_{-\infty}^{\infty} \phi(x) e^{j\alpha x} dx. \quad (2.3)$$

In addition to β , the algebraic equations (2.2a,b) contain four other unknowns \tilde{J}_x , \tilde{J}_z , \tilde{E}_x and \tilde{E}_z .

The Green's admittance functions are derived as follows. First, the hybrid fields are expressed in terms of superposition of TM-to-y and TE-to-y expressions by way of vector potentials. The electric and magnetic vector potentials are defined in each region as

$$\Phi_i^h(x, y, z) = \hat{a}_y \phi_{yi}^h(x, y) e^{-j\beta z} \quad (2.4a)$$

$$\Phi_i^e(x, y, z) = \hat{a}_y \phi_{yi}^e(x, y) e^{-j\beta z} \quad (2.4b)$$

$i=1,2,3$ for Section A (with crosstie strip)
 $=1,2,3,4$ for Section B (without crosstie strip)

where the time convention $e^{j\omega t}$ ($\omega=2\pi f$, f is the operating frequency) is implied, and harmonic solutions in the z direction are assumed. Beta (β) is the phase constant and \hat{a}_y denotes the unit vector in the y direction. Since the vector potentials satisfy the vector Helmholtz equation, the scalar functions ϕ_{yi}^h and ϕ_{yi}^e should satisfy the scalar

Helmholtz equation

$$\frac{\partial^2 \phi_{yi}^h}{\partial x^2} + \frac{\partial^2 \phi_{yi}^h}{\partial y^2} + (\epsilon_n k_0^2 - \beta^2) \phi_{yi}^h = 0 \quad (2.5a)$$

$$\frac{\partial^2 \phi_{yi}^e}{\partial x^2} + \frac{\partial^2 \phi_{yi}^e}{\partial y^2} + (\epsilon_n k_0^2 - \beta^2) \phi_{yi}^e = 0 \quad (2.5b)$$

where $k_0 = \omega \sqrt{\mu_0 \epsilon_0}$ is the free space wavenumber (μ_0 is the permeability of free space) and ϵ_{ri} is the relative dielectric constant in region i. In homogeneous source-free regions, the electromagnetic field in terms of Φ_i^h and Φ_i^e is given [20] by :

$$\mathbf{E}_i = -\nabla_x \Phi_i^h + \frac{1}{\lambda} \nabla_x \nabla_x \Phi_i^e \quad (2.6a)$$

$$\mathbf{H}_i = \nabla_x \Phi_i^e + \frac{1}{\lambda} \nabla_x \nabla_x \Phi_i^h \quad (2.6b)$$

where $y_i^\wedge = j\omega \epsilon_{ri} \epsilon_0$ and $z_i^\wedge = j\omega \mu_0$.

After taking the Fourier transforms of equation (2.5), we obtain solutions for the transformed quantities $\phi_{yi}^{-h}(\alpha, y)$ and $\phi_{yi}^{-e}(\alpha, y)$:

For Section A :

$$\tilde{\phi}_{y1}^h(\alpha, y) = A^h e^{\gamma_1 y} \quad ; y < 0 \quad (2.7a)$$

$$\tilde{\phi}_{y1}^e(\alpha, y) = A^e e^{\gamma_1 y} \quad ; y < 0 \quad (2.7b)$$

$$\tilde{\phi}_{y2}^h(\alpha, y) = B^h \cosh \gamma_2 y + C^h \sinh \gamma_2 y \quad ; 0 < y < h \quad (2.7c)$$

$$\tilde{\phi}_{y2}^e(\alpha, y) = B^e \sinh \gamma_2 y + C^e \cosh \gamma_2 y \quad ; 0 < y < h \quad (2.7d)$$

$$\tilde{\phi}_{y3}^h(\alpha, y) = D^h \sinh \gamma_3 (b+h-y) \quad ; h < y < b+h \quad (2.7e)$$

$$\tilde{\phi}_{y3}^e(\alpha, y) = D^e \cosh \gamma_3 (b+h-y) \quad ; h < y < b+h \quad (2.7f)$$

$$\gamma_i = \sqrt{\alpha^2 + \beta^2 - \epsilon_{ri} k_0^2} \quad ; i = 1, 2, 3 \quad (2.7g)$$

For Section B :

$$\tilde{\phi}_{y_1}^h(\alpha, y) = A^h e^{\gamma_1 y} \quad ; y < 0 \quad (2.8a)$$

$$\tilde{\phi}_{y_1}^e(\alpha, y) = A^e e^{\gamma_1 y} \quad ; y < 0 \quad (2.8b)$$

$$\tilde{\phi}_{y_2}^h(\alpha, y) = B^h \cosh \gamma_2 y + C^h \sinh \gamma_2 y \quad ; 0 < y < h \quad (2.8c)$$

$$\tilde{\phi}_{y_2}^e(\alpha, y) = B^e \sinh \gamma_2 y + C^e \cosh \gamma_2 y \quad ; 0 < y < h \quad (2.8d)$$

$$\tilde{\phi}_{y_3}^h(\alpha, y) = D^h \cosh \gamma_3(y-h) + E^h \sinh \gamma_3(y-h) \quad ; h < y < b+h \quad (2.8e)$$

$$\tilde{\phi}_{y_3}^e(\alpha, y) = D^e \sinh \gamma_3(y-h) + E^e \cosh \gamma_3(y-h) \quad ; h < y < b+h \quad (2.8f)$$

$$\tilde{\phi}_{y_4}^h(\alpha, y) = F^h e^{-\gamma_4[y-(b+h)]} \quad ; b+h < y \quad (2.8g)$$

$$\tilde{\phi}_{y_4}^e(\alpha, y) = F^e e^{-\gamma_4[y-(b+h)]} \quad ; b+h < y \quad (2.8h)$$

$$\gamma_i = \sqrt{\alpha^2 + \beta^2 - \epsilon_{n0} k_z^2} \quad ; i=1,2,3,4 \quad (2.8i)$$

where $A^h, A^e, B^h, B^e, C^h, C^e, D^h, D^e, E^h, E^e, F^h, F^e$ are unknown coefficients and γ_i is the propagation constant in the y direction in the i -th region. The boundary condition of the perfectly conducting plane at $y=b+h$ is embedded in this set of solutions. Also, γ_1 and γ_4 are chosen to be positive so that the radiation conditions at $y=\pm\infty$ are satisfied. Substitution of these solutions into the Fourier transforms of equation (2.6a,b) yields the field expressions in each region :

For Section A :Region 1 ($y < 0$)

$$\tilde{E}_{x1} = [-j\beta A^h - j \frac{\alpha \gamma_1}{\gamma_1} A^e] e^{\gamma_1 y} \quad (2.9a)$$

$$\tilde{E}_{y1} = [-z_1 + \frac{\gamma_1^2}{\gamma_1}] A^e e^{\gamma_1 y} \quad (2.9b)$$

$$\tilde{E}_{z1} = [j\alpha A^h - j \frac{\beta \gamma_1}{\gamma_1} A^e] e^{\gamma_1 y} \quad (2.9c)$$

$$\tilde{H}_{x1} = [j\beta A^e - j \frac{\alpha \gamma_1}{z_1} A^h] e^{\gamma_1 y} \quad (2.9d)$$

$$\tilde{H}_{y1} = [-y_1^h + \frac{\gamma_1^2}{z_1}] A^h e^{\gamma_1 y} \quad (2.9e)$$

$$\tilde{H}_{z1} = [-j\alpha A^e - j \frac{\beta \gamma_1}{z_1} A^h] e^{\gamma_1 y} \quad (2.9f)$$

Region 2 ($0 < y < h$)

$$\tilde{E}_{x2} = [-j\beta B^h - j \frac{\alpha \gamma_2}{y_2} B^e] \cosh \gamma_2 y + [-j\beta C^h - j \frac{\alpha \gamma_2}{y_2} C^e] \sinh \gamma_2 y \quad (2.10a)$$

$$\tilde{E}_{y2} = [-z_2^h + \frac{\gamma_2^2}{y_2}] [B^e \sinh \gamma_2 y + C^e \cosh \gamma_2 y] \quad (2.10b)$$

$$\tilde{E}_{z2} = [j\alpha B^h - j \frac{\beta \gamma_2}{y_2} B^e] \cosh \gamma_2 y + [j\alpha C^h - j \frac{\beta \gamma_2}{y_2} C^e] \sinh \gamma_2 y \quad (2.10c)$$

$$\tilde{H}_{x2} = [j\beta B^e - j \frac{\alpha \gamma_2}{z_2} B^h] \sinh \gamma_2 y + [j\beta C^e - j \frac{\alpha \gamma_2}{z_2} C^h] \cosh \gamma_2 y \quad (2.10d)$$

$$\tilde{H}_{y2} = [-y_2^h + \frac{\gamma_2^2}{z_2}] [B^h \cosh \gamma_2 y + C^h \sinh \gamma_2 y] \quad (2.10e)$$

$$\tilde{H}_{z2} = [-j\alpha B^e - j \frac{\beta \gamma_2}{z_2} B^h] \sinh \gamma_2 y + [-j\alpha C^e - j \frac{\beta \gamma_2}{z_2} C^h] \cosh \gamma_2 y \quad (2.10f)$$

Region 3 ($h < y < b+h$)

$$\tilde{E}_{x3} = [-j\beta D^h + j \frac{\alpha \gamma_3}{y_3} D^e] \sinh \gamma_3 (b+h-y) \quad (2.11a)$$

$$\tilde{E}_{y3} = [-z_3^h + \frac{\gamma_3^2}{y_3}] D^e \cosh \gamma_3 (b+h-y) \quad (2.11b)$$

$$\tilde{E}_{z3} = [j\alpha D^h + j\frac{\beta \gamma_3}{\gamma_3} D^e] \sinh \gamma_3 (b+h-y) \quad (2.11c)$$

$$\tilde{H}_{x3} = [j\beta D^e + j\frac{\alpha \gamma_3}{\gamma_3} D^h] \cosh \gamma_3 (b+h-y) \quad (2.11d)$$

$$\tilde{H}_{y3} = [-y_3 + \frac{\gamma_3^2}{\gamma_3}] D^h \sinh \gamma_3 (b+h-y) \quad (2.11e)$$

$$\tilde{H}_{z3} = [-j\alpha D^e + j\frac{\beta \gamma_3}{\gamma_3} D^h] \cosh \gamma_3 (b+h-y) \quad (2.11f)$$

For Section B :

The field expressions in Region 1 ($y < 0$) and Region 2 ($0 < y < h$) are identical to those in Section A.

Region 3 ($h < y < b+h$)

$$\tilde{E}_{x3} = [-j\beta D^h - j\frac{\alpha \gamma_3}{\gamma_3} D^e] \cosh \gamma_3 (y-h) + [-j\beta E^h - j\frac{\alpha \gamma_3}{\gamma_3} E^e] \sinh \gamma_3 (y-h) \quad (2.12a)$$

$$\tilde{E}_{y3} = [-z_3 + \frac{\gamma_3^2}{\gamma_3}] [D^e \sinh \gamma_3 (y-h) + E^e \cosh \gamma_3 (y-h)] \quad (2.12b)$$

$$\tilde{E}_{z3} = [j\alpha D^h - j\frac{\beta \gamma_3}{\gamma_3} D^e] \cosh \gamma_3 (y-h) + [j\alpha E^h - j\frac{\beta \gamma_3}{\gamma_3} E^e] \sinh \gamma_3 (y-h) \quad (2.12c)$$

$$\tilde{H}_{x3} = [j\beta D^e - j\frac{\alpha \gamma_3}{\gamma_3} D^h] \sinh \gamma_3 (y-h) + [j\beta E^e - j\frac{\alpha \gamma_3}{\gamma_3} E^h] \cosh \gamma_3 (y-h) \quad (2.12d)$$

$$\tilde{H}_{y3} = [-y_3 + \frac{\gamma_3^2}{\gamma_3}] [D^h \cosh \gamma_3 (y-h) + E^h \sinh \gamma_3 (y-h)] \quad (2.12e)$$

$$\tilde{H}_{z3} = [-j\alpha D^e - j\frac{\beta \gamma_3}{\gamma_3} D^h] \sinh \gamma_3 (y-h) + [-j\alpha E^e - j\frac{\beta \gamma_3}{\gamma_3} E^h] \cosh \gamma_3 (y-h) \quad (2.12f)$$

Region 4 ($b+h < y$)

$$\tilde{E}_{x4} = [-j\beta F^h + j \frac{\alpha \gamma_4}{y_4} F^e] e^{-\gamma_4 [y-(b+h)]} \quad (2.13a)$$

$$\tilde{E}_{y4} = [-z_4^h + \frac{\gamma_4^2}{y_4}] F^e e^{-\gamma_4 [y-(b+h)]} \quad (2.13b)$$

$$\tilde{E}_{z4} = [j\alpha F^h + j \frac{\beta \gamma_4}{y_4} F^e] e^{-\gamma_4 [y-(b+h)]} \quad (2.13c)$$

$$\tilde{H}_{x4} = [j\beta F^e + j \frac{\alpha \gamma_4}{z_4} F^h] e^{-\gamma_4 [y-(b+h)]} \quad (2.13d)$$

$$\tilde{H}_{y4} = [-y_4^h + \frac{\gamma_4^2}{z_4}] F^e e^{-\gamma_4 [y-(b+h)]} \quad (2.13e)$$

$$\tilde{H}_{z4} = [-j\alpha F^e + j \frac{\beta \gamma_4}{z_4} F^h] e^{-\gamma_4 [y-(b+h)]} \quad (2.13f)$$

Finally, the boundary conditions at $y=0$, $y=h$, and $y=b+h$ have to be satisfied.

In the spectral (or Fourier transform) domain, the boundary conditions are :

For Section A :

$$\tilde{E}_{x1}(\alpha, 0) = \tilde{E}_{x2}(\alpha, 0) \quad (2.14a)$$

$$\tilde{E}_{z1}(\alpha, 0) = \tilde{E}_{z2}(\alpha, 0) \quad (2.14b)$$

$$\tilde{H}_{x1}(\alpha, 0) = \tilde{H}_{x2}(\alpha, 0) \quad (2.14c)$$

$$\tilde{H}_{z1}(\alpha, 0) = \tilde{H}_{z2}(\alpha, 0) \quad (2.14d)$$

$$\tilde{E}_{x2}(\alpha, h) = \tilde{E}_{x3}(\alpha, h) = \tilde{E}_x(\alpha, h) \quad (2.14e)$$

$$\tilde{E}_{z2}(\alpha, h) = \tilde{E}_{z3}(\alpha, h) = \tilde{E}_z(\alpha, h) \quad (2.14f)$$

$$\tilde{H}_{x2}(\alpha, h) - \tilde{H}_{x3}(\alpha, h) = \tilde{J}_z(\alpha, h) \quad (2.14g)$$

$$\tilde{H}_{z2}(\alpha, h) - \tilde{H}_{z3}(\alpha, h) = -\tilde{J}_x(\alpha, h) \quad (2.14h)$$

For Section B :

$$\tilde{E}_{x1}(\alpha, 0) = \tilde{E}_{x2}(\alpha, 0) \quad (2.15a)$$

$$\tilde{E}_{z1}(\alpha, 0) = \tilde{E}_{z2}(\alpha, 0) \quad (2.15b)$$

$$\tilde{H}_{x1}(\alpha, 0) = \tilde{H}_{x2}(\alpha, 0) \quad (2.15c)$$

$$\tilde{H}_{z1}(\alpha, 0) = \tilde{H}_{z2}(\alpha, 0) \quad (2.15d)$$

$$\tilde{E}_{x2}(\alpha, h) = \tilde{E}_{x3}(\alpha, h) = \tilde{E}_x(\alpha, h) \quad (2.15e)$$

$$\tilde{E}_{z2}(\alpha, h) = \tilde{E}_{z3}(\alpha, h) = \tilde{E}_z(\alpha, h) \quad (2.15f)$$

$$\tilde{H}_{x2}(\alpha, h) - \tilde{H}_{x3}(\alpha, h) = \tilde{J}_z(\alpha, h) \quad (2.15g)$$

$$\tilde{H}_{z2}(\alpha, h) - \tilde{H}_{z3}(\alpha, h) = -\tilde{J}_x(\alpha, h) \quad (2.15h)$$

$$\tilde{E}_{x3}(\alpha, b+h) = \tilde{E}_{x4}(\alpha, b+h) \quad (2.15i)$$

$$\tilde{E}_{z3}(\alpha, b+h) = \tilde{E}_{z4}(\alpha, b+h) \quad (2.15j)$$

$$\tilde{H}_{x3}(\alpha, b+h) = \tilde{H}_{x4}(\alpha, b+h) \quad (2.15k)$$

$$\tilde{H}_{z3}(\alpha, b+h) = \tilde{H}_{z4}(\alpha, b+h) \quad (2.15l)$$

where \tilde{J}_z and \tilde{J}_x are Fourier transforms of unknown current components J_z and J_x on the conducting region at $y=h$. These conditions allow us to obtain the expressions for coefficients $A^h, A^e, B^h, B^e, C^h, C^e, D^h, D^e, E^h, E^e, F^h$, and F^e in terms of \tilde{J}_z and \tilde{J}_x :

For Section A :

$$A^h = j \left(\frac{\alpha \tilde{J}_z - \beta \tilde{J}_x}{\alpha^2 + \beta^2} \right) \cdot \begin{vmatrix} \frac{\gamma_1}{z_1} \cosh \gamma_2 h + \frac{\gamma_2}{z_2} \sinh \gamma_2 h + \frac{\gamma_3}{z_3} \frac{\cosh \gamma_2 h \cdot \cosh \gamma_3 b}{\sinh \gamma_3 b} \\ \frac{\gamma_1 \gamma_3}{z_1 z_3} \frac{\gamma_2}{z_2} \frac{\sinh \gamma_2 h \cdot \cosh \gamma_3 b}{\sinh \gamma_3 b} \end{vmatrix}^{-1} \quad (2.16a)$$

$$A^e = -j \left(\frac{\beta \hat{J}_z + \alpha \hat{J}_x}{\alpha^2 + \beta^2} \right) \begin{pmatrix} \cosh \gamma_2 h + \frac{\gamma_1 \hat{y}_2}{\gamma_2 \hat{y}_1} \sinh \gamma_2 h + \frac{\gamma_1 \hat{y}_3}{\gamma_3 \hat{y}_1} \cosh \gamma_2 h \cosh \gamma_3 b & \gamma_1 \hat{y}_3 \cosh \gamma_2 h \cosh \gamma_3 b \\ \gamma_2 \hat{y}_3 \sinh \gamma_2 h \cosh \gamma_3 b & \gamma_3 \hat{y}_2 \sinh \gamma_3 b \end{pmatrix}^{-1} \quad (2.16b)$$

$$B^h = A^h \quad (2.16c)$$

$$B^e = \frac{\gamma_1 \hat{y}_2}{\gamma_2 \hat{y}_1} A^e \quad (2.16d)$$

$$C^h = \frac{\gamma_1 \hat{z}_2}{\gamma_2 \hat{z}_1} A^h \quad (2.16e)$$

$$C^e = A^e \quad (2.16f)$$

$$D^h = \frac{1}{\sinh \gamma_3 b} \left(\cosh \gamma_2 h + \frac{\gamma_1 \hat{z}_2}{\gamma_2 \hat{z}_1} \sinh \gamma_2 h \right) A^h \quad (2.16g)$$

$$D^e = \frac{1}{\gamma_3 \sinh \gamma_3 b} \left(\frac{\gamma_1}{\hat{y}_1} \cosh \gamma_2 h + \frac{\gamma_2}{\hat{y}_2} \sinh \gamma_2 h \right) A^e \quad (2.16h)$$

For Section B :

$$A^h = j \left(\frac{\alpha \hat{J}_z - \beta \hat{J}_x}{\alpha^2 + \beta^2} \right) \cdot \left[\begin{pmatrix} \frac{\gamma_1}{\hat{z}_1} \cosh \gamma_2 h + \frac{\gamma_2}{\hat{z}_2} \sinh \gamma_2 h + \frac{\gamma_3}{\hat{z}_3} \left(\cosh \gamma_2 h + \frac{\gamma_1 \hat{z}_2}{\gamma_2 \hat{z}_1} \sinh \gamma_2 h \right) & 1 \\ \left(\frac{\gamma_3}{\hat{z}_3} \sinh \gamma_3 b + \frac{\gamma_4}{\hat{z}_4} \cosh \gamma_3 b \right) & \left(\frac{\gamma_3}{\hat{z}_3} \cosh \gamma_3 b + \frac{\gamma_4}{\hat{z}_4} \sinh \gamma_3 b \right) \end{pmatrix}^{-1} \right] \quad (2.17a)$$

$$A^e = -J \left(\frac{\beta J_z + \alpha J_x}{\alpha^2 + \beta^2} \right) \cdot \begin{bmatrix} \cosh \gamma_2 h + \frac{\gamma_1 \hat{y}_2}{\gamma_2 \hat{y}_1} \sinh \gamma_2 h + \frac{\hat{y}_3}{\gamma_3} \left(\frac{\gamma_1}{\hat{y}_1} \cosh \gamma_2 h + \frac{\gamma_2}{\hat{y}_2} \sinh \gamma_2 h \right) \\ \cdot \left(\frac{\gamma_3}{\hat{y}_3} \cosh \gamma_3 b + \frac{\gamma_4}{\hat{y}_4} \sinh \gamma_3 b \right) \cdot \left(\frac{\gamma_3}{\hat{z}_3} \cosh \gamma_3 b + \frac{\gamma_4}{\hat{z}_4} \sinh \gamma_3 b \right) \end{bmatrix}^{-1} \quad (2.17b)$$

$$B^h = A^h \quad (2.17c)$$

$$B^e = \frac{\gamma_1 \hat{y}_2}{\gamma_2 \hat{y}_1} A^e \quad (2.17d)$$

$$C^h = \frac{\gamma_1 \hat{z}_2}{\gamma_2 \hat{z}_1} A^h \quad (2.17e)$$

$$C^e = A^e \quad (2.17f)$$

$$D^h = \left(\cosh \gamma_2 h + \frac{\gamma_1 \hat{z}_2}{\gamma_2 \hat{z}_1} \sinh \gamma_2 h \right) A^h \quad (2.17g)$$

$$D^e = \frac{\hat{y}_3}{\gamma_3} \left(\frac{\gamma_1}{\hat{y}_1} \cosh \gamma_2 h + \frac{\gamma_2}{\hat{y}_2} \sinh \gamma_2 h \right) A^e \quad (2.17h)$$

$$E^h = \left[\begin{pmatrix} \cosh \gamma_2 h + \frac{\gamma_1 \hat{z}_2}{\gamma_2 \hat{z}_1} \sinh \gamma_2 h & \frac{\hat{y}_3}{\gamma_3} \sinh \gamma_3 b + \frac{\gamma_4}{\hat{z}_4} \cosh \gamma_3 b \\ \frac{\gamma_3}{\hat{z}_3} \cosh \gamma_3 b + \frac{\gamma_4}{\hat{z}_4} \sinh \gamma_3 b & \end{pmatrix}^{-1} \right] A^h \quad (2.17i)$$

$$E^e = \left[\begin{array}{c} \frac{\hat{y}_3}{\gamma_3} \left(\frac{\gamma_1}{\hat{y}_1} \cosh \gamma_2 h + \frac{\gamma_2}{\hat{y}_2} \sinh \gamma_2 h \right) \\ \frac{\gamma_3}{\hat{y}_3} \left(\frac{\gamma_1}{\hat{y}_1} \cosh \gamma_3 b + \frac{\gamma_4}{\hat{y}_4} \sinh \gamma_3 b \right)^{-1} \\ \frac{\hat{z}_3}{\gamma_3} \left(\frac{\gamma_3}{\hat{z}_3} \cosh \gamma_3 b + \frac{\gamma_4}{\hat{z}_4} \sinh \gamma_3 b \right) \end{array} \right] A^e \quad (2.17j)$$

$$F^h = \left[\begin{array}{c} \cosh \gamma_3 b \left(\cosh \gamma_2 h + \frac{\gamma_1 \hat{z}_2}{\gamma_2 z_1} \sinh \gamma_2 h \right) - \sinh \gamma_3 b \left(\cosh \gamma_2 h + \frac{\gamma_1 \hat{z}_2}{\gamma_2 z_1} \sinh \gamma_2 h \right)^{-1} \\ \cdot \left(\frac{\gamma_3}{\hat{z}_3} \sinh \gamma_3 b + \frac{\gamma_4}{\hat{z}_4} \cosh \gamma_3 b \right) \cdot \left(\frac{\gamma_3}{\hat{z}_3} \cosh \gamma_3 b + \frac{\gamma_4}{\hat{z}_4} \sinh \gamma_3 b \right)^{-1} \end{array} \right] A^h \quad (2.17k)$$

$$F^e = \left[\begin{array}{c} \frac{\hat{y}_3}{\gamma_3} \sinh \gamma_3 b \left(\frac{\gamma_1}{\hat{y}_1} \cosh \gamma_2 h + \frac{\gamma_2}{\hat{y}_2} \sinh \gamma_2 h \right) \frac{\hat{y}_3}{\gamma_3} \cosh \gamma_3 b \left(\frac{\gamma_1}{\hat{y}_1} \cosh \gamma_2 h + \frac{\gamma_2}{\hat{y}_2} \sinh \gamma_2 h \right)^{-1} \\ \cdot \left(\frac{\gamma_3}{\hat{y}_3} \cosh \gamma_3 b + \frac{\gamma_4}{\hat{y}_4} \sinh \gamma_3 b \right) \cdot \left(\frac{\gamma_3}{\hat{z}_3} \cosh \gamma_3 b + \frac{\gamma_4}{\hat{z}_4} \sinh \gamma_3 b \right)^{-1} \end{array} \right] A^e \quad (2.17l)$$

By substituting equations (2.16a~h) and (2.17a~l) into (2.14e,f) or (2.15e,f), we obtain the algebraic equations (2.2a,b) with the Green's admittance function Y_{xx} , etc., expressed in closed forms as follows :

For Section A :

$$\tilde{Y_{xx}} = \frac{1}{\alpha^2 + \beta^2} (P\alpha^2 - Q\beta^2) \quad (2.18a)$$

$$\tilde{Y_{xz}} = \tilde{Y_{zx}} = \frac{\alpha\beta}{\alpha^2 + \beta^2} (P+Q) \quad (2.18b)$$

$$\tilde{Y_{zz}} = \frac{1}{\alpha^2 + \beta^2} (-Q\alpha^2 + P\beta^2) \quad (2.18c)$$

where

$$P = -\frac{\hat{y_3}}{\gamma_3 \sinh \gamma_3 b} \begin{pmatrix} 1 & \left(\begin{array}{c} \cosh \gamma_2 h + \frac{\gamma_1 \hat{y_2}}{\gamma_2 \hat{y_1}} \sinh \gamma_2 h + \frac{\gamma_1 \hat{y_3} \cosh \gamma_2 h \cdot \cosh \gamma_3 b}{\gamma_3 \hat{y_1}} \\ \sinh \gamma_3 b \end{array} \right) \\ \left(\begin{array}{c} \frac{\gamma_2 \hat{y_3} \sinh \gamma_2 h \cdot \cosh \gamma_3 b}{\gamma_3 \hat{y_2}} \\ \sinh \gamma_3 b \end{array} \right) & \left(\begin{array}{c} \frac{\gamma_1 \hat{y_3} \cosh \gamma_2 h}{\gamma_3 \hat{y_1} \sinh \gamma_3 b} + \frac{\gamma_2 \hat{y_3} \sinh \gamma_2 h}{\gamma_3 \hat{y_2} \sinh \gamma_3 b} \\ \end{array} \right) \end{pmatrix} \quad (2.18d)$$

$$Q = \begin{pmatrix} \frac{\gamma_1 \hat{y_2}}{\hat{z_1}} \cosh \gamma_2 h + \frac{\gamma_2 \hat{y_1}}{\hat{z_2}} \sinh \gamma_2 h + \frac{\gamma_1 \gamma_3 \hat{z_2}}{\gamma_2 \hat{z_1} \hat{z_3}} \sinh \gamma_2 h \cdot \cosh \gamma_3 b \\ \sinh \gamma_3 b \\ \left(\begin{array}{c} \cosh \gamma_2 h + \frac{\gamma_1 \hat{z_2}}{\gamma_2 \hat{z_1}} \sinh \gamma_2 h \\ \end{array} \right) \end{pmatrix} \quad (2.18e)$$

For Section B :

$$\tilde{Y}_{xx} = \frac{1}{\alpha^2 + \beta^2} (R\alpha^2 - S\beta^2) \quad (2.19a)$$

$$\tilde{Y}_{xz} = \tilde{Y}_{zx} = \frac{\alpha\beta}{\alpha^2 + \beta^2} (R + S) \quad (2.19b)$$

$$\tilde{Y}_{zz} = \frac{1}{\alpha^2 + \beta^2} (-S\alpha^2 + R\beta^2) \quad (2.19c)$$

where

$$R = \left[\begin{array}{c} \left(\frac{\cosh \gamma_2 h + \frac{\gamma_1 \hat{y}_2}{\gamma_2 \hat{y}_1} \sinh \gamma_2 h + \frac{\hat{y}_3}{\gamma_3} \left(\frac{\gamma_1}{\hat{y}_1} \cosh \gamma_2 h + \frac{\gamma_2}{\hat{y}_2} \sinh \gamma_2 h \right)}{\hat{y}_2} \right) \left(\frac{\gamma_3}{\hat{y}_3} \cosh \gamma_3 b + \frac{\gamma_4}{\hat{y}_4} \sinh \gamma_3 b \right) \\ \cdot \left(\frac{\gamma_3}{\hat{z}_3} \cosh \gamma_3 b + \frac{\gamma_4}{\hat{z}_4} \sinh \gamma_3 b \right)^{-1} \\ \cdot \left(\frac{\gamma_1}{\hat{y}_1} \cosh \gamma_2 h + \frac{\gamma_2}{\hat{y}_2} \sinh \gamma_2 h \right)^{-1} \end{array} \right] \quad (2.19d)$$

$$S = \left[\begin{array}{c} \left(\frac{\gamma_1}{\hat{z}_1} \cosh \gamma_2 h + \frac{\gamma_2}{\hat{z}_2} \sinh \gamma_2 h + \frac{\gamma_3}{\hat{z}_3} \left(\cosh \gamma_2 h + \frac{\gamma_1 \hat{z}_2}{\gamma_2 \hat{z}_1} \sinh \gamma_2 h \right) \right) \left(\frac{\gamma_3}{\hat{z}_3} \sinh \gamma_3 b + \frac{\gamma_4}{\hat{z}_4} \cosh \gamma_3 b \right) \\ \cdot \left(\frac{\gamma_3}{\hat{z}_3} \cosh \gamma_3 b + \frac{\gamma_4}{\hat{z}_4} \sinh \gamma_3 b \right)^{-1} \\ \cdot \left(\cosh \gamma_2 h + \frac{\gamma_1 \hat{z}_2}{\gamma_2 \hat{z}_1} \sinh \gamma_2 h \right)^{-1} \end{array} \right] \quad (2.19e)$$

This process of formulating the Green's function is straightforward but rather lengthy, especially when more dielectric layers are used. Therefore, a simpler method of formulation proposed by Itoh [14] will be discussed. This method is fast

and easy while it gives more physical insight into the spectral domain method.

From the form of the inverse Fourier transform

$$\phi(x,y)e^{-j\beta z} = \frac{1}{2\pi} \int_{-\infty}^{\infty} \tilde{\phi}(\alpha, y) e^{-j(\alpha x + \beta z)} d\alpha \quad (2.20)$$

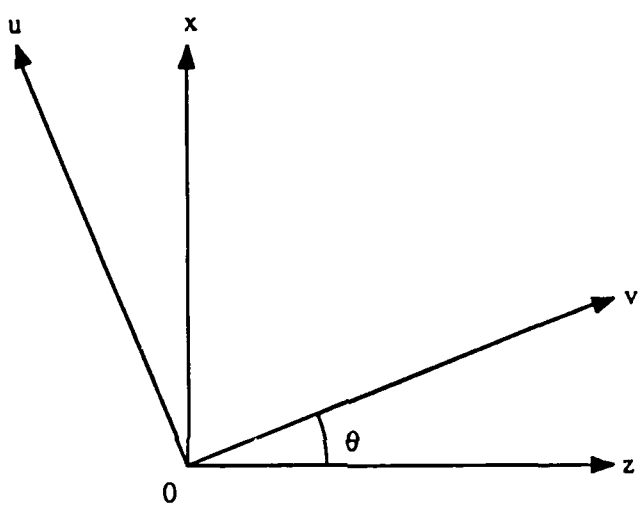
we recognized that the field components in the space domain are the superposition of nonuniform plane waves (spectral waves) propagating in the direction of θ from the z-axis, where $\theta = \cos^{-1}(\beta/\sqrt{\alpha^2 + \beta^2})$. For convenience, we defined in Fig.2.3 a u, v-coordinate system for each spectral wave, which has a rotational relation with the x, z-coordinate system defined by

$$u = x \cos \theta - z \sin \theta \quad (2.21a)$$

$$v = x \sin \theta + z \cos \theta \quad (2.21b)$$

For each θ (i.e., for each α), the nonuniform plane wave may be decomposed into TE-to-y ($H_y \sim$, $E_u \sim$, $H_v \sim$) and TM-to-y ($E_y \sim$, $E_v \sim$, $H_u \sim$) surface waves for which homogeneous boundary conditions apply. Since the spectral current $J_u \sim$ is due only to the discontinuity of the tangential $H_v \sim$ component in the TE fields, and $J_v \sim$ is due only to TM fields, they can be dealt with independently.

For surface wave modes, the characteristic equations may be obtained from the transverse resonance conditions of the equivalent transmission line circuits. Fig.2.4 shows the equivalent circuits for both TE and TM cases. The characteristic admittances in each region are



$$\begin{aligned}u &= x\cos\theta - z\sin\theta \\v &= x\sin\theta + z\cos\theta\end{aligned}$$

Fig.2.3 Coordinate transformation.

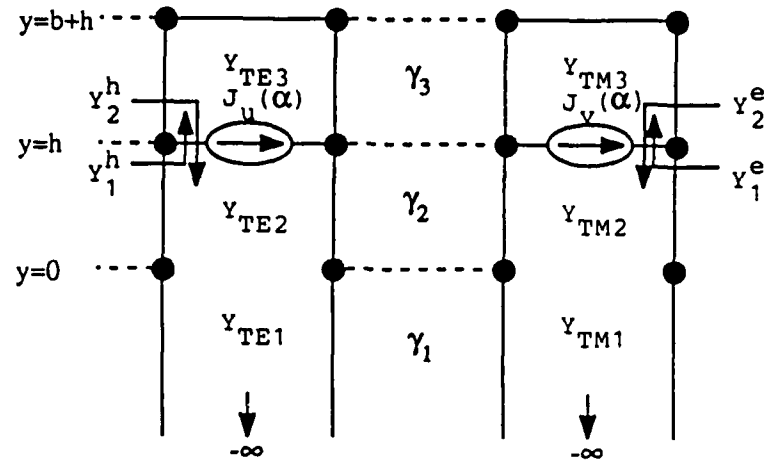
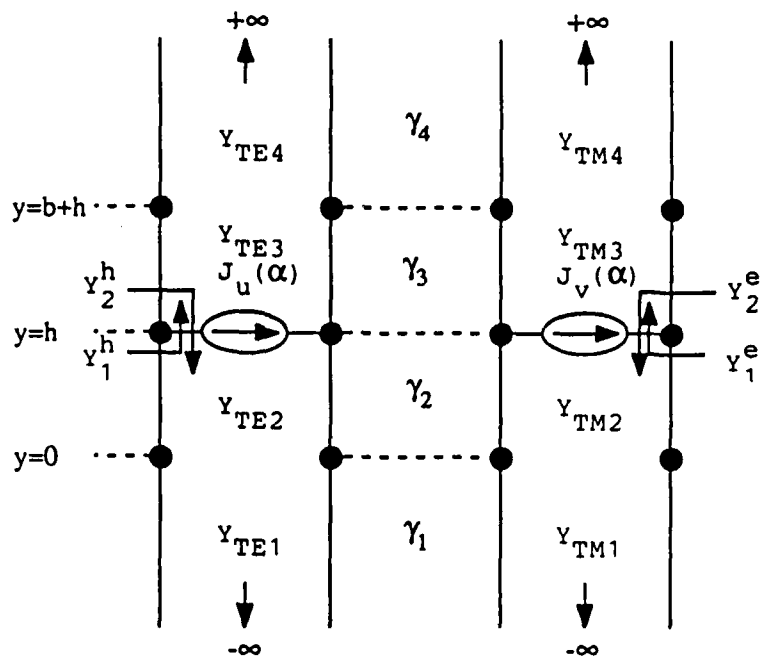
Section ASection B

Fig.2.4 Transverse equivalent circuits for crosstie overlay coplanar waveguide.

$$Y_{TEi} = \frac{\tilde{H}_{vi}}{\tilde{E}_{ui}} = \frac{\gamma_i}{z_i} \quad (2.22a)$$

$$Y_{TMI} = \frac{\tilde{H}_{ui}}{\tilde{E}_{vi}} = \frac{y_i}{\gamma_i} \quad (2.22b)$$

$i=1,2,3$ for Section A
 $=1,2,3,4$ for Section B.

All the boundary conditions for the TE and TM waves are readily incorporated in the equivalent circuits. For instance, the conducting plane at $y=b+h$ is represented by a short circuit. The electric fields E_u and E_v are continuous at $y=h$ and are related to the currents via

$$\tilde{J}_u(\alpha) = Y^{-h}(\alpha, \beta) \tilde{E}_u(\alpha) \quad (2.23a)$$

$$\tilde{J}_v(\alpha) = Y^{-e}(\alpha, \beta) \tilde{E}_v(\alpha) \quad (2.23b)$$

Y^{-h} and Y^{-e} are the input admittances looking into the equivalent circuits from the current sources at $y=h$, and are given by

$$Y^{-h}(\alpha, \beta) = Y_1^h + Y_2^h \quad (2.24a)$$

$$Y^{-e}(\alpha, \beta) = Y_1^e + Y_2^e \quad (2.24b)$$

where Y_1^h and Y_2^h are the input admittances looking upward and downward, respectively, at $y=h$ in the TE equivalent circuit, and Y_1^e and Y_2^e are input admittances in the TM circuit :

For Section A:

$$Y_1^h = Y_{TE3} \coth \gamma_3 b, \quad Y_2^h = Y_{TE2} \frac{Y_{TE1} + Y_{TE2} \tanh \gamma_2 h}{Y_{TE2} + Y_{TE1} \tanh \gamma_2 h} \quad (2.25a)$$

$$Y_1^e = Y_{TM3} \coth \gamma_3 b, \quad Y_2^e = Y_{TM2} \frac{Y_{TM1} + Y_{TM2} \tanh \gamma_2 h}{Y_{TM2} + Y_{TM1} \tanh \gamma_2 h} \quad (2.25b)$$

For Section B :

$$Y_1^h = Y_{TE3} \frac{Y_{TE4} + Y_{TE3} \tanh \gamma_3 b}{Y_{TE3} + Y_{TE4} \tanh \gamma_3 b}, \quad Y_2^h = Y_{TE2} \frac{Y_{TE1} + Y_{TE2} \tanh \gamma_2 h}{Y_{TE2} + Y_{TE1} \tanh \gamma_2 h} \quad (2.26a)$$

$$Y_1^e = Y_{TM3} \frac{Y_{TM4} + Y_{TM3} \tanh \gamma_3 b}{Y_{TM3} + Y_{TM4} \tanh \gamma_3 b}, \quad Y_2^e = Y_{TM2} \frac{Y_{TM1} + Y_{TM2} \tanh \gamma_2 h}{Y_{TM2} + Y_{TM1} \tanh \gamma_2 h} \quad (2.26b)$$

The final step is to derive the relation (2.2a,b) in the x, z-coordinate system from equations (2.23a,b) via a coordinate transformation. Because the transformation is a simple coordinate rotation (2.21a,b), $E_x \sim$ and $E_z \sim$ ($J_x \sim$ and $J_z \sim$) are linear combinations of $E_u \sim$ and $E_v \sim$ ($J_u \sim$ and $J_v \sim$). After the transformation, the admittance matrix elements in (2.2a,b) are found to be

$$Y_{xx}^-(\alpha, \beta) = \cos^2 \theta Y^h + \sin^2 \theta Y^e \quad (2.27a)$$

$$Y_{xz}^-(\alpha, \beta) = Y_{zx}^-(\alpha, \beta) = \sin \theta \cos \theta (Y^e - Y^h) \quad (2.27b)$$

$$Y_{zz}^-(\alpha, \beta) = \sin^2 \theta Y^h + \cos^2 \theta Y^e \quad (2.27c)$$

$$\text{where } \sin \theta = \frac{\alpha}{\sqrt{\alpha^2 + \beta^2}}, \quad \cos \theta = \frac{\beta}{\sqrt{\alpha^2 + \beta^2}}.$$

It is easily shown that this equation (2.27) is identical to equation (2.18) or (2.19).

Now that we have derived the equations corresponding to the integral equations (2.1a,b), with closed form expressions for the Green's functions in the spectral domain, the solution of the propagation constant β in the z-direction is to be

calculated. To this end, Galerkin's method is applied by expanding the electric field components $E_x \sim$ and $E_z \sim$ in terms of known basis functions $E_{xn} \sim$ and $E_{zn} \sim$ as follows :

$$\tilde{E}_x(\alpha) = \sum_{n=0}^M c_n \tilde{E}_{xn}(\alpha) \quad (2.28a)$$

$$\tilde{E}_z(\alpha) = \sum_{n=1}^N d_n \tilde{E}_{zn}(\alpha) \quad (2.28b)$$

where c_n and d_n are unknown coefficients. The basis functions $E_{xn} \sim$ and $E_{zn} \sim$ must be chosen such that their inverse Fourier transforms are nonzero only in the slots. After substituting (2.28a,b) into (2.2a,b) and taking the inner products of the resultant equations with the basis functions $E_{xn} \sim$ and $E_{zn} \sim$, we obtain the linear simultaneous equations:

$$\sum_{n=0}^M K_{mn}^{(1,1)} c_n + \sum_{n=1}^N K_{mn}^{(1,2)} d_n = 0 , \quad m=0,1,2,\dots,M \quad (2.29a)$$

$$\sum_{n=0}^M K_{mn}^{(2,1)} c_n + \sum_{n=1}^N K_{mn}^{(2,2)} d_n = 0 , \quad m=1,2,3,\dots,N \quad (2.29b)$$

where

$$K_{mm}^{(1,1)} = \int_{-\infty}^{\infty} \tilde{E}_{xm}(\alpha) \tilde{Y}_{xx}(\alpha, \beta) \tilde{E}_{xn}(\alpha) d\alpha$$

$$K_{mn}^{(1,2)} = \int_{-\infty}^{\infty} \tilde{E}_{xm}(\alpha) \tilde{Y}_{xz}(\alpha, \beta) \tilde{E}_{zn}(\alpha) d\alpha$$

$$K_{mn}^{(2,1)} = \int_{-\infty}^{\infty} E_{zm}(\alpha) Y_{zx}(\alpha, \beta) E_{xn}(\alpha) d\alpha$$

$$K_{mn}^{(2,2)} = \int_{-\infty}^{\infty} E_{zm}(\alpha) Y_{zz}(\alpha, \beta) E_{zn}(\alpha) d\alpha$$

Notice that the right hand sides of (2.2a,b) are eliminated by this procedure. This can be verified by using Parseval's theorem that

$$\int_{-\infty}^{\infty} E_{xm}(\alpha) J_x(\alpha) d\alpha = \int_{-\infty}^{\infty} E_{xm}(x) J_x(x) = 0 \quad (2.30)$$

The above relation is true since $E_{xm}(x)$ [the inverse transform of $E_{xm}(\alpha)$] and $J_x(x)$ are nonzero in the complementary regions of x at $y=h$.

Finally, the propagation constant β is obtained by solving the system of simultaneous equations, (2.29). Since this set of equations is homogeneous, non-trivial solutions can be obtained only when the determinant of its coefficient matrix is equal to zero, i.e., the matrix is singular. This results in a characteristic equation, from which β is obtained.

2.3.2 CHARACTERISTIC IMPEDANCE

Due to the non-TEM nature of the analyzed structure, the definition of characteristic impedance is not unique. Three commonly used definitions of the characteristic impedance (Z_C) are based on

1. Voltage-current, $Z_c = V/I$ (2.31a)

$$2. \text{ Power-current, } Z_c = 2P/I^2 \quad (2.31b)$$

$$3. \text{ Power-voltage, } Z_c = V^2/2P \quad (2.31c)$$

where P is the transmitted power, V is the voltage across the slot, and I is the current on the transmission lines. For switching applications, the characteristic impedance based on voltage and current in the transmission line is preferred [21]. For some other applications, the power-voltage definition of characteristic impedance is used [22]. However, the most suitable definition for the structures analyzed here, following the argument given in [23], is

$$Z_c = \frac{V^2}{2P_{avg}} \quad (2.32)$$

where P_{avg} is the time-averaged power flow. The expression for the voltage V across the slot is given by

$$V = \int_{\text{slot}} E_x(x) dx \quad (2.33)$$

and the time-averaged power flow on the transmission line is given by

$$P_{avg} = \text{Re} \left(\iint_{-\infty}^{\infty} \tilde{E}_x \tilde{H}_z^* dxdy \right) \quad (2.34)$$

Since the limits of integration are infinite, Parseval's theorem may be used to transform the expression into the spectral domain as

$$P_{avg} = \text{Re} \left(\iint_{-\infty}^{\infty} [\tilde{E}_x(\alpha, y) \tilde{H}_y^*(\alpha, y) - \tilde{E}_y(\alpha, y) \tilde{H}_x^*(\alpha, y)] d\alpha dy \right). \quad (2.35)$$

Expressions for the electric and magnetic fields in each region are given by equations

(2.9)~(2.13). Since the y -dependence of these expressions is simple, the integration with respect to y may be performed analytically.

Note that the calculation of P_{avg} requires the values of $E_x \sim$ and $E_z \sim$ to be known, i.e., the expansion coefficients c_n and d_n obtained by solving the equations (2.29a,b) for a known β .

Finally, the voltage V is computed. This involves simply the integration of the assumed electric field distribution across the slot and can be done analytically.

2.3.3 CHOICE OF BASIS FUNCTIONS

Any kind of basis function may be used as long as it is nonzero only in the slot regions. However, due to the variational nature of the approach, the efficiency and accuracy of this method depend greatly on the choice of basis functions. In this study, the basis functions are selected in accordance with the following criteria :

(1) For rapid convergence of the solution the functions should satisfy the edge condition [24] which requires that $E_z(x)$ behaves like $|x-x_e|^{1/2}$ near the edge x_e of a strip, whereas $E_x(x)$ approaches x_e with the singularity $|x-x_e|^{-1/2}$. This ensures the proper singular behavior of the field for any degree of solution accuracy and is necessary to achieve fast convergence of the characteristic impedance values, which quite sensitively depend on the field distribution.

(2) The set of functions E_{xi} , E_{zi} should be complete to enable approximation of the exact solution to any degree desired simply by increasing the number of terms

of the expansion. In this way the numerical solutions can be easily checked for their convergence.

(3) All the physical insight available should be incorporated into the choice of expansion functions so that the combination of them can closely represent a modal field distribution and the matrix size can be held small for the given required accuracy.

(4) It is desirable that the transforms $E_{xi} \sim$ and $E_{zi} \sim$ be available in a fairly simple analytical form.

With the above considerations in mind, the following set of functions are employed [25]

$$E_{xn}(x) = \begin{cases} \frac{\cos[n\pi(x+\frac{s+w}{2})/w] - \cos[n\pi(x-\frac{s+w}{2})/w]}{\sqrt{1 - \left[\frac{2(x+\frac{s+w}{2})}{w}\right]^2}} & n=0,2,4,\dots \\ \frac{\sin[n\pi(x+\frac{s+w}{2})/w] + \sin[n\pi(x-\frac{s+w}{2})/w]}{\sqrt{1 - \left[\frac{2(x+\frac{s+w}{2})}{w}\right]^2}} & n=1,3,5,\dots \end{cases} \quad (2.36a)$$

$$E_{zn}(x) = \begin{cases} \frac{\cos\left[n\pi(x+\frac{s+w}{2})/w\right] + \cos\left[n\pi(x-\frac{s+w}{2})/w\right]}{1 - \left[\frac{2(x+\frac{s+w}{2})}{w}\right]^2} & n=1,3,5,\dots \\ \frac{\sin\left[n\pi(x+\frac{s+w}{2})/w\right] - \sin\left[n\pi(x-\frac{s+w}{2})/w\right]}{1 - \left[\frac{2(x-\frac{s+w}{2})}{w}\right]^2} & n=2,4,6,\dots \end{cases} \quad (2.36b)$$

Note that the first and second terms in these functions are defined over the slot at $-(s+2w)/2 \leq x \leq -s/2$ and $s/2 \leq x \leq (s+2w)/2$, respectively. For odd mode (coplanar waveguide mode) solutions, complete figures for the first four basis functions are shown in Fig.2.5. The Fourier transforms of the entire set are

$$\tilde{E}_{xn}(\alpha) = \begin{cases} -j\frac{\pi w}{2} \sin\frac{\alpha(s+w)}{2} \left[J_0\left(\left|\frac{\alpha w}{2} + \frac{n\pi}{2}\right|\right) + J_0\left(\left|\frac{\alpha w}{2} - \frac{n\pi}{2}\right|\right) \right] & n=0,2,4,\dots \\ -j\frac{\pi w}{2} \cos\frac{\alpha(s+w)}{2} \left[J_0\left(\left|\frac{\alpha w}{2} + \frac{n\pi}{2}\right|\right) - J_0\left(\left|\frac{\alpha w}{2} - \frac{n\pi}{2}\right|\right) \right] & n=1,3,5,\dots \end{cases} \quad (2.37a)$$

$$\tilde{E}_{zn}(\alpha) = \begin{cases} \frac{\pi w}{2} \cos\frac{\alpha(s+w)}{2} \left[J_0\left(\left|\frac{\alpha w}{2} + \frac{n\pi}{2}\right|\right) + J_0\left(\left|\frac{\alpha w}{2} - \frac{n\pi}{2}\right|\right) \right] & n=1,3,5,\dots \\ \frac{\pi w}{2} \sin\frac{\alpha(s+w)}{2} \left[J_0\left(\left|\frac{\alpha w}{2} + \frac{n\pi}{2}\right|\right) - J_0\left(\left|\frac{\alpha w}{2} - \frac{n\pi}{2}\right|\right) \right] & n=2,4,6,\dots \end{cases} \quad (2.37b)$$

where J_0 denotes the zero-order Bessel function of the first kind.

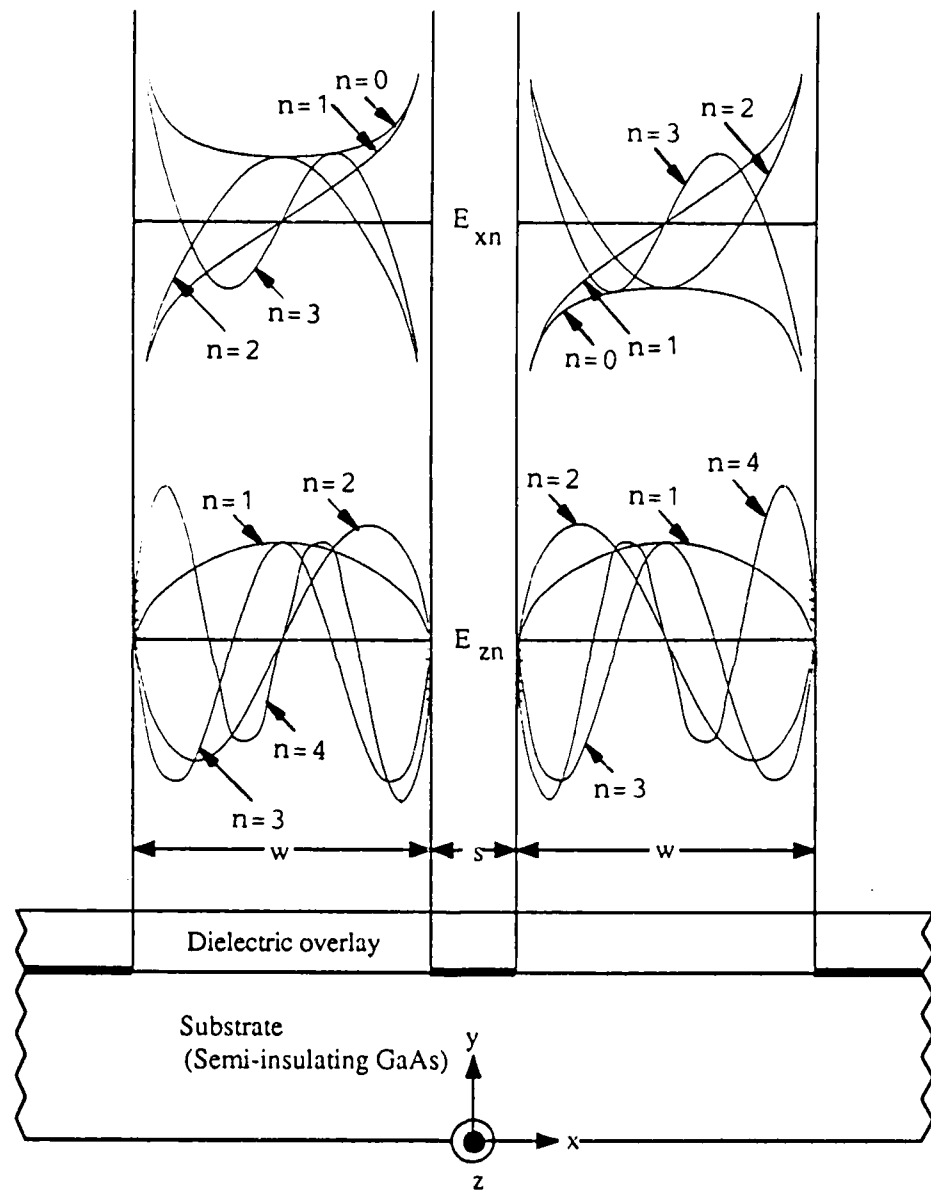


Fig.2.5 Field distribution of the first four basis functions.

2.4 FLOQUET'S THEOREM AND A PERIODIC CROSSTIE OVERLAY SLOW-WAVE COPLANAR WAVEGUIDE

The basis for a study of periodic transmission systems is a theorem due to a French mathematician, Floquet. This theorem may be stated as follows: For a given mode of propagation at a given steady-state frequency, the fields at one cross section differ from those a period away only by a complex constant. The theorem is true whether or not the structure contains loss as long as it is periodic. The proof of the theorem lies in the fact that when a structure having infinite length is displaced along its axis by one period, it cannot be distinguished from its original structure.

Fig.2.6 is the transmission line equivalent circuit of a periodic crosstie overlay slow-wave CPW. In this figure, one unit cell of the periodic slow-wave CPW consists of a Section A (with crosstie strip) with length l_A , complex propagation constant γ_A ($\gamma_A = \alpha_A + j\beta_A$, α_A and β_A are the attenuation constant and the phase constant of Section A, respectively.), characteristic impedance Z_A ; and a Section B (without crosstie strip) with length l_B , complex propagation constant γ_B ($\gamma_B = \alpha_B + j\beta_B$, α_B and β_B are the attenuation constant and the phase constant of Section B, respectively.), and characteristic impedance Z_B . The length for a unit cell is thus $l = l_A + l_B$. Based on Floquet's theorem, if the periodic structure is capable of supporting a propagating wave, it is necessary for the voltage and current at the $(n+1)$ st terminal to be equal to the voltage and current at the n th terminal, apart from a phase delay due to a finite propagation time. Thus we assume that

$$V_{n+1} = e^{-\gamma l} V_n = e^{-\gamma(l_A + l_B)} V_n \quad (2.38a)$$

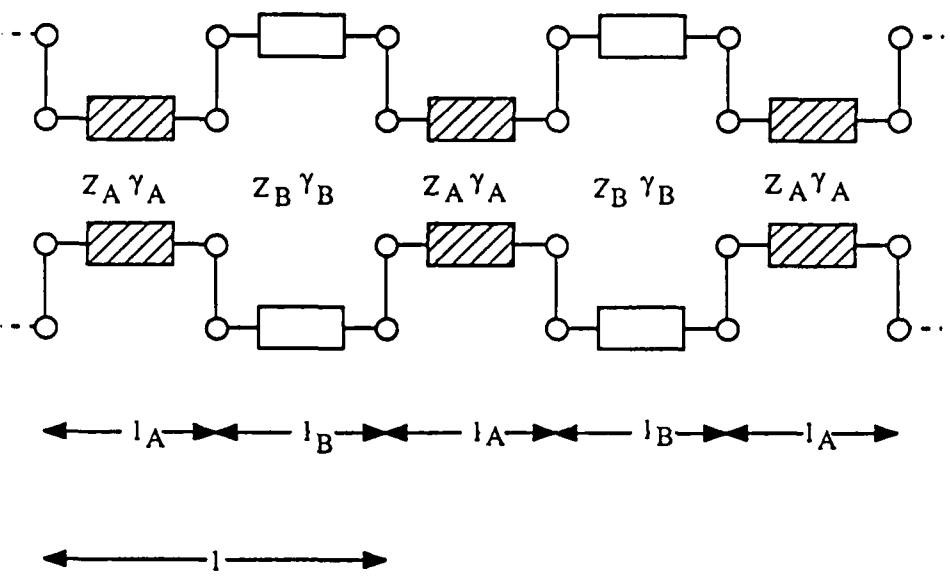


Fig.2.6 Periodic transmission line model of a crosstie overlay slow-wave CPW.

$$I_{n+1} = e^{-\gamma l} I_n = e^{-\gamma(l_A + l_B)} I_n \quad (2.38b)$$

where $\gamma = \alpha + j\beta$ is the complex propagation constant for the periodic structure (α is the attenuation constant and β is the phase constant). In terms of the transmission matrix for a unit cell, we now have

$$\begin{bmatrix} V_n \\ I_n \end{bmatrix} = \begin{bmatrix} A_{\text{unit}} & B_{\text{unit}} \\ C_{\text{unit}} & D_{\text{unit}} \end{bmatrix} \begin{bmatrix} V_{n+1} \\ I_{n+1} \end{bmatrix} = e^{\gamma l} \begin{bmatrix} V_{n+1} \\ I_{n+1} \end{bmatrix} = e^{\gamma(l_A + l_B)} \begin{bmatrix} V_{n+1} \\ I_{n+1} \end{bmatrix} \quad (2.39)$$

where the transmission matrix for a unit cell is given by

$$\begin{bmatrix} A_{\text{unit}} & B_{\text{unit}} \\ C_{\text{unit}} & D_{\text{unit}} \end{bmatrix} = \begin{bmatrix} A_A & B_A \\ C_A & D_A \end{bmatrix} \begin{bmatrix} A_B & B_B \\ C_B & D_B \end{bmatrix} = \begin{bmatrix} \cosh \gamma_A l_A & Z_A \sinh \gamma_A l_A \\ \frac{1}{Z_A} \sinh \gamma_A l_A & \cosh \gamma_A l_A \end{bmatrix} \begin{bmatrix} \cosh \gamma_B l_B & Z_B \sinh \gamma_B l_B \\ \frac{1}{Z_B} \sinh \gamma_B l_B & \cosh \gamma_B l_B \end{bmatrix}$$

$$= \begin{bmatrix} \cosh \gamma_A l_A \cosh \gamma_B l_B + \frac{Z_A}{Z_B} \sinh \gamma_A l_A \sinh \gamma_B l_B & Z_A \sinh \gamma_A l_A \cosh \gamma_B l_B + Z_B \cosh \gamma_A l_A \sinh \gamma_B l_B \\ \frac{1}{Z_A} \sinh \gamma_A l_A \cosh \gamma_B l_B + \frac{1}{Z_B} \cosh \gamma_A l_A \sinh \gamma_B l_B & \cosh \gamma_A l_A \cosh \gamma_B l_B + \frac{Z_B}{Z_A} \sinh \gamma_A l_A \sinh \gamma_B l_B \end{bmatrix} \quad (2.40)$$

From equation (2.39) we have

$$\left(\begin{bmatrix} A_{\text{unit}} & B_{\text{unit}} \\ C_{\text{unit}} & D_{\text{unit}} \end{bmatrix} - \begin{bmatrix} e^{\gamma(l_A + l_B)} & 0 \\ 0 & e^{\gamma(l_A + l_B)} \end{bmatrix} \right) \begin{bmatrix} V_{n+1} \\ I_{n+1} \end{bmatrix} = 0 \quad (2.41)$$

This equation is a matrix eigenvalue equation for γ . A nontrivial solution for V_{n+1} , I_{n+1} exists only if the determinant vanishes. Hence

$$\begin{vmatrix} A_{\text{unit}} - e^{\gamma(l_A + l_B)} & B_{\text{unit}} \\ C_{\text{unit}} & D_{\text{unit}} - e^{\gamma(l_A + l_B)} \end{vmatrix} = A_{\text{unit}} D_{\text{unit}} - B_{\text{unit}} C_{\text{unit}} + e^{2\gamma(l_A + l_B)} - e^{-2\gamma(l_A + l_B)} (A_{\text{unit}} + D_{\text{unit}}) = 0 \quad (2.42)$$

For a reciprocal network the determinant $A_{\text{unit}}D_{\text{unit}} - B_{\text{unit}}C_{\text{unit}}$ of the transmission matrix equals unity [26]; so we obtain

$$\cosh \gamma l = \frac{A_{\text{unit}} + D_{\text{unit}}}{2} = \cosh \gamma_A l_A \cosh \gamma_B l_B + \frac{1}{2} \left(\frac{Z_A}{Z_B} + \frac{Z_B}{Z_A} \right) \sinh \gamma_A l_A \sinh \gamma_B l_B \quad (2.43)$$

This is the dispersion equation for an infinitely long uniform periodic crosstie overlay slow-wave CPW.

Another parameter of importance in connection with a periodic structure is the characteristic impedance Z_p presented to the voltage and current waves at the reference terminal plane, i.e., input terminals of a unit cell. An expression for Z_p may be obtained from (2.41) which may be written as

$$(A_{\text{unit}} - e^{\gamma l}) V_{n+1} = -B_{\text{unit}} I_{n+1} \quad (2.44a)$$

$$-C_{\text{unit}} V_{n+1} = (D_{\text{unit}} - e^{\gamma l}) I_{n+1} \quad (2.44b)$$

$$Z_p = \frac{V_{n+1}}{I_{n+1}} = \frac{-B_{\text{unit}}}{A_{\text{unit}} - e^{\gamma l}} = -\frac{D_{\text{unit}} - e^{\gamma l}}{C_{\text{unit}}} \quad (2.45)$$

Replacing $2e^{\gamma l}$ by $A_{\text{unit}} + D_{\text{unit}} \pm [(A_{\text{unit}} + D_{\text{unit}})^2 - 4]^{1/2}$ from (2.42), we obtain

$$Z_p^{\pm} = \frac{2B_{\text{unit}}}{D_{\text{unit}} - A_{\text{unit}} \pm \sqrt{(A_{\text{unit}} + D_{\text{unit}})^2 - 4}} \quad (2.46)$$

where the upper and lower signs refer to propagation in the +z and -z directions, respectively. For a symmetrical network, $A_{\text{unit}} = D_{\text{unit}}$, and since $A_{\text{unit}}D_{\text{unit}} - B_{\text{unit}}C_{\text{unit}} = 1$, we have $A_{\text{unit}}^2 - 1 = B_{\text{unit}}C_{\text{unit}}$. In this case (2.46) reduces to

$$\begin{aligned} Z_p^\pm &= \frac{2B_{\text{unit}}}{\pm\sqrt{4A_{\text{unit}}^2 - 4}} = \pm\sqrt{\frac{B_{\text{unit}}}{C_{\text{unit}}}} \\ &= \pm\sqrt{\frac{Z_A \sinh \gamma_A l_A \cosh \gamma_B l_B + Z_B \cosh \gamma_A l_A \sinh \gamma_B l_B}{\frac{1}{Z_A} \sinh \gamma_A l_A \cosh \gamma_B l_B + \frac{1}{Z_B} \cosh \gamma_A l_A \sinh \gamma_B l_B}} \end{aligned} \quad (2.47)$$

In general, for a lossless structure, $Z_p^- = -(Z_p^+)^*$ (* denotes the complex conjugate) in the passband, since $|A_{\text{unit}} + D_{\text{unit}}| < 2$, as (2.43) shows.

Finally, it is well to note that in this approach, the effect of the geometrical discontinuity at the junction of two sections is assumed to be negligible, although it can, however, contribute a little.

2.5 PROPAGATION CHARACTERISTICS OF A CROSSTIE OVERLAY SLOW-WAVE COPLANAR WAVEGUIDE WITH LOSSLESS CONDUCTORS

To check the validity of the spectral domain analysis mentioned in Section 2.3, the convergence of solutions has been studied by increasing the number of basis functions used. In this study, it is found that good results can be obtained by using seven basis functions that represent axial and transverse electric fields in the slot. Typical results for the propagation constant and the characteristic impedance show convergence accuracy within 0.5% and 1%, respectively. Of course, the

convergence accuracy could be further enhanced if more basis functions were used. Based on this scheme, the characteristics of constituent sections in the crosstie overlay CPW have been studied for a wide range of geometric parameters.

2.5.1 GENERAL PROPAGATION CHARACTERISTICS OF THE CONSTITUENT SECTIONS

In Section A, the capacitance per unit length is greatly enhanced due to the existence of the metal crosstie and the thin dielectric overlay. The inherent TEM nature of the significant parallel plate capacitor created between the metal crosstie and the center conductor of the CPW results in an almost-nondispersive propagation as well as a quite low characteristic impedance in Section A. In contrast, without the metal crosstie, Section B exhibits much higher inductance per unit length and characteristic impedance in conjunction with more dispersive propagation characteristics. These behaviors are shown in Figs.2.7(a) and 2.7(b).

2.5.2 EFFECTS OF THE CROSS-SECTIONAL CONFIGURATION OF A COPLANAR WAVEGUIDE AND THE THICKNESS OF THE DIELECTRIC OVERLAY

In Figs.2.8(a), 2.8(b), 2.9(a) and 2.9(b), it is observed that for a fixed distance between two ground planes $s+2w$ in a CPW, both the propagation constant and the characteristic impedance increase in Section A (less capacitive), whereas the propagation constant decreases firstly then increases and the characteristic impedance increases in Section B (more inductive) as the slot width w increases. On the other

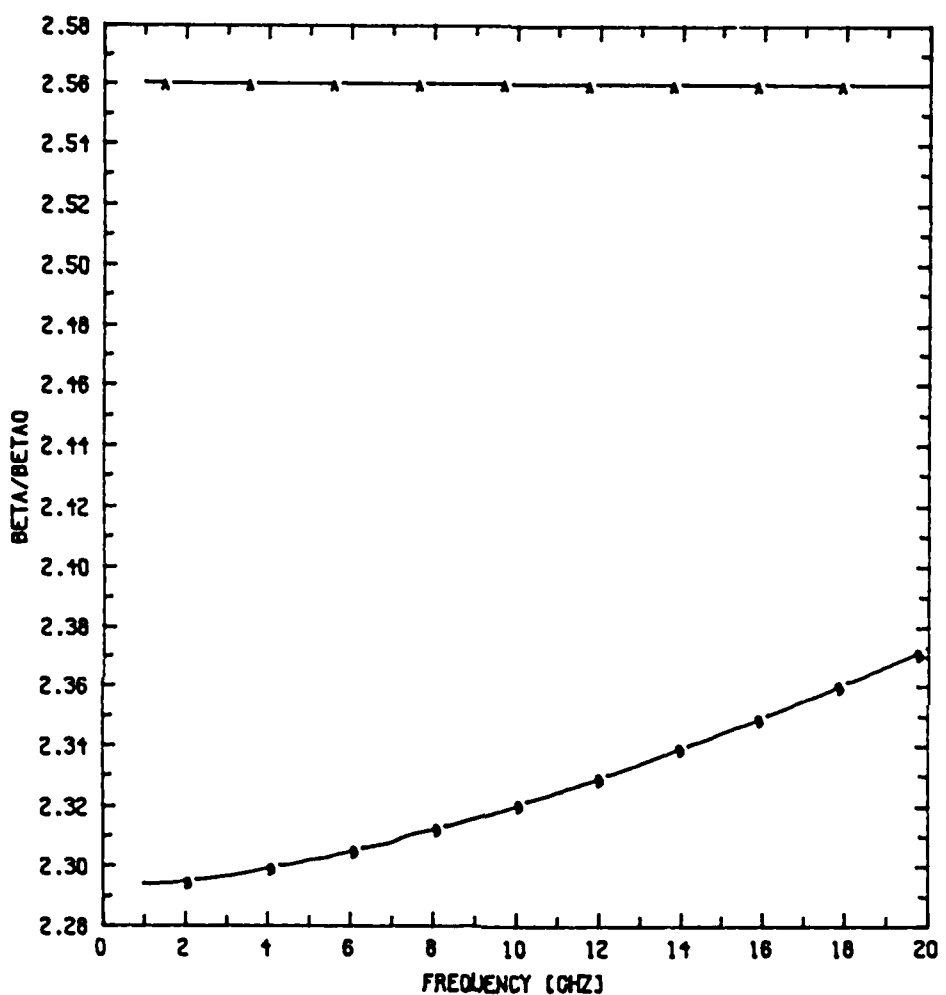


Fig.2.7(a) Normalized propagation constant versus frequency of sections A and B in a crosstie overlay slow-wave CPW.

$s = .15\text{mm}$, $w = .745\text{mm}$, $b = .001\text{mm}$, $h = .35\text{mm}$, $\epsilon_r = 12.9$ (S.I.GaAs), $\epsilon_r' = 6.5(\text{Si}_3\text{N}_4)$, Curve A----Section A, Curve B----Section B.

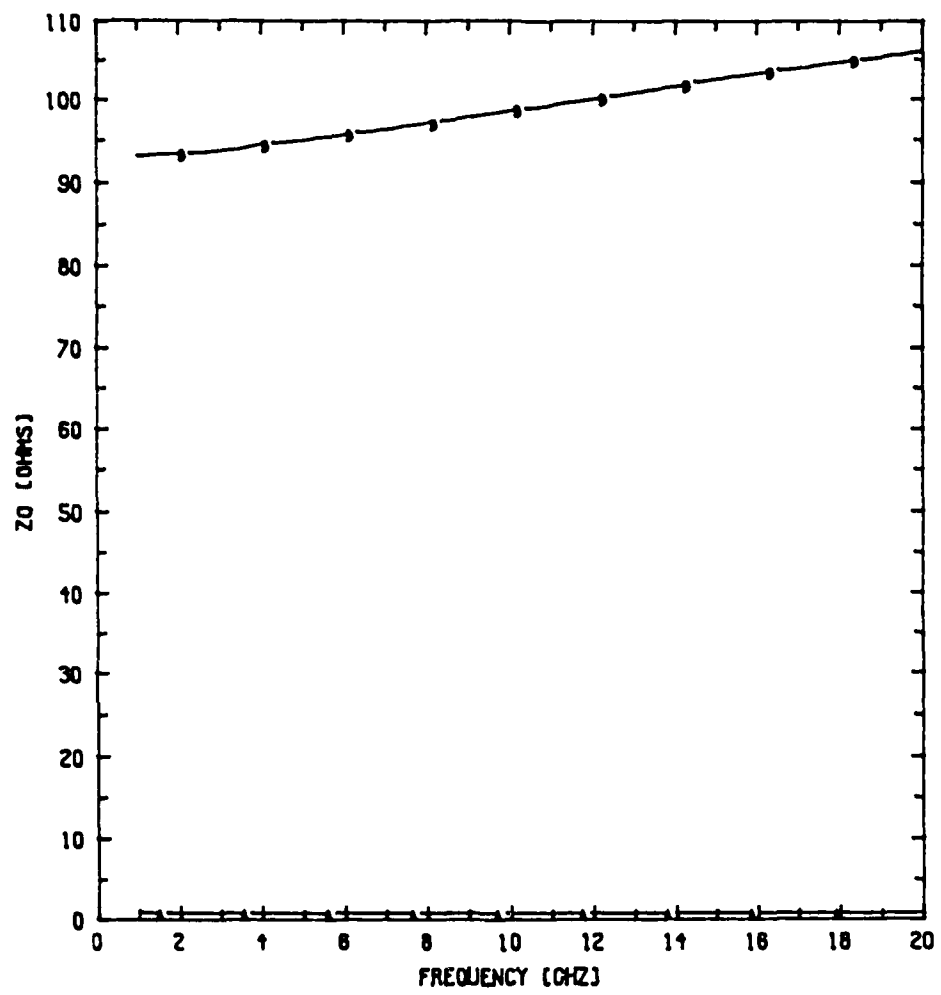


Fig.2.7(b) Characteristic impedance versus frequency of sections A and B in a crosstie overlay slow-wave CPW.

s=.15mm, w=.745mm, b=.001mm, h=.35mm, $\epsilon_r=12.9$
(S.I.GaAs), $\epsilon_r'=6.5(\text{Si}_3\text{N}_4)$, Curve A---Section A, Curve B---Section B.

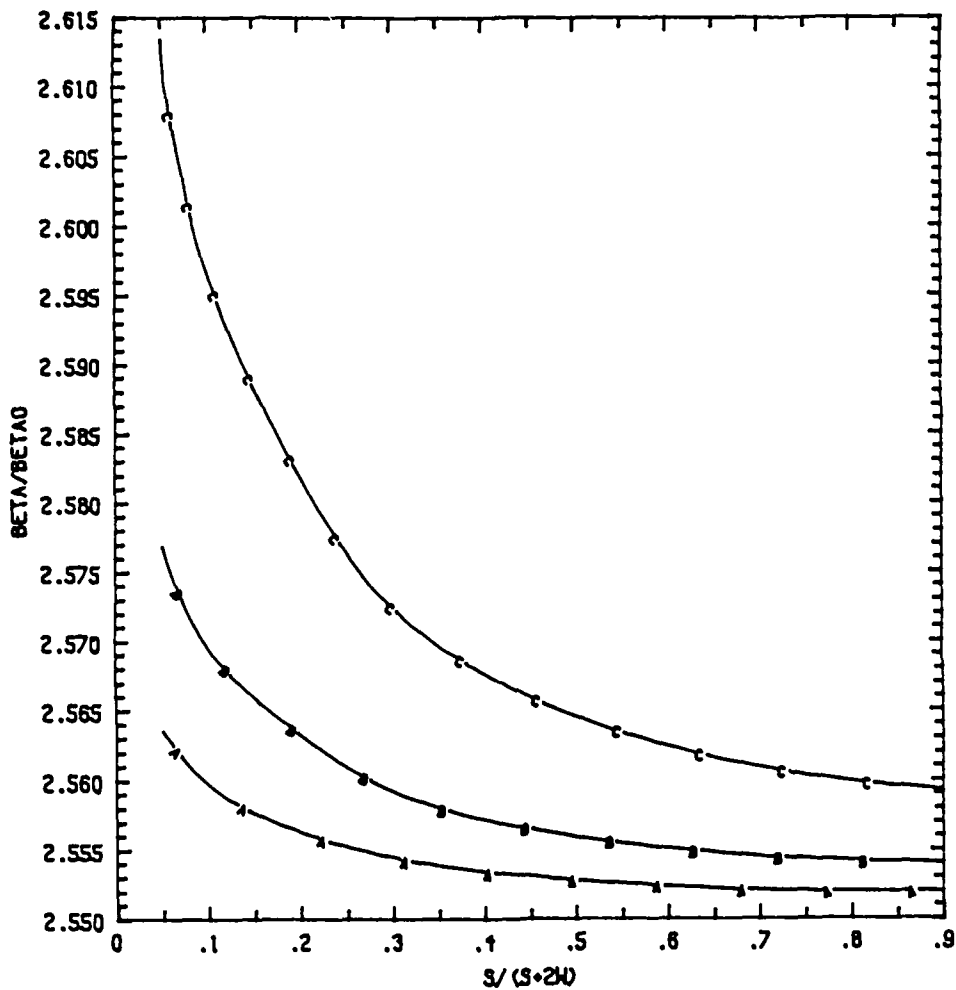


Fig.2.8(a) Normalized propagation constant versus aspect ratio of Section A
with different overlay thicknesses.

$s+2w=1.64\text{mm}$, $b=.001\text{mm}$, $\epsilon_r=12.9$ (S.I.GaAs), $\epsilon_r'=6.5(\text{Si}_3\text{N}_4)$,
 $f=10\text{GHz}$, Curve A--- $b=.001\text{mm}$, Curve B--- $b=.002\text{mm}$, Curve
C--- $b=.005\text{mm}$.

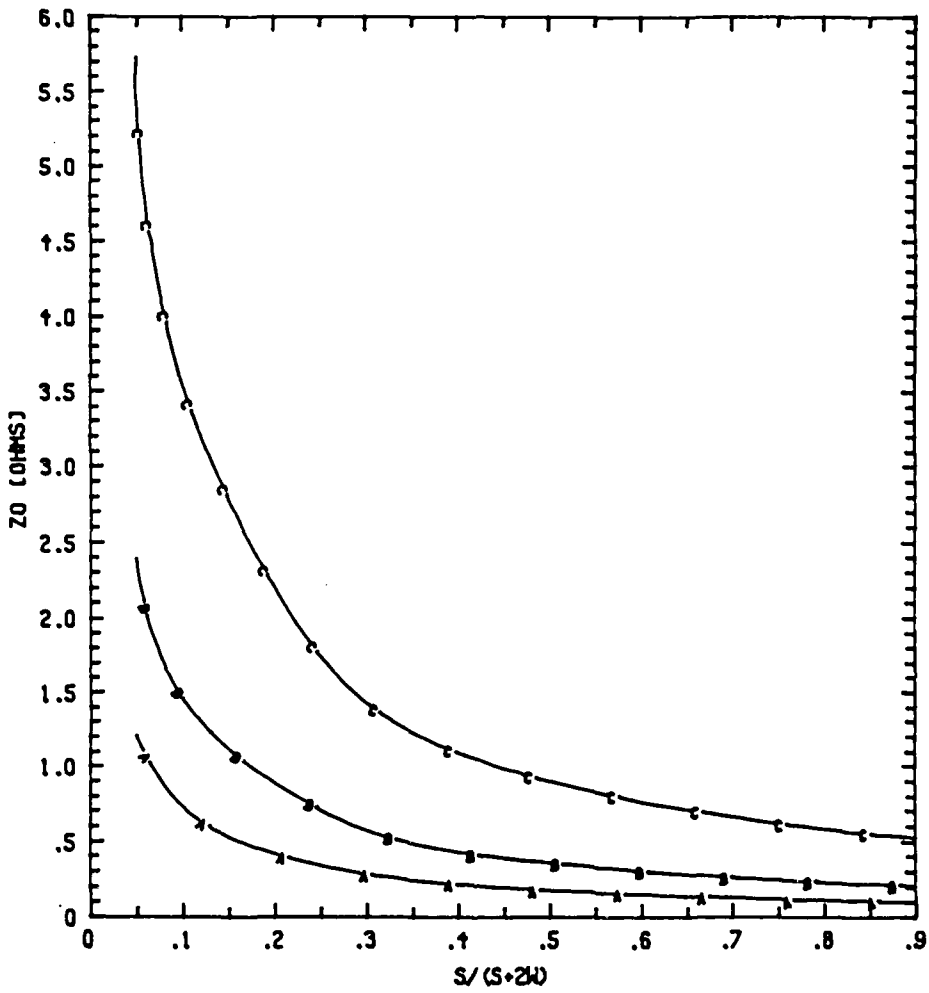


Fig.2.8(b) Characteristic impedance versus aspect ratio of Section A with different overlay thicknesses.

$s+2w=1.64\text{mm}$, $b=.001\text{mm}$, $\epsilon_r=12.9$ (S.I.GaAs), $\epsilon_r'=6.5$ (Si_3N_4), $f=10\text{GHz}$, Curve A--- $b=.001\text{mm}$, Curve B--- $b=.002\text{mm}$, Curve C--- $b=.005\text{mm}$.

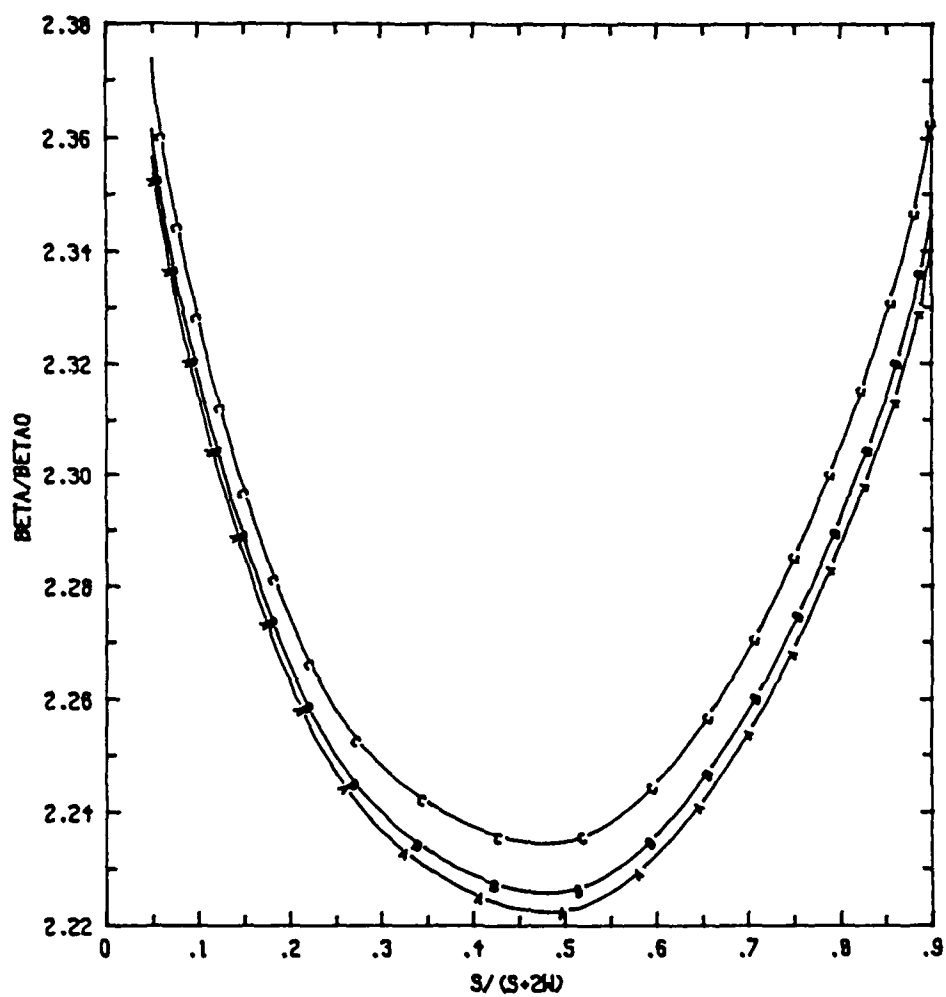


Fig.2.9(a) Normalized propagation constant versus aspect ratio of Section B with different overlay thicknesses.

$s+2w=1.64\text{mm}$, $b=.001\text{mm}$, $\epsilon_r=12.9$ (S.I.GaAs), $\epsilon_r'=6.5$ (Si₃N₄),
 $f=10\text{GHz}$, Curve A--- $b=.001\text{mm}$, Curve B--- $b=.002\text{mm}$, Curve
C--- $b=.005\text{mm}$.

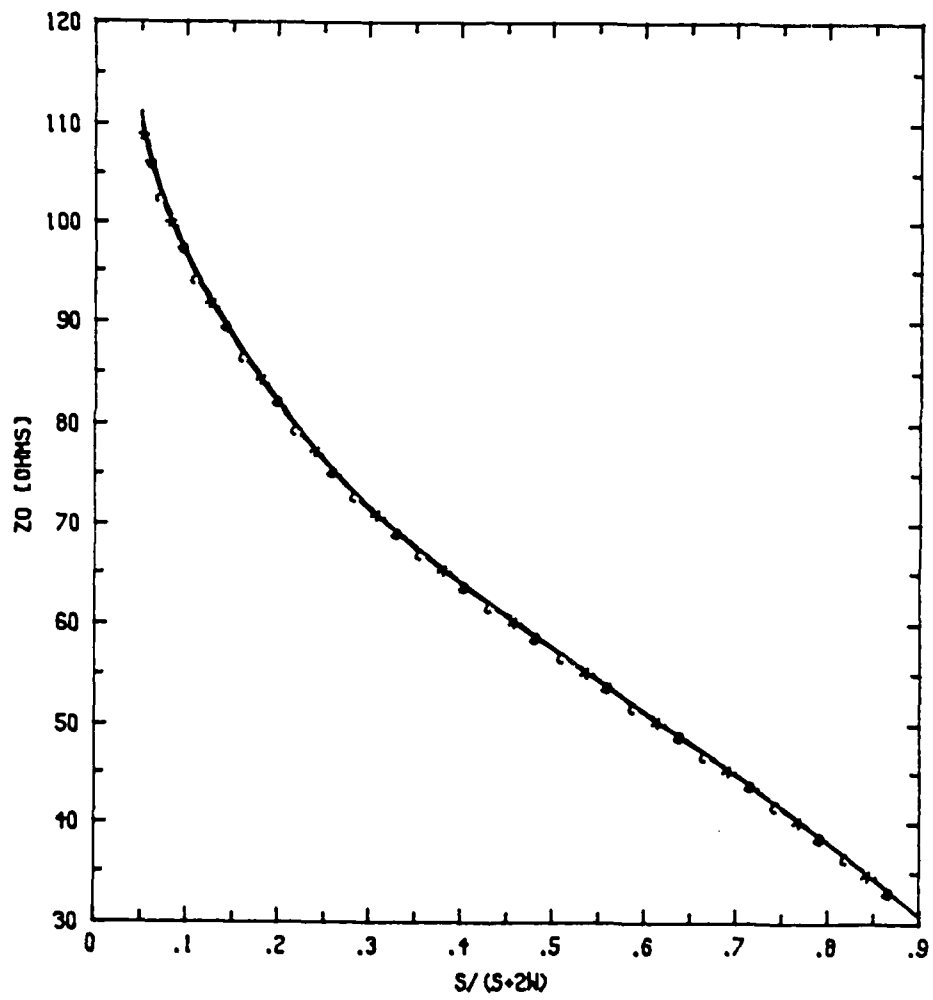


Fig.2.9(b) Characteristic impedance versus aspect ratio of Section B with different overlay thicknesses.

$s+2w=1.64\text{mm}$, $b=.001\text{mm}$, $\epsilon_r=12.9$ (S.I.GaAs), $\epsilon_r'=6.5$ (Si_3N_4), $f=10\text{GHz}$, Curve A--- $b=.001\text{mm}$, Curve B--- $b=.002\text{mm}$, Curve C--- $b=.005\text{mm}$.

hand, for a fixed $s+2w$ in CPW, both the propagation constant and the characteristic impedance decrease in Section A (more capacitive), while the propagation constant decreases firstly then increases and the characteristic impedance decreases in Section B (less inductive) as the center conductor width s increases. Since the slow-wave factor and the characteristic impedance in the periodic crosstie overlay slow-wave CPW mainly depend on $\sqrt{Z_B/Z_A}$ and $\sqrt{Z_A Z_B}$, respectively, by appropriately choosing the combination of center conductor width s and slot width w in CPW, one may optimally control both the slow-wave factor and the characteristic impedance values in the periodic crosstie overlay slow-wave CPW's.

Furthermore, from Figs.2.8(a)-2.9(b), both the propagation constant and the characteristic impedance decrease in Section A (more capacitive) whereas the propagation constant decreases and the characteristic impedance is almost unaffected (more inductive) in Section B as the dielectric overlay thickness b decreases. Consequently, a higher slow-wave factor can be realized by the adoption of a thinner dielectric overlay, as depicted in Fig.2.12 also.

2.5.3 EFFECT OF SUBSTRATE THICKNESS

As Figs.2.10(a), 2.10(b), 2.11(a) and 2.11(b) show, for a fixed distance between two ground planes $s+2w$ and an aspect ratio $s/(s+2w)$ in a CPW, the propagation constant increases and the characteristic impedance is almost unaffected in Section A (more capacitive), whereas the propagation constant increases and the characteristic impedance decreases in Section B (less inductive) as the substrate thickness h increases. Since the effect of substrate thickness on Section A is opposite that on Section B, the slow-wave factor and the characteristic impedance of the

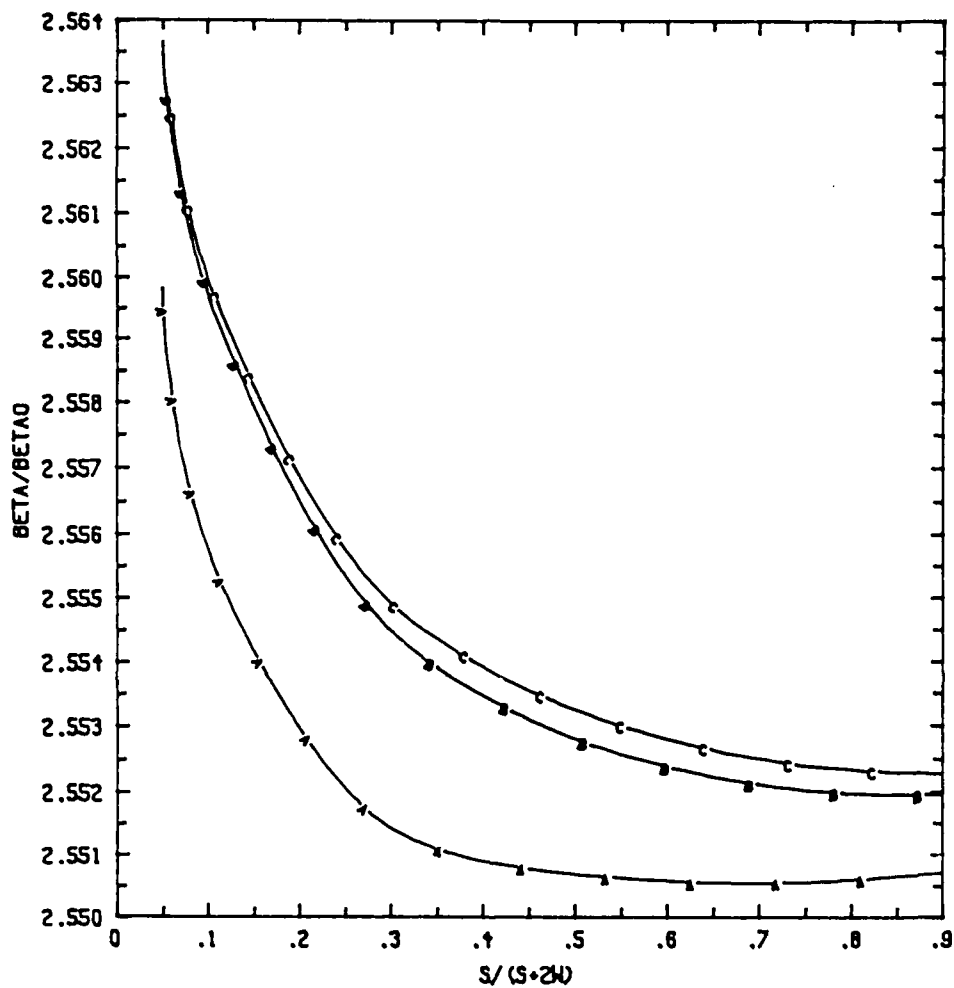


Fig.2.10(a) Normalized propagation constant versus aspect ratio of Section A
with different substrate thicknesses.

$s+2w=1.64\text{mm}$, $b=.001\text{mm}$, $\epsilon_r=12.9$ (S.I.GaAs), $\epsilon_r'=6.5(\text{Si}_3\text{N}_4)$,
 $f=10\text{GHz}$, Curve A---- $h=0.1\text{mm}$, Curve B---- $h=0.35\text{mm}$, Curve C----
 $h=0.5\text{mm}$.

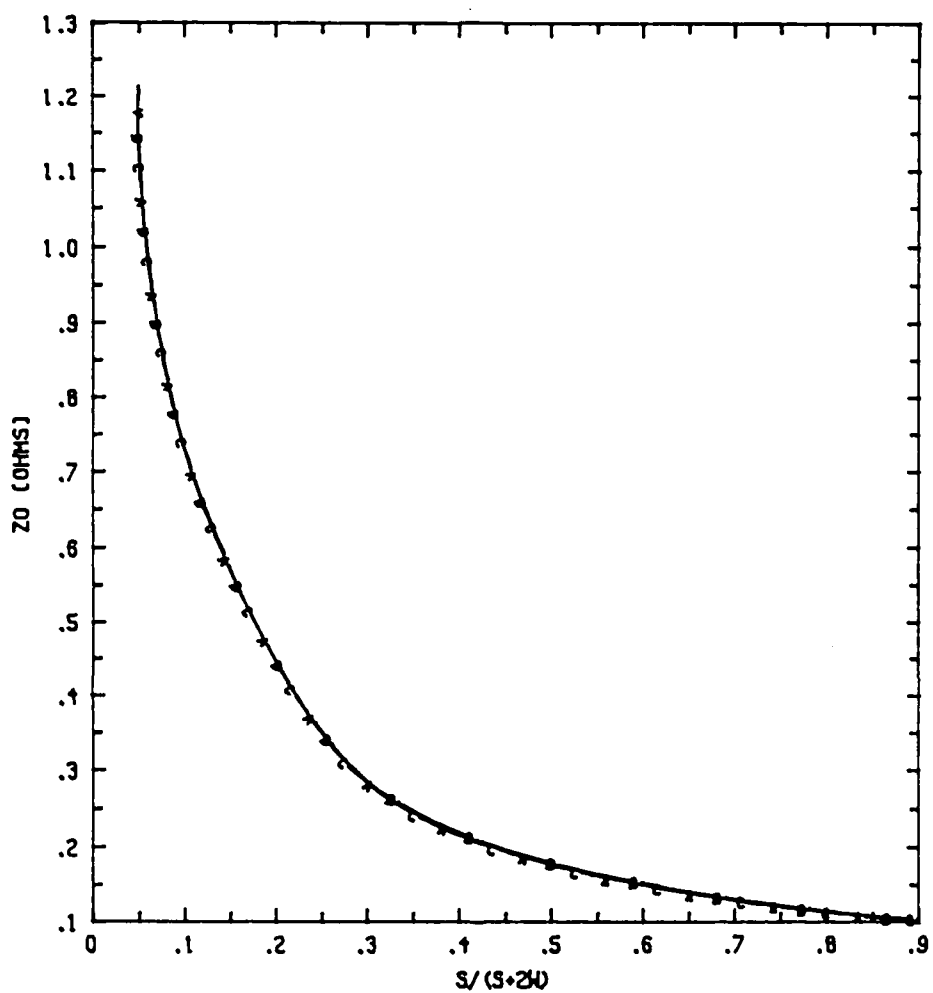


Fig.2.10(b) Characteristic impedance versus aspect ratio of Section A with different substrate thicknesses.

$s+2w=1.64\text{mm}$, $b=.001\text{mm}$, $\epsilon_r=12.9$ (S.I.GaAs), $\epsilon_r'=6.5(\text{Si}_3\text{N}_4)$, $f=10\text{GHz}$, Curve A---- $h=.1\text{mm}$, Curve B---- $h=.35\text{mm}$, Curve C---- $h=.5\text{mm}$.

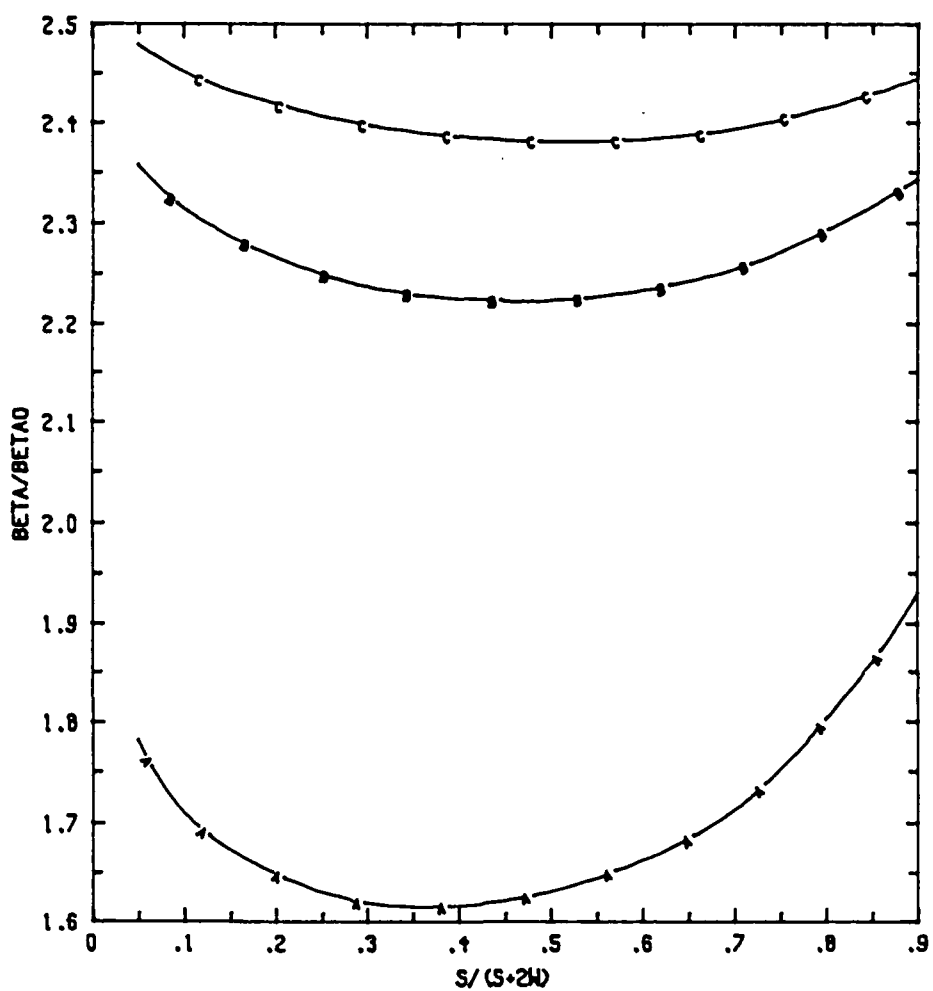


Fig.2.11(a) Normalized propagation constant versus aspect ratio of Section B
with different substrate thicknesses.

$s+2w=1.64\text{mm}$, $b=.001\text{mm}$, $\epsilon_r=12.9$ (S.I.GaAs), $\epsilon_r'=6.5(\text{Si}_3\text{N}_4)$,
 $f=10\text{GHz}$, Curve A--- $h=0.1\text{mm}$, Curve B--- $h=0.35\text{mm}$, Curve C---
 $h=0.5\text{mm}$.

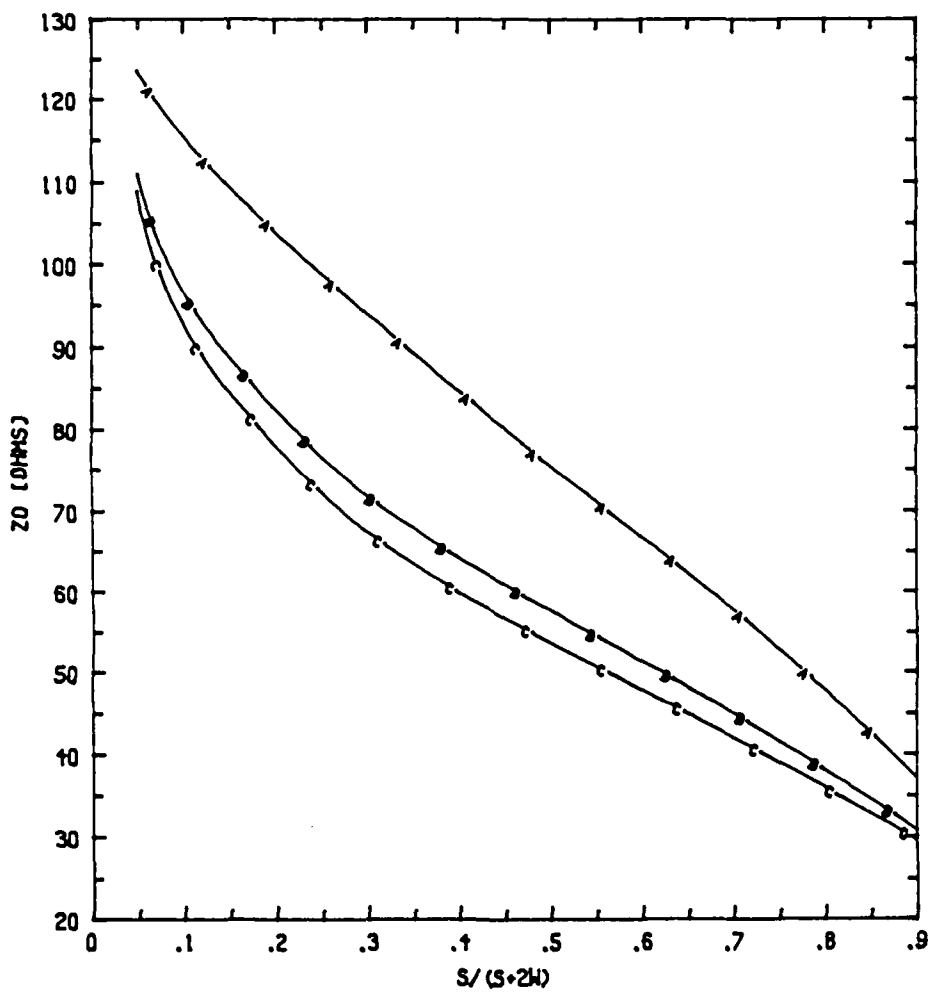


Fig.2.11(b) Characteristic impedance versus aspect ratio of Section B with different substrate thicknesses.

$s+2w=1.64\text{mm}$, $b=.001\text{mm}$, $\epsilon_r=12.9$ (S.I.GaAs), $\epsilon'_r=6.5(\text{Si}_3\text{N}_4)$, $f=10\text{GHz}$, Curve A--- $h=0.1\text{mm}$, Curve B--- $h=0.35\text{mm}$, Curve C--- $h=0.5\text{mm}$.

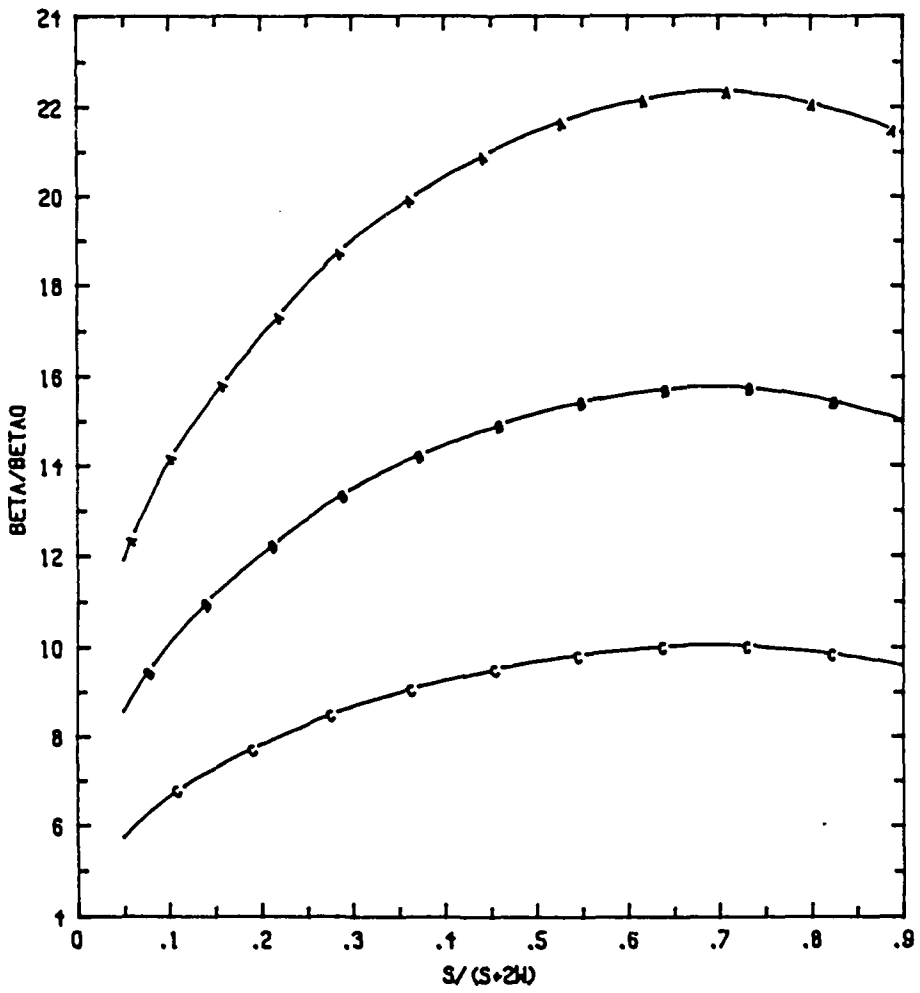


Fig.2.12 Slow-wave factor versus aspect ratio of crosstie overlay slow-wave CPWs with different overlay thicknesses.

Fig. $s+2w=1.64\text{mm}$, $b=.001\text{mm}$, $\epsilon_r=12.9$ (S.I.GaAs),
 $\epsilon_r'=6.5(\text{Si}_3\text{N}_4)$, $l_A=l_B=.01\text{mm}$, $f=10\text{GHz}$, Curve A---
 $b=.001\text{mm}$, Curve B--- $b=.002\text{mm}$, Curve C--- $b=.005\text{mm}$.

crosstie overlay slow-wave CPW would not change so much for the different thicknesses of substrates which have been used. The behavior is shown in Figs.2.13(a) and 2.13(b).

2.5.4 EFFECT OF THE LENGTHS OF THE CONSTITUENT SECTIONS

Figs.2.14(a) and 2.14(b) show the slow-wave factor and the characteristic impedance, respectively, of crosstie overlay slow-wave CPW's with different periodicities. As shown in Fig.2.14(a), it is noticed that, as the frequency is increased, the curve approaches a very dispersive region which is caused by the stopband phenomenon. The frequency at which such a region appears increases as the length of the grating period $l (=l_A + l_B)$ is reduced. Therefore, if the period chosen is much smaller than the operating wavelength, the corresponding frequency is in the linear portion of the curve much below the stopband so that the structure can be viewed as a uniform transmission line. In addition, it is easy to show from equation (2.43) that a maximum slow-wave factor and a maximum attenuation constant are achieved under the condition $\gamma_A l_A = \gamma_B l_B = \phi/2$ (ϕ is the phase shift amount in each period) in the linear dispersion region. In that region ($\gamma_A l_A \ll 1$, $\gamma_B l_B \ll 1$, $\gamma l \ll 1$) we can obtain the following approximations:

$$\cosh \gamma l = 1 + \frac{(\gamma l)^2}{2!} \quad (2.48a)$$

$$\sinh \gamma l \approx \gamma l \quad (2.48b)$$

Substituting (2.48a,b) into (2.43), we get

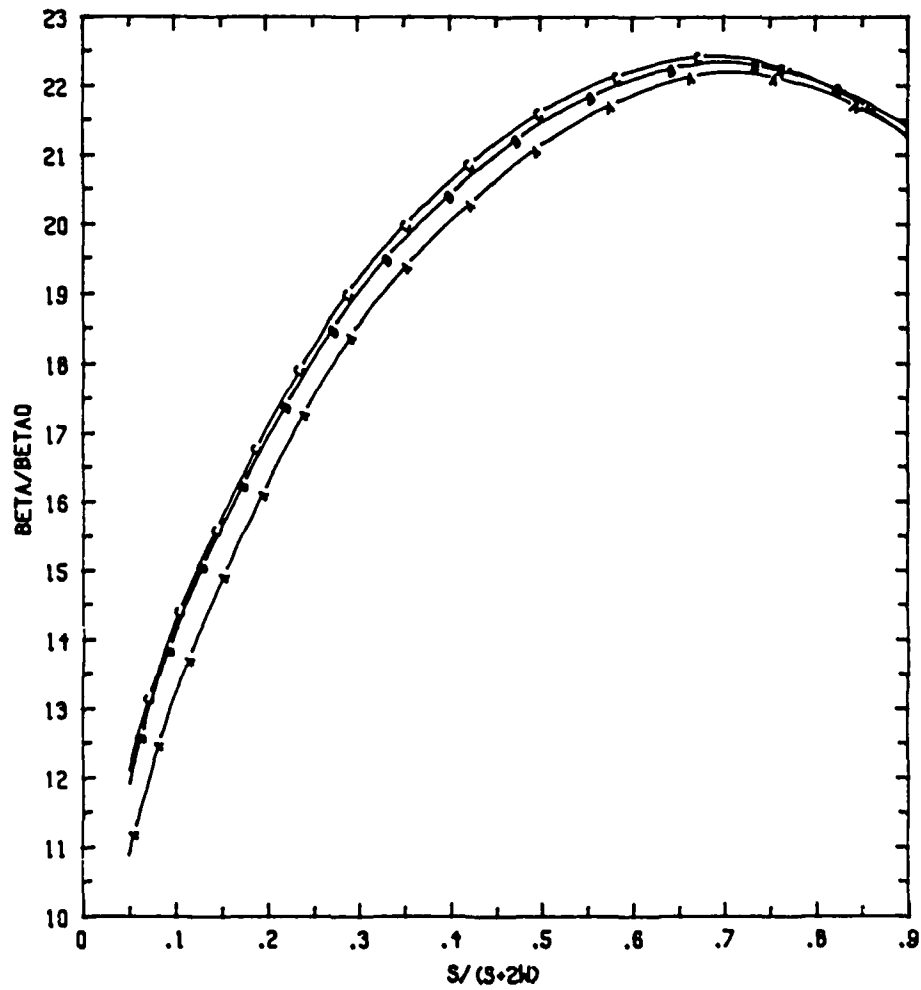


Fig.2.13(a) Slow-wave factor versus aspect ratio of crosstie overlay slow-wave CPWs with different substrate thicknesses.

$s+2w=1.64\text{mm}$, $b=.001\text{mm}$, $\epsilon_r=12.9$ (S.I.GaAs), $\epsilon_r'=6.5$ (Si₃N₄), $l_A=l_B=.01\text{mm}$, $f=10\text{GHz}$, Curve A--- $h=.1\text{mm}$, Curve B--- $h=.35\text{mm}$, Curve C--- $h=.5\text{mm}$.

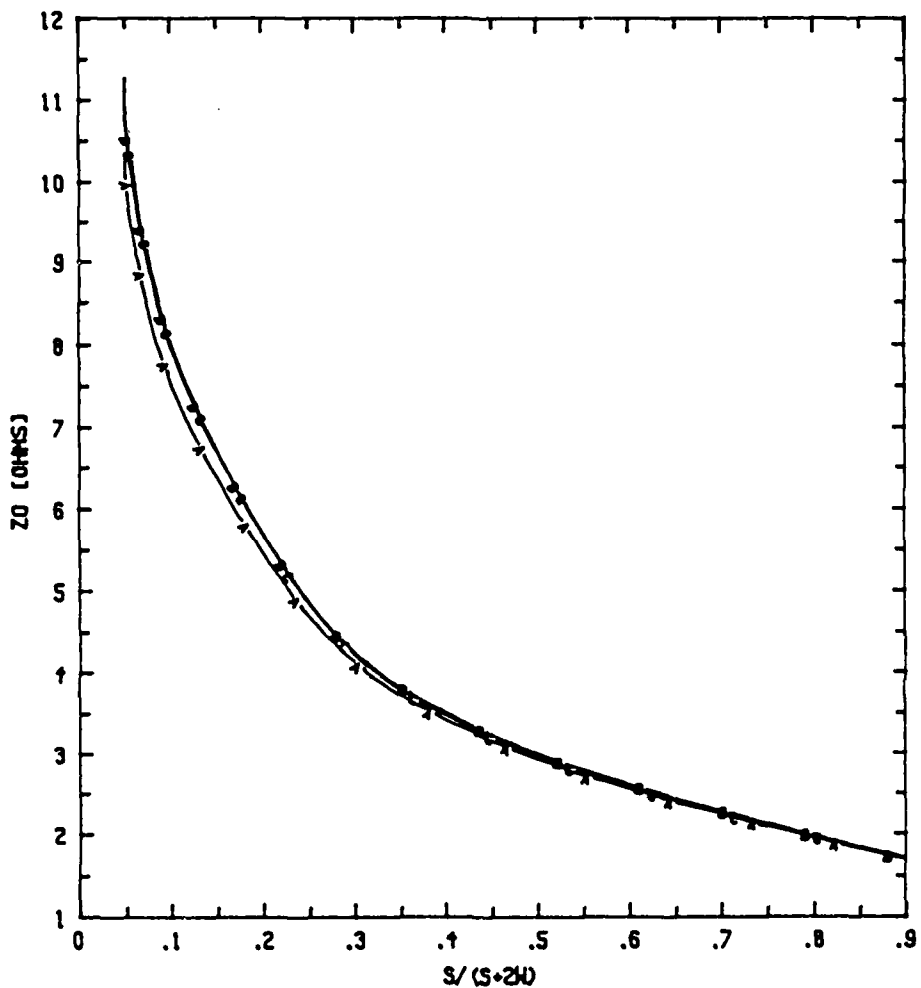


Fig.2.13(b) Characteristic impedance versus aspect ratio of crosstie overlay slow-wave CPWs with different substrate thicknesses.

$s+2w=1.64\text{mm}$, $b=.001\text{mm}$, $\epsilon_r=12.9$ (S.I.GaAs), $\epsilon_r'=6.5$ (Si_3N_4), $l_A=l_B=.01\text{mm}$, $f=10\text{GHz}$, Curve A--- $h=.1\text{mm}$, Curve B--- $h=.35\text{mm}$, Curve C--- $h=.5\text{mm}$.

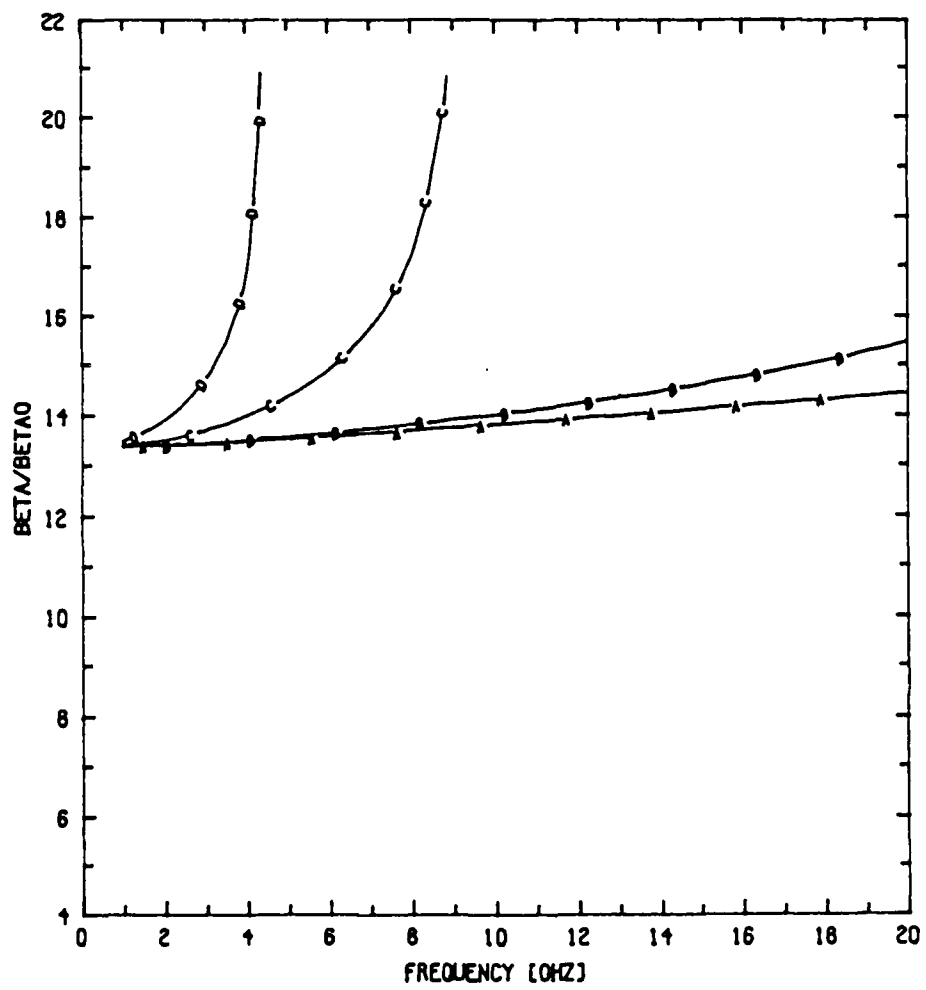


Fig.2.14(a) Slow-wave factor versus frequency of crosstie overlay slow-wave CPWs with different periodicities.

$s = .15 \text{ mm}$, $w = .745 \text{ mm}$, $b = .001 \text{ mm}$, $h = .35 \text{ mm}$, $\epsilon_r = 12.9$ (S.I.GaAs), $\epsilon_r' = 6.5(\text{Si}_3\text{N}_4)$, Curve A--- $l_A = l_B = 0.01 \text{ mm}$, Curve B--- $l_A = l_B = 0.1 \text{ mm}$, Curve C--- $l_A = l_B = 0.4 \text{ mm}$, Curve D--- $l_A = l_B = 0.8 \text{ mm}$.

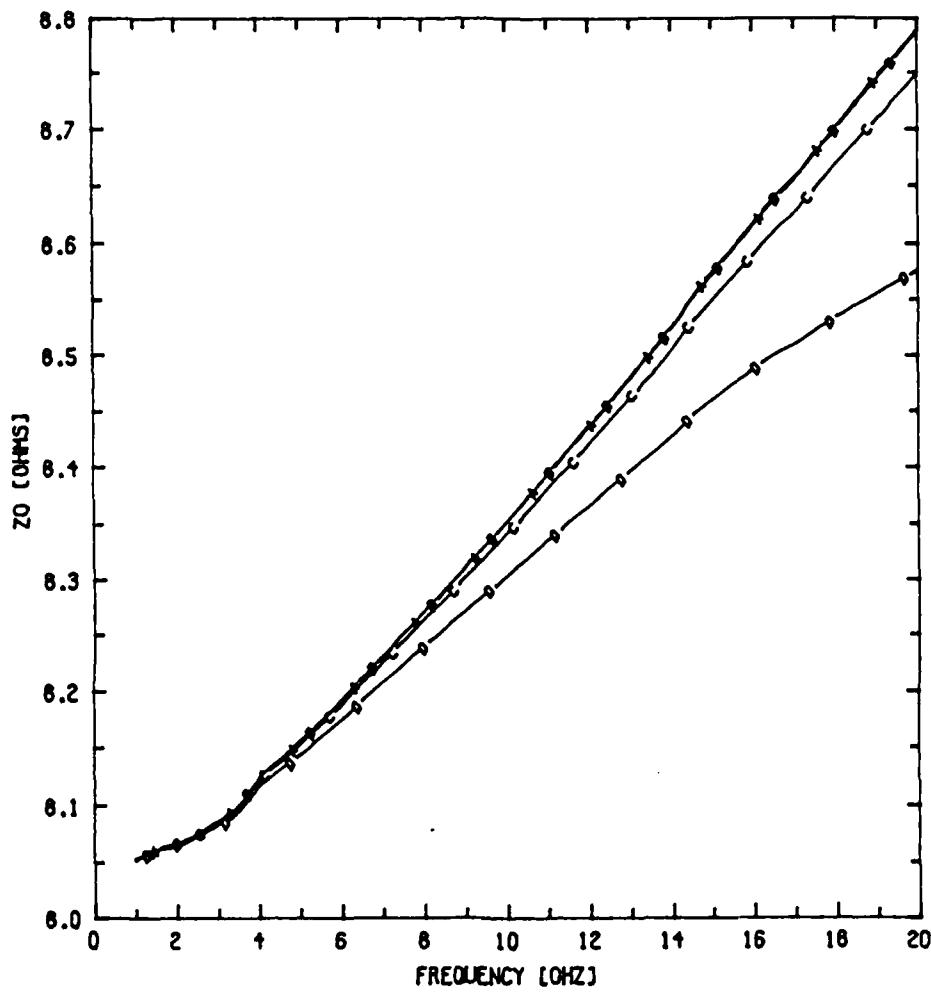


Fig.2.14(b) Characteristic impedance versus frequency of crosstie overlay slow-wave CPWs with different periodicities.

$s=.15\text{ mm}$, $w=.745\text{ mm}$, $b=.001\text{ mm}$, $h=.35\text{ mm}$, $\epsilon_r=12.9$ (S.I.GaAs), $\epsilon_r'=6.5(\text{Si}_3\text{N}_4)$, Curve A--- $l_A=l_B=.01\text{ mm}$, Curve B--- $l_A=l_B=.1\text{ mm}$, Curve C---- $l_A=l_B=.4\text{ mm}$, Curve D---- $l_A=l_B=.8\text{ mm}$.

$$\gamma = \frac{1}{(l_A + l_B)} \sqrt{\left(\gamma_A l_A - \gamma_B l_B\right)^2 + \left(\sqrt{\frac{Z_A}{Z_B}} + \sqrt{\frac{Z_B}{Z_A}}\right)^2 \gamma_A l_A \gamma_B l_B} \quad (2.49)$$

Hence, the maximum slow-wave factor and the maximum attenuation constant for a periodic crosstie overlay slow-wave CPW become

$$\left(\beta/\beta_0\right)_{\max} = \text{Real part of } \frac{\phi}{2\beta_0(l_A + l_B)} \left(\sqrt{\frac{Z_A}{Z_B}} + \sqrt{\frac{Z_B}{Z_A}} \right) \quad (2.50a)$$

$$(\alpha)_{\max} = \text{Imaginary part of } \frac{\phi}{2(l_A + l_B)} \left(\sqrt{\frac{Z_A}{Z_B}} + \sqrt{\frac{Z_B}{Z_A}} \right) \quad (2.50b)$$

where $\beta_0 = 2\pi/\lambda_0$, and the characteristic impedance is

$$Z_p = \sqrt{Z_A Z_B}. \quad (2.51)$$

Fig.2.15 shows how the slow-wave factor of the crosstie overlay slow-wave CPW depends on the duty cycle $l_A/(l_A + l_B)$. It is found that the maximum value of slow-wave factor occurs at the position where duty cycle is equal to 0.5 ($l_A = l_B$) as mentioned in above.

2.6 CONDUCTOR LOSS ESTIMATION

The discussion of the periodic crosstie overlay slow-wave CPW thus far has been based on the assumption that the losses are negligible. However, in practice, losses are always present and it may be quite important to obtain a quantitative estimate of these losses in order to reliably design the slow-wave circuits. It will therefore be pertinent to include here brief descriptions of the methods that we use for evaluating these losses. For simplicity, due to the very nice insulating properties of

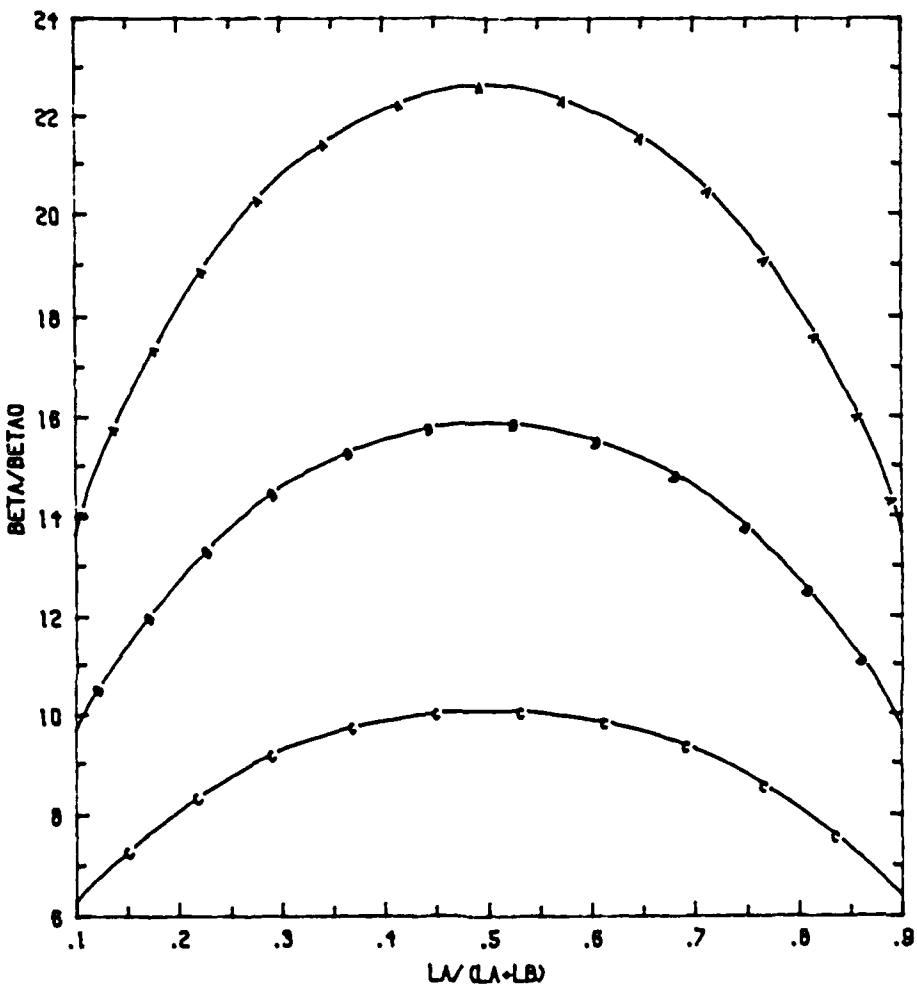


Fig.2.15 Slow-wave factor versus duty cycle of crosstie overlay slow-wave CPWs with different overlay thicknesses.

$s=.15\text{mm}$, $w=.745\text{mm}$, $b=.001\text{mm}$, $h=.35\text{mm}$, $\epsilon_r=12.9$
 (S.I.GaAs), $\epsilon_r'=6.5(\text{Si}_3\text{N}_4)$, $l_A+l_B=.1\text{mm}$, $f=10\text{GHz}$, Curve A---
 $-b=.001\text{mm}$, Curve B---- $b=.002\text{mm}$, Curve C---- $b=.005\text{mm}$.

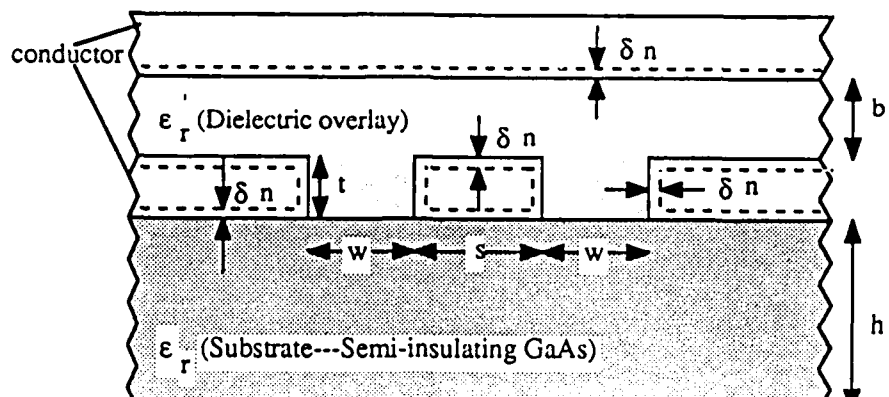
the semi-insulating GaAs substrate and dielectric overlay used as well as the good nature of the propagating mode, we restrict our attention to the ohmic skin loss only and assume that the dielectric, magnetic, and radiation losses in the new crosstie slow-wave structure are either absent or negligible.

Referring to Fig.2.16 in Section A, the ohmic loss per unit length includes the CPW and the crosstie strip ohmic losses while only CPW ohmic loss exists in Section B. To obtain the ohmic attenuation constant α_c for the constituent sections A and B, a technique based on the so-called "incremental inductance rule" which is due to Wheeler [27] has been used. This rule expresses the series surface resistance R_s per unit length in terms of that part of the total inductance per unit length which is attributable to the skin effect, i.e., the inductance L_i produced by the magnetic field within the conductors.

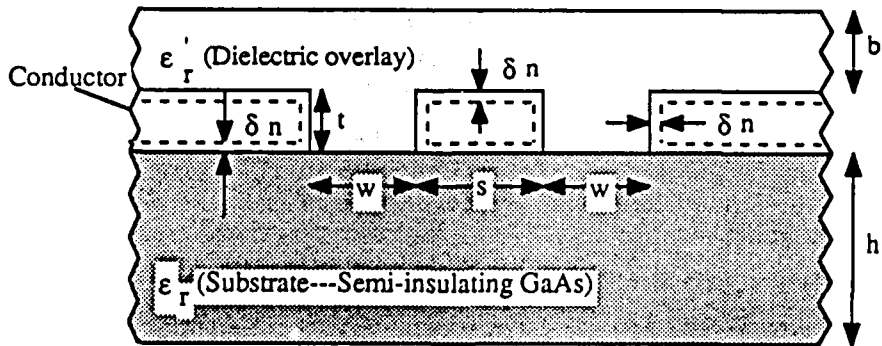
It is well known that for a conductor the surface impedance $Z_s (=R_s+jX_s)$ has a real part R_s (surface resistance per unit length) which is equal to the imaginary part X_s . That is

$$R_s = X_s = \omega L_i \quad (2.52)$$

According to Wheeler, L_i can be inferred from the external inductance L per unit length as the incremental increase in L caused by an incremental recession of all metallic walls carrying a skin current (see Fig.2.16). The amount of recession is equal to half the skin depth $\delta = \sqrt{2/\omega\mu\sigma_c}$, where μ and σ_c are the permeability and the conductivity, respectively, of the metallic wall material. An assumption underlying this rule is that the radius of curvature and the thickness of the conductors exposed to

Section A

(a)

Section B

(b)

Fig.2.16 Recession of conducting walls of crosstie overlay coplanar waveguide
 (a) Section A, (b) Section B using "Incremental Inductance Rule".

the electromagnetic fields be greater than the skin depth, preferably several skin depths. According to Wheeler, we have

$$L_i = \sum_m \left(\frac{\mu_m}{\mu_0} \right) \left(\frac{\partial L}{\partial n_m} \right) \left(\frac{\delta_m}{2} \right) \quad (2.53)$$

$$R_s = \sum_m \left(\frac{R_{sm}}{\mu_0} \right) \left(\frac{\partial L}{\partial n_m} \right) \quad (2.54)$$

where $\partial L / \partial n_m$ denotes the derivative of L with respect to incremental recession of wall m , n_m is the normal direction to this wall, and $R_{sm} = \omega \mu_m \delta_m / 2$ is the surface resistivity of the wall m .

The attenuation constant because of ohmic loss is defined as

$$\alpha_c \approx \frac{P_c}{2P} = \frac{\text{power loss in conductors}}{2 \times \text{power transmitted}} \quad (\text{nepers/unit length}) \quad (2.55)$$

In terms of R_s and Z_c , α_c may be written as

$$\alpha_c = \frac{|I|^2 R_s}{2|I|^2 Z_c} = \frac{1}{2\mu_0 Z_c} \sum_m R_{sm} \frac{\partial L}{\partial n_m} \quad (2.56)$$

where Z_c is the characteristic impedance of the constituent section A or B calculated under the quasi-TEM approximation for the lossless case, and I is the total current per conductor.

We assume that the inductance per unit length for the inhomogeneous dielectric case (Section A or B) is approximately the same as that of the unloaded TEM line. This assumption implies that the stored magnetic energy is not affected by the presence of the nonmagnetic dielectric substrate. This is a reasonable assumption

as verified experimentally by Pucel et al. [28]. With this assumption in mind, the inductance per unit length can be expressed in terms of the characteristic impedance for the Section A or B with the dielectric materials replaced by air (Z_c^a) and is given as

$$L = \frac{Z_c^a}{c} \quad (2.57)$$

where $c (=1/\sqrt{\mu_0\epsilon_0})$ is the velocity of electromagnetic waves in free space. From equations (2.56) and (2.57) one obtains

$$\alpha_c = \left(\frac{\epsilon_0}{\mu_0} \right)^{1/2} \frac{1}{2Z_c} \sum_m R_{sm} \frac{\partial Z_c^a}{\partial n_m}. \quad (2.58)$$

Equation (2.58) is the basis for our skin loss computations. Referring to Fig.2.16 in Section A, Z_c^a is a function of b , s , w , and t , respectively. In Section B, Z_c^a is a function of s , w , and t . By considering to first order the variation in Z_c^a that occurs due to an inward normal perturbation δn at each surface there results:

Section A :

$$\delta b = \delta w = +2\delta n \quad (2.59a)$$

$$\delta s = \delta t = -2\delta n. \quad (2.59b)$$

Section B:

$$\delta w = +2\delta n \quad (2.60a)$$

$$\delta s = \delta t = -2\delta n. \quad (2.60b)$$

The variation in Z_c^a is

Section A:

$$\delta Z_c^a = \frac{\partial Z_c^a}{\partial b} \delta b + \frac{\partial Z_c^a}{\partial s} \delta s + \frac{\partial Z_c^a}{\partial w} \delta w + \frac{\partial Z_c^a}{\partial t} \delta t; \quad (2.61a)$$

Section B:

$$\delta Z_c^a = \frac{\partial Z_c^a}{\partial s} \delta s + \frac{\partial Z_c^a}{\partial w} \delta w + \frac{\partial Z_c^a}{\partial t} \delta t. \quad (2.61b)$$

Substituting (2.59), (2.60) and (2.61) into (2.58), then the ohmic attenuation constant α_c for the constituent sections A and B can be written as

Section A:

$$\alpha_c = \sqrt{\frac{\epsilon_0}{\mu_0} \frac{R_s}{Z_c} \left[\frac{\partial Z_c^a}{\partial b} - \frac{\partial Z_c^a}{\partial s} + \left(1 - \frac{\partial w}{\partial t}\right) \frac{\partial Z_c^a}{\partial w} \right]}; \quad (2.62a)$$

Section B:

$$\alpha_c = \sqrt{\frac{\epsilon_0}{\mu_0} \frac{R_s}{Z_c} \left[\left(1 - \frac{\partial w}{\partial t}\right) \frac{\partial Z_c^a}{\partial w} - \frac{\partial Z_c^a}{\partial s} \right]} \quad (2.62b)$$

for the case $R_{s1}=R_{s2}=R_s$ (R_{s1} and R_{s2} are the surface resistivities of the crosstie strip and CPW conductors, respectively).

The remaining task is to derive the expression for the characteristic impedance Z_c^a of the lossless line. From the quasi-static results by Ghione and Naldi [29], we get

Section A:

$$Z_c^a = Z_c \Big|_{\epsilon_r = \epsilon_r' = 1} = \frac{60\pi}{\sqrt{\epsilon_{\text{eff}} \left[\frac{K(k)}{K(k)} + \frac{K(k_2)}{K(k_2)} \right]}} \Big|_{\epsilon_r = \epsilon_r' = 1} = \frac{60\pi}{\frac{K(k)}{K(k)} + \frac{K(k_2)}{K(k_2)}} \quad (2.63a)$$

where

$$\epsilon_{\text{eff}} = \frac{\frac{K(k)}{K(k)} + (\epsilon_r - 1) \frac{K(k_1)}{K(k_1)} + \epsilon_r \frac{K(k_2)}{K(k_2)}}{\frac{K(k)}{K(k)} + \frac{K(k_2)}{K(k_2)}} \quad (2.63b)$$

$$k = \frac{s}{s+2w}$$

$$k_1 = \frac{\sinh\left(\frac{\pi s}{4h}\right)}{\sinh\left(\frac{\pi(s+2w)}{4h}\right)}$$

$$k_2 = \frac{\tanh\left(\frac{\pi s}{4b}\right)}{\tanh\left(\frac{\pi(s+2w)}{4b}\right)}$$

$$k' = \sqrt{1-k^2}$$

$$k_1' = \sqrt{1-k_1^2}$$

$$k_2' = \sqrt{1-k_2^2}$$

$K(k)$ is the complete elliptic integral of the first kind and

$$\frac{K(k)}{K(k)} = \frac{K(k)}{K(k)} = \frac{1}{\pi} \ln \left[2 \frac{1+\sqrt{k}}{1-\sqrt{k}} \right] \quad 0.707 \leq k \leq 1$$

$$\frac{K(k)}{K(k)} = \frac{K(k)}{K(k)} = \frac{\pi}{\ln \left[2 \frac{1+\sqrt{k}}{1-\sqrt{k}} \right]} \quad 0 \leq k \leq 0.707$$

Section B:

$$Z_c^a = Z_c \left| \frac{30\pi}{\sqrt{\epsilon_{eff}} \frac{1}{K(k)}} \right| = \frac{30\pi}{\frac{1}{K(k)}} \quad (2.64a)$$

where

$$\epsilon_{eff} = \frac{2 \frac{K(k)}{K(k)} + (\epsilon_r - 1) \frac{K(k_1)}{K(k_1)} + (\epsilon_r - 1) \frac{K(k_3)}{K(k_3)}}{2 \frac{K(k)}{K(k)}} \quad (2.64b)$$

$$k_3 = \frac{\sinh(\frac{\pi s}{4b})}{\sinh\left[\frac{\pi(s+2w)}{4b}\right]}$$

The expression for Δw , the effective decrease in the slot width of a CPW due to strip thickness, is given approximately in [30], and is repeated below:

$$\Delta w = - (w_e - w) = - \frac{1.25t}{\pi} \left(1 + \ln \frac{4\pi s}{t} \right). \quad (2.65)$$

The partial derivative $\partial w / \partial t$ is obtained from (2.65) as

$$\frac{\partial w}{\partial t} = \frac{1.25}{\pi} \ln\left(\frac{4\pi s}{t}\right). \quad (2.66)$$

Utilizing (2.62) and (2.66), we finally obtain the attenuation constant α_c of the constituent sections A and B due to skin ohmic loss after a lengthy but straightforward mathematical manipulation.

2.7 PROPAGATION CHARACTERISTICS OF A CROSSTIE OVERLAY SLOW-WAVE COPLANAR WAVEGUIDE WITH LOSSY CONDUCTORS

Figures 2.17(a) and 2.17(b) show the calculated ohmic attenuation constant versus aspect ratio $s/(s+2w)$ of a CPW in Section A with 1.5 μm - and 3 μm -thick gold as the conductor, respectively. Figs.2.18(a) and 2.18(b) show the calculated ohmic attenuation constant versus aspect ratio $s/(s+2w)$ of a CPW in Section B with 1.5 μm - and 3 μm -thick gold as the conductor, respectively. Comparing to Section B, due to the existence of crosstie strip and thin dielectric overlay, the surface skin current density as well as ohmic loss in Section A are not only greatly enhanced but also more insensitive with respect to the aspect ratio $s/(s+2w)$. For a fixed value of $s+2w$ in CPW, as the center conductor width s decreases, the current flowing on the center conductor is more concentrated and the series resistance increases. On the other hand, if the slot width w decreases so that $s/(s+2w)$ increases, the current is concentrated on the conductor surface bordering the gap and the series resistance increases. Hence the series resistance takes a minimum value for a certain finite value of $s/(s+2w)$. In addition, as the conductor thickness increases, series resistance and ohmic loss reduce. This is natural because as the conductor thickness increases the

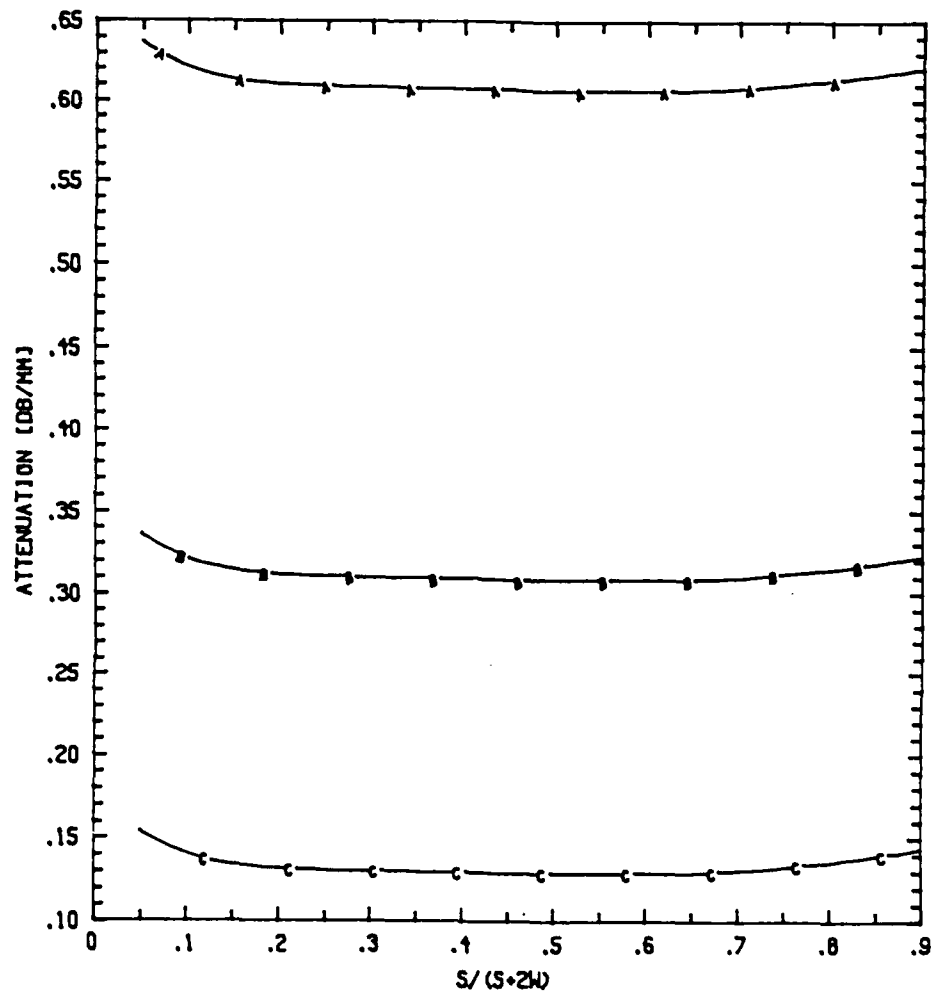


Fig.2.17(a) Ohmic attenuation constant versus aspect ratio of Section A with different overlay thicknesses ($\text{Au}=1.5\mu\text{m}$).

$s+2w=1.64\text{mm}$, $b=.001\text{mm}$, $h=.35\text{mm}$, $\epsilon_r=12.9$ (S.I.GaAs),
 $\epsilon'_r=6.5(\text{Si}_3\text{N}_4)$, $\text{Au}=1.5\mu\text{m}$, $f=10\text{GHz}$, Curve A---- $b=.001\text{mm}$,
Curve B---- $b=.002\text{mm}$, Curve C---- $b=.005\text{mm}$.

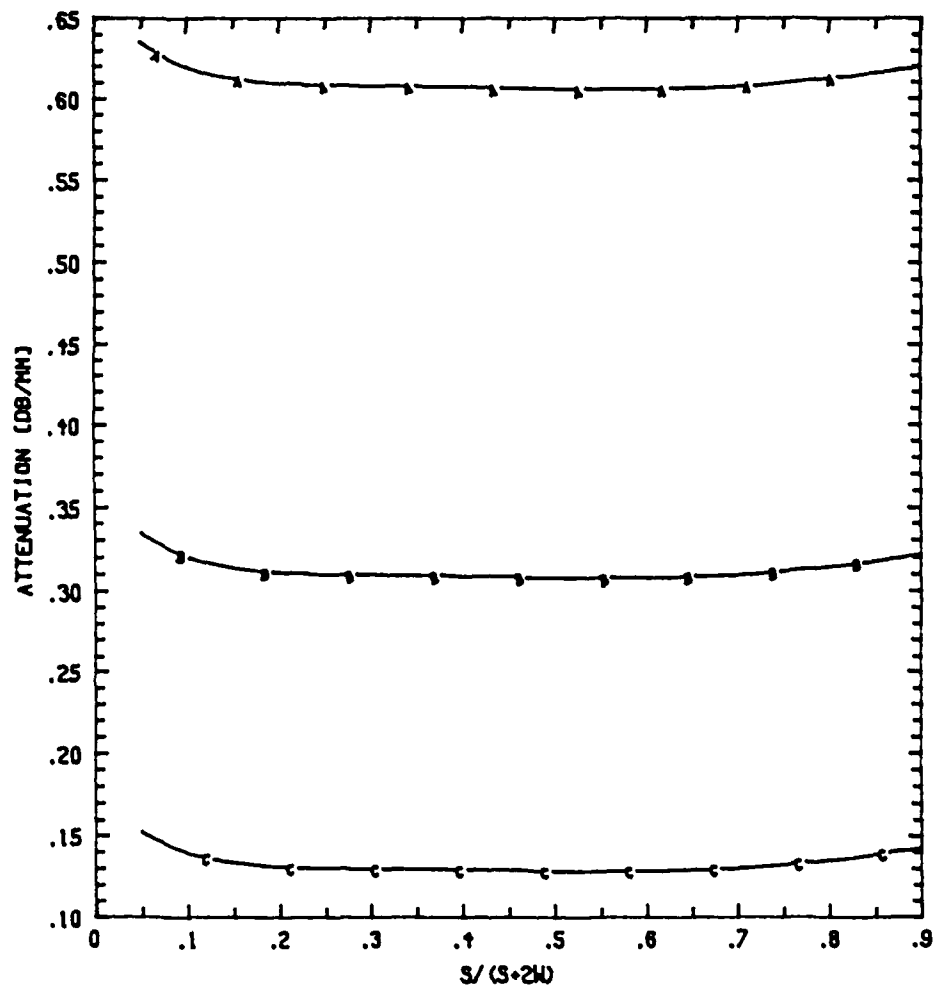


Fig.2.17(b) Ohmic attenuation constant versus aspect ratio of Section A with different overlay thicknesses (Au=3.0μm).

$s+2w=1.64\text{mm}$, $b=.001\text{mm}$, $h=.35\text{mm}$, $\epsilon_r=12.9$ (S.I.GaAs),
 $\epsilon_r'=6.5(\text{Si}_3\text{N}_4)$, Au=3.0μm, f=10GHz, Curve A---b=.001mm,
Curve B---b=.002mm, Curve C---b=.005mm.

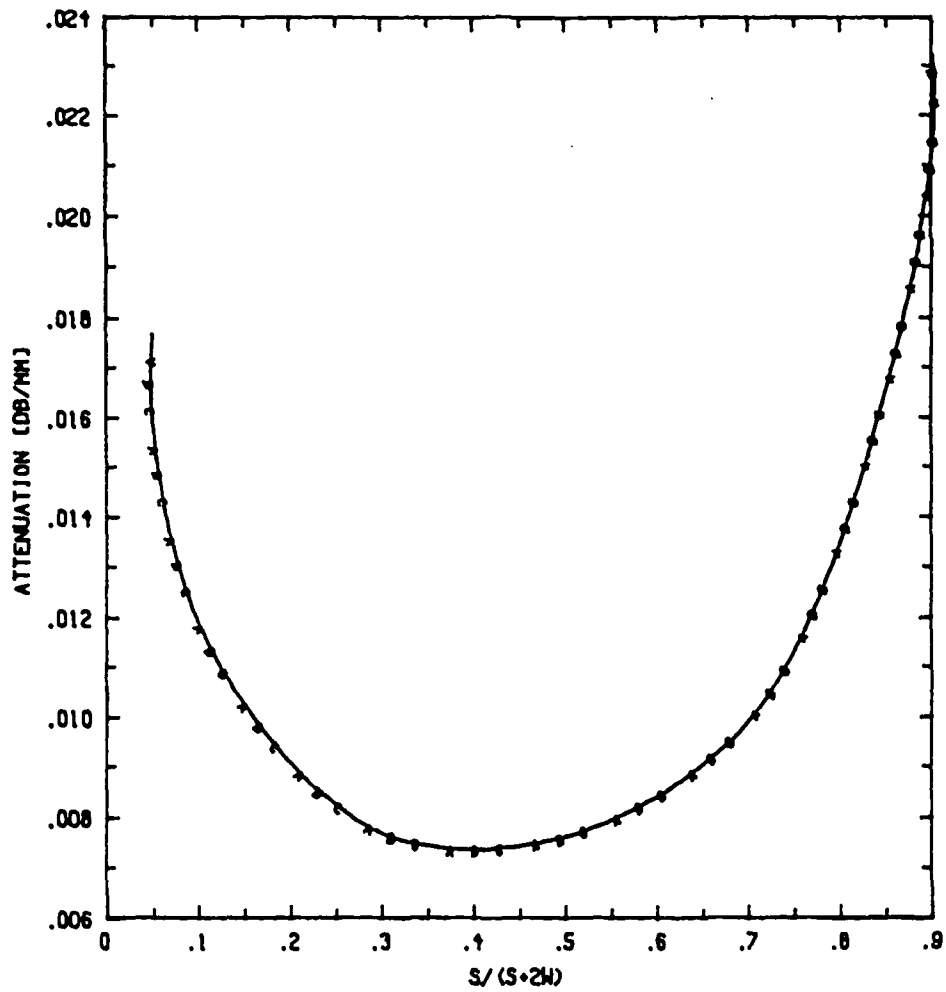


Fig.2.18(a) Ohmic attenuation constant versus aspect ratio of Section B with different overlay thicknesses ($Au=1.5\mu m$).

$s+2w=1.64mm$, $b=.001mm$, $h=.35mm$, $\epsilon_r=12.9$ (S.I.GaAs),
 $\epsilon_r'=6.5(Si_3N_4)$, $Au=1.5\mu m$, $f=10GHz$, Curve A--- $b=.001mm$,
Curve B--- $b=.002mm$, Curve C--- $b=.005mm$.

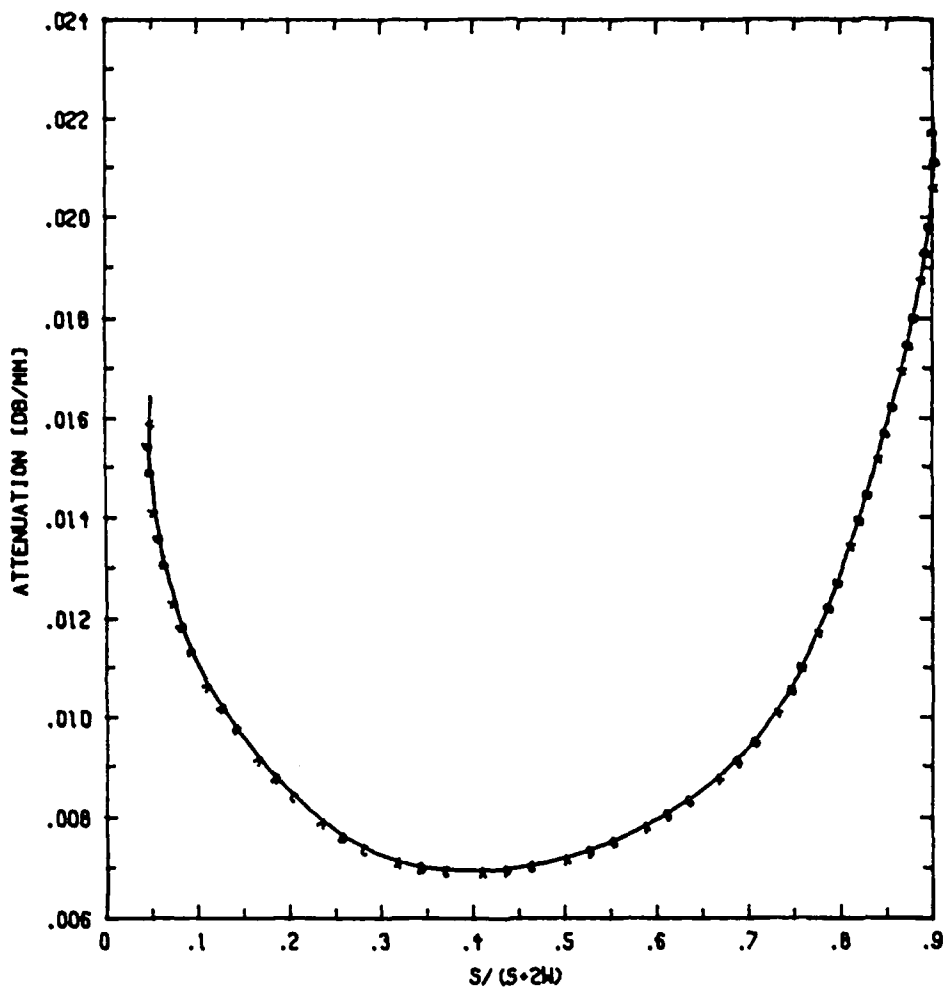


Fig.2.18(b) Ohmic attenuation constant versus aspect ratio of Section B with different overlay thicknesses (Au=3.0μm).

$s+2w=1.64\text{mm}$, $b=.001\text{mm}$, $h=.35\text{mm}$, $\epsilon_r=12.9$ (S.I.GaAs),
 $\epsilon_r'=6.5(\text{Si}_3\text{N}_4)$, Au=3.0μm, f=10GHz, Curve A----b=.001mm,
Curve B----b=.002mm, Curve C----b=.005mm.

cross-sectional size of the center conductor and metal crosstie increase. In Section A, the series resistance is larger for the structure with a thinner dielectric overlay than for the one with a thicker dielectric overlay. This is because the current is shifted more toward the conductor surface in contact with the thinner dielectric overlay. Fig.2.19 shows the attenuation constant (α) due to conductor loss of the crosstie overlay slow-wave CPW with different dielectric overlay thicknesses. In this figure, we have assumed that the attenuation constants due to dielectric loss in both Sections A and B were negligibly small. Based on the theory given in Section 2.6, the attenuation constants due to CPW and crosstie conductor losses in Section A (α_A) and due to CPW conductor loss only in Section B (α_B) were calculated. In the meantime, we assumed that the propagation constants in Section A (β_A) and Section B (β_B) were not affected by the attenuation due to conductor loss. By applying (2.43), we finally obtained the attenuation constant per unit length of the infinitely long crosstie overlay slow-wave CPW's.

Figure 2.20 shows the quality factor ($Q=\beta/2\alpha$) of the crosstie overlay slow-wave CPW versus aspect ratio $s/(s+2w)$ with different overlay thicknesses. It is found that a better quality factor could be obtained with appropriate choice of s and w as well as thicker dielectric overlay. Fig.2.21 shows the ohmic attenuation constant of the crosstie overlay slow-wave CPW versus duty cycle factor $I_A/(I_A+I_B)$. Due to the reason discussed in Section 2.5.4, when $I_A/(I_A+I_B)=0.5$ ($I_A=I_B$) the slow-wave CPW exhibits the maximum ohmic attenuation. Fig.2.22 represents the relationship between Q value and duty cycle factor $I_A/(I_A+I_B)$. Because of the large ohmic loss in Section A, the shorter the I_A , the higher the Q value.

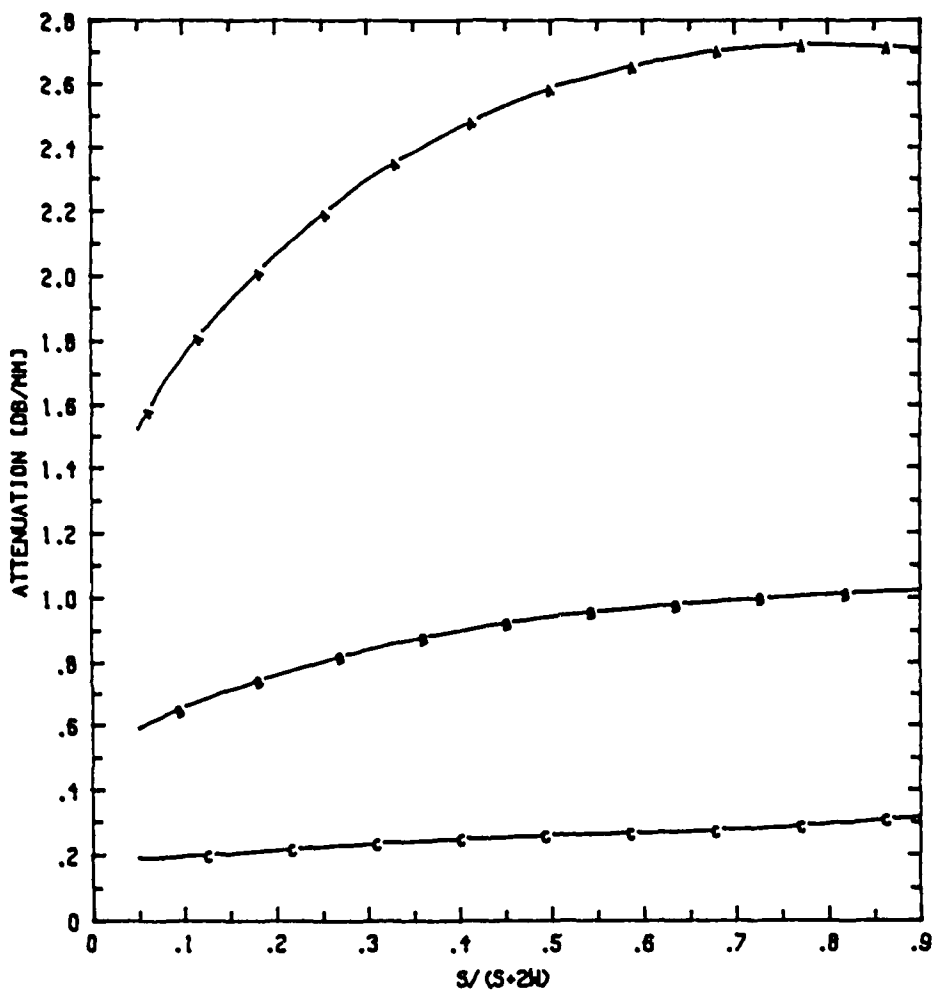


Fig.2.19 Ohmic attenuation constant of crosstie overlay slow-wave CPW with different overlay thicknesses.

$s+2w=1.64\text{mm}$, $b=.001\text{mm}$, $h=.35\text{mm}$, $\epsilon_r=12.9$ (S.I.GaAs),
 $\epsilon_r'=6.5(\text{Si}_3\text{N}_4)$, $\text{Au}=1.5\mu\text{m}$, $l_A=l_B=.01\text{mm}$, $f=10\text{GHz}$, Curve A--- $b=.001\text{mm}$, Curve B---- $b=.002\text{mm}$, Curve C--- $b=.005\text{mm}$.

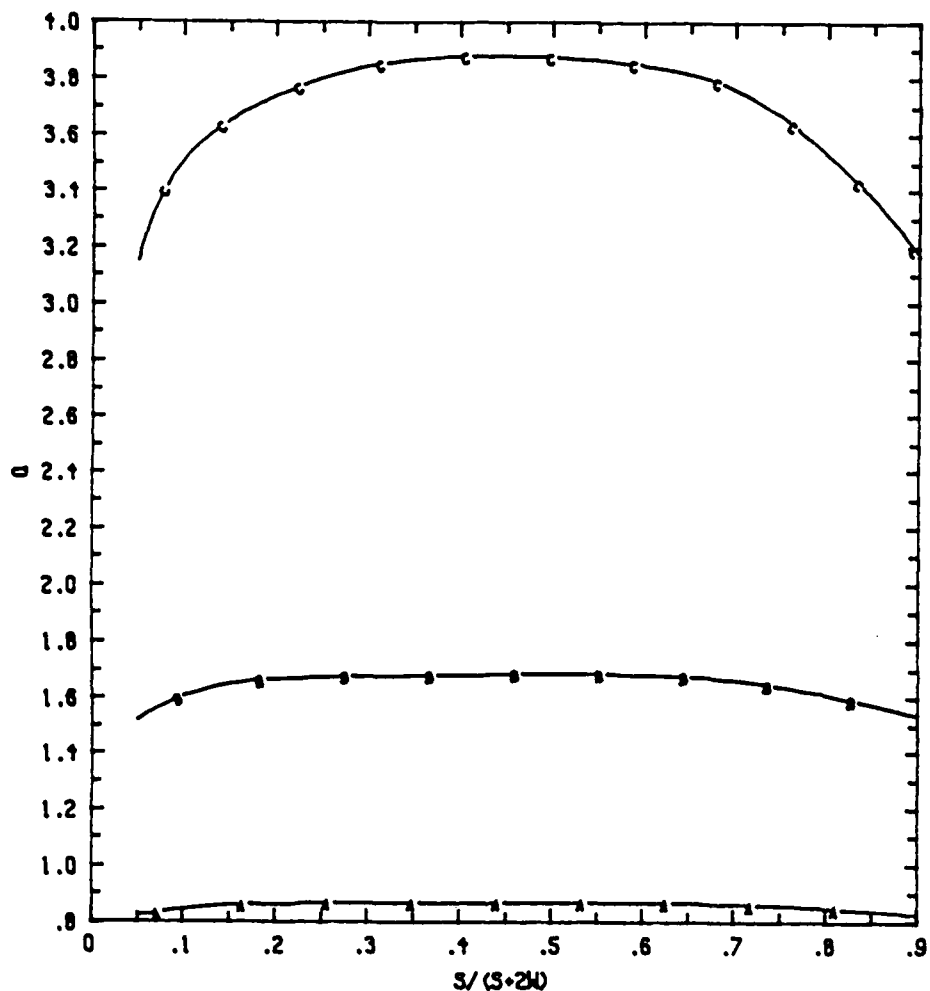


Fig.2.20 Quality factor versus aspect ratio of crosstie overlay slow-wave CPWs with different overlay thicknesses.

$s+2w=1.64\text{mm}$, $b=.001\text{mm}$, $h=.35\text{mm}$, $\epsilon_r=12.9$ (S.I.GaAs),
 $\epsilon_r'=6.5(\text{Si}_3\text{N}_4)$, $\text{Au}=1.5\mu\text{m}$, $l_A=l_B=0.01\text{mm}$, $f=10\text{GHz}$, Curve A--- $b=.001\text{mm}$, Curve B---- $b=.002\text{mm}$, Curve C--- $b=.005\text{mm}$.

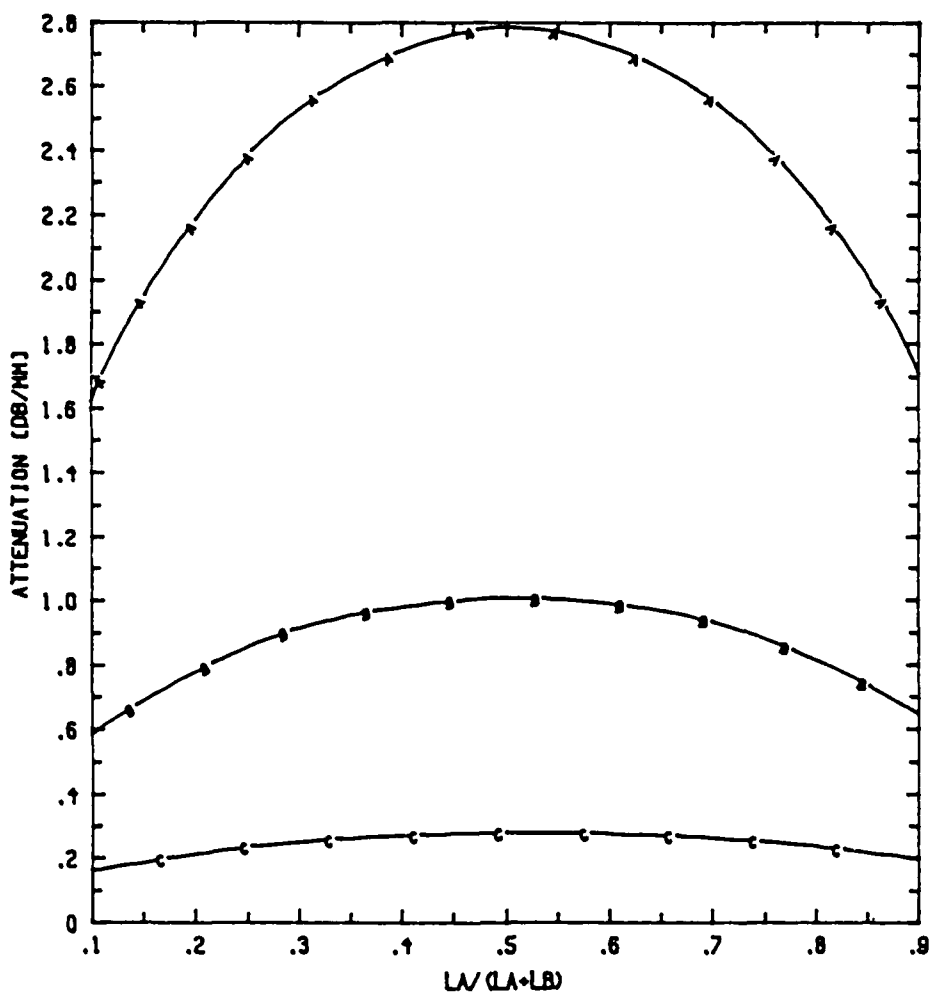


Fig.2.21 Ohmic attenuation constant versus duty cycle of crosstie overlay slow-wave CPWs with different overlay thicknesses.

$s = .15\text{ mm}$, $w = .745\text{ mm}$, $b = .001\text{ mm}$, $h = .35\text{ mm}$, $\epsilon_r = 12.9$ (S.I.GaAs), $\epsilon'_r = 6.5$ (Si_3N_4), $\text{Au} = 1.5\mu\text{m}$, $l_A + l_B = .1\text{ mm}$, $f = 10\text{ GHz}$, Curve A--- $b = .001\text{ mm}$, Curve B--- $b = .002\text{ mm}$, Curve C--- $b = .005\text{ mm}$.

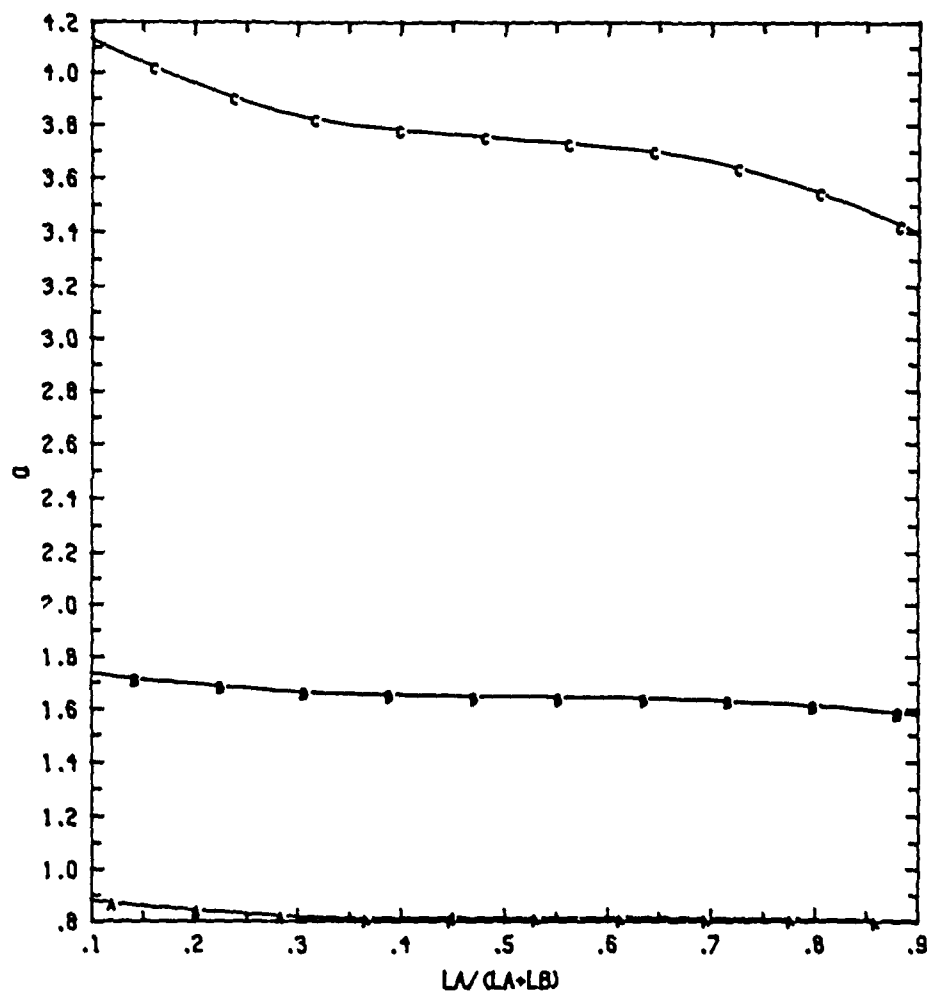


Fig.2.22 Quality factor versus duty cycle of crosstie overlay slow-wave CPWs with different overlay thicknesses.

$s=.15\text{mm}$, $w=.745\text{mm}$, $b=.001\text{mm}$, $h=.35\text{mm}$, $\epsilon_r=12.9$
 (S.I.GaAs), $\epsilon_r'=6.5(\text{Si}_3\text{N}_4)$, $\text{Au}=1.5\mu\text{m}$, $l_A+l_B=1\text{mm}$, $f=10\text{GHz}$,
 Curve A--- $b=.001\text{mm}$, Curve B--- $b=.002\text{mm}$, Curve C--- $b=.005\text{mm}$.

AD-A194 981

CONFIRMATION OF SLOW-WAVES IN A CROSSTIE OVERLAY
COPLANAR WAVEGUIDE AND I. (U) TEXAS UUVY AT AUSTIN DEPT
OF ELECTRICAL AND COMPUTER ENGINEER. T WANG ET ALL

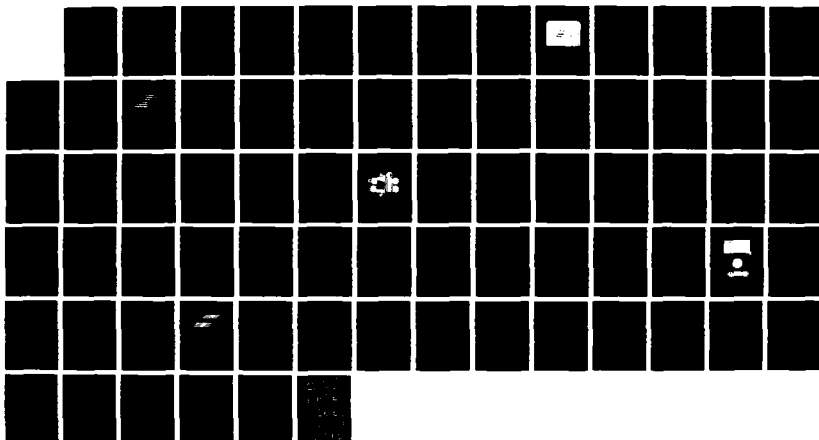
2/2

UNCLASSIFIED

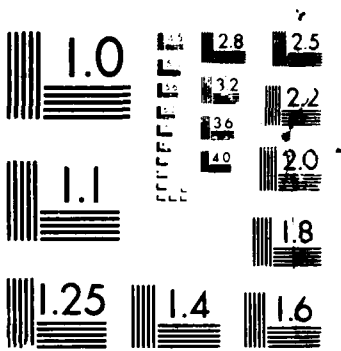
MAR 88 ARO-25045.1-EL DAAL03-88-K-0005

F/G 9/1

NL



100



MICROGRAPH RESOLUTION TEST CHART
NATIONAL BUREAU OF STANDARDS 1961

Figures 2.23(a) and 2.23(b) show the ohmic attenuation constants of sections A and B versus aspect ratio $s/(s+2w)$, respectively, with different cross-sectional size of CPW $s+2w$. From these figures, for a fixed $s/(s+2w)$ the larger the value of $s+2w$ the lower the skin current densities as well as the ohmic attenuation constants. Figs.2.24(a) and 2.24(b) represent the slow-wave factor and the ohmic attenuation constant, respectively, of the crosstie overlay slow-wave CPW versus aspect ratio $s/(s+2w)$ for different values of $s+2w$. In the calculation, $l_A=l_B=10 \mu\text{m}$ was assumed. From Figs.2.23(a)-2.24(b), the larger the value of $s+2w$, the larger the capacitance per unit length while the inductance per unit length is relatively unaffected. Therefore large values of $s+2w$ cause a larger slow-wave factor as well as a larger ohmic attenuation constant. Fig.2.25 shows the Q value versus aspect ratio $s/(s+2w)$ of the crosstie overlay slow-wave CPW with different values of $s+2w$. According to this figure, the larger the value of $s+2w$, the higher the Q-value obtained.

2.8 EXPERIMENTAL CONFIRMATION OF SLOW-WAVE PROPAGATION IN A CROSSTIE OVERLAY COPLANAR WAVEGUIDE

In this section, the slow-wave propagation along the new crosstie overlay CPW was investigated experimentally. In this experiment, a CPW pattern was photo-etched on a pre-thinned $15 \mu\text{m}$ Cu-clad Epsilam-10 substrate surface with $\epsilon_r=10.2$ and $h=0.635\text{mm}$ (h is the thickness of substrate). The center conductor width of CPW is $s=0.15\text{mm}$ and the slot width is $w=0.745\text{mm}$. Twenty periods of metal crossties were photo-etched on another pre-thinned $15 \mu\text{m}$ Cu-clad microwave

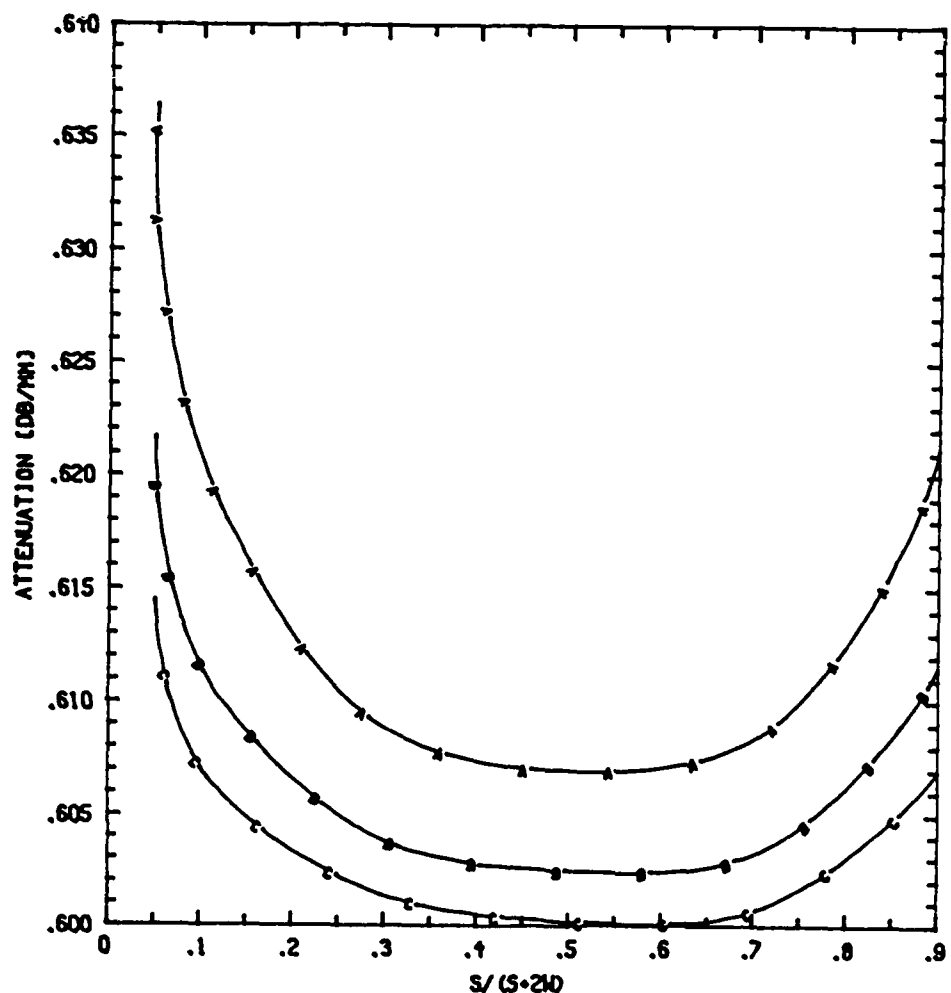


Fig.2.23(a) Ohmic attenuation constant versus aspect ratio of Section A with different cross-sectional sizes of CPWs.

$b = .001\text{mm}$, $h = .35\text{mm}$, $\epsilon_r = 12.9$ (S.I.GaAs), $\epsilon_r' = 6.5(\text{Si}_3\text{N}_4)$, $Au = 1.5\mu\text{m}$, $f = 10\text{GHz}$, Curve A--- $s+2w = 1.64\text{mm}$, Curve B--- $s+2w = 2.64\text{mm}$, Curve C--- $s+2w = 3.64\text{mm}$.

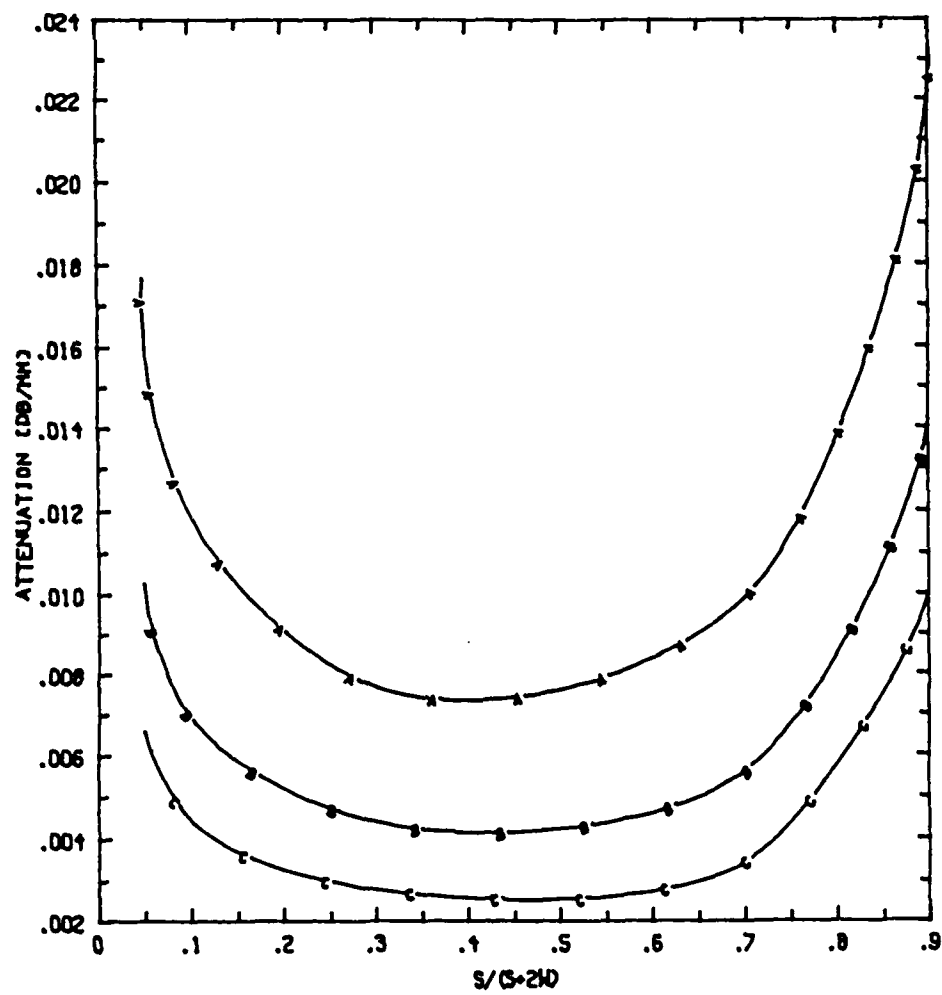


Fig.2.23(b) Ohmic attenuation constant versus aspect ratio of Section B with different cross-sectional sizes of CPWs.

$b = .001\text{mm}$, $h = .35\text{mm}$, $\epsilon_r = 12.9$ (S.I.GaAs), $\epsilon_r' = 6.5$ (Si_3N_4),
 $Au = 1.5\mu\text{m}$, $f = 10\text{GHz}$, Curve A---- $s + 2w = 1.64\text{mm}$, Curve B----
 $s + 2w = 2.64\text{mm}$, Curve C---- $s + 2w = 3.64\text{mm}$.

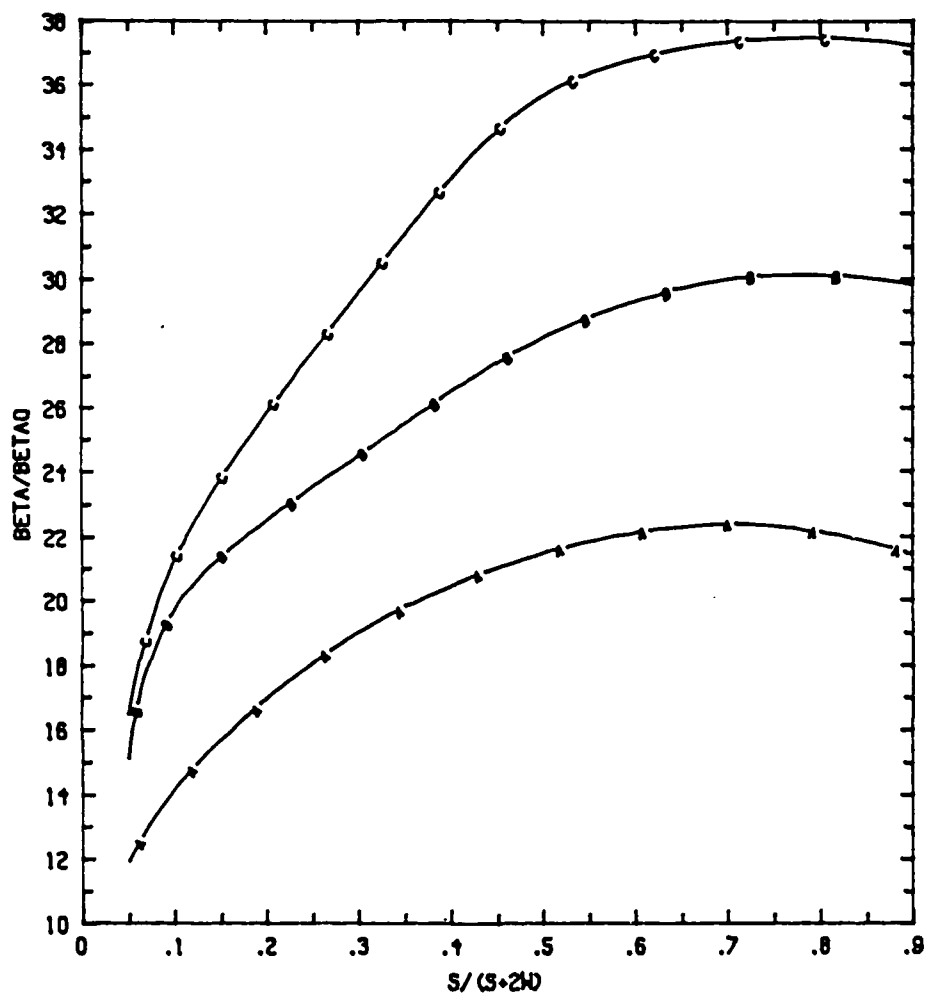


Fig.2.24(a) Slow-wave factor versus aspect ratio of crosstie overlay slow-wave CPWs with different cross-sectional sizes of CPWs.

$b=.001\text{mm}$, $h=.35\text{mm}$, $\epsilon_r=12.9$ (S.I.GaAs), $\epsilon_r'=6.5(\text{Si}_3\text{N}_4)$, $\text{Au}=1.5\mu\text{m}$, $l_A=l_B=.01\text{mm}$, $f=10\text{GHz}$, Curve A--- $s+2w=1.64\text{mm}$, Curve B--- $s+2w=2.64\text{mm}$, Curve C--- $s+2w=3.64\text{mm}$.

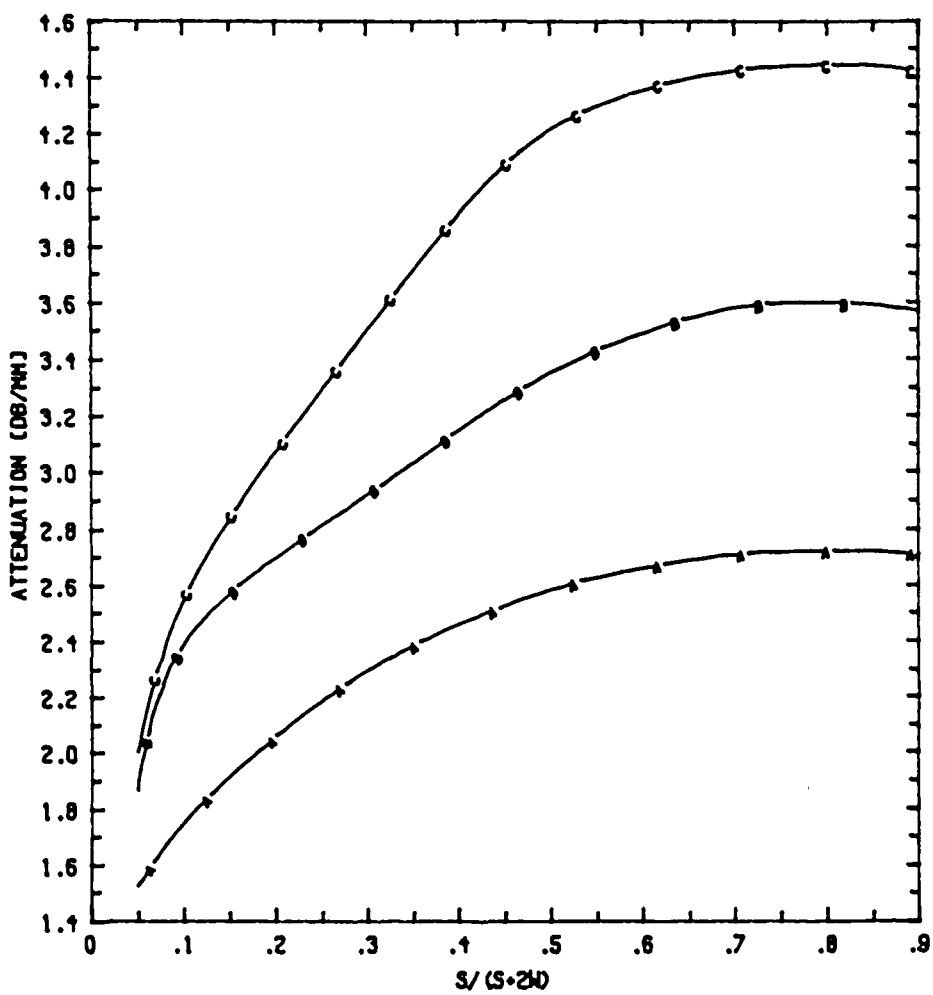


Fig.2.24(b) Ohmic attenuation constant versus aspect ratio of crosstie overlay slow-wave CPWs with different cross-sectional sizes of CPWs.

$b = .001\text{mm}$, $h = .35\text{mm}$, $\epsilon_r = 12.9$ (S.I.GaAs), $\epsilon_r' = 6.5$ (Si_3N_4), $\text{Au} = 1.5\mu\text{m}$, $l_A = l_B = .01\text{mm}$, $f = 10\text{GHz}$, Curve A--- $s+2w = 1.64\text{mm}$, Curve B--- $s+2w = 2.64\text{mm}$, Curve C--- $s+2w = 3.64\text{mm}$.

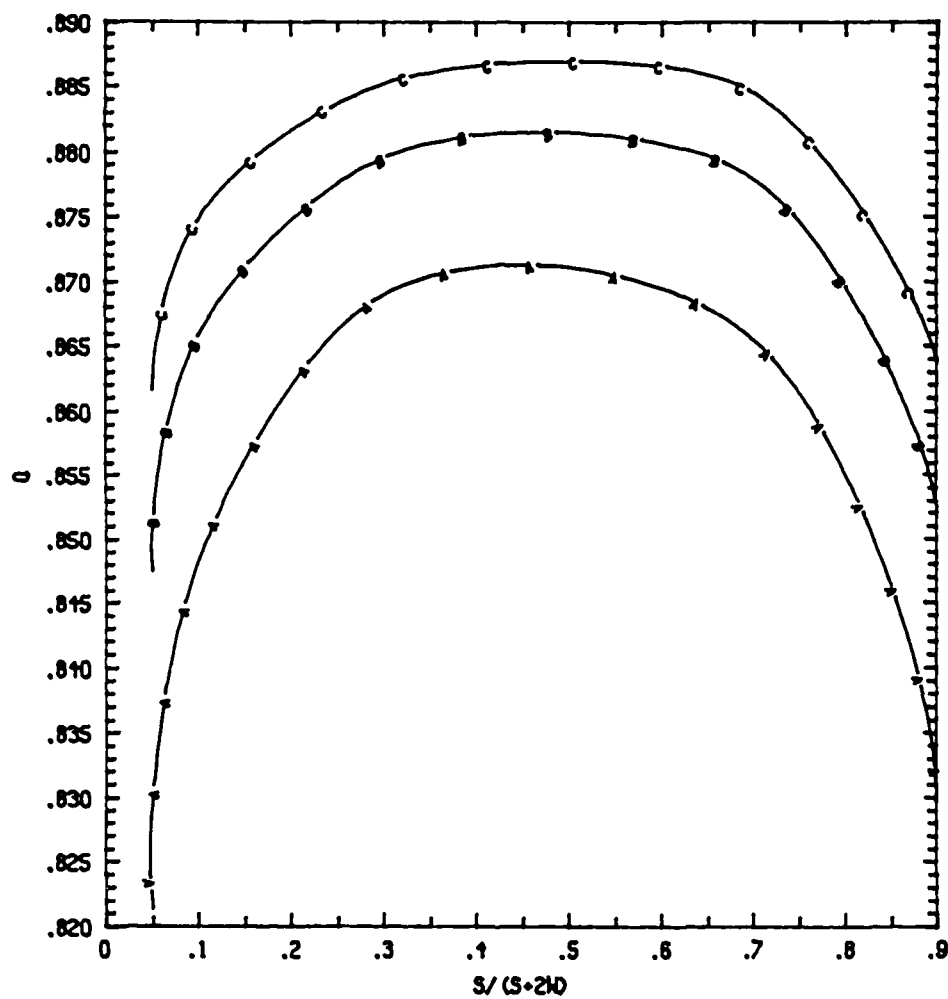


Fig.2.25 Quality factor versus aspect ratio of crosstie overlay slow-wave CPWs with different cross-sectional sizes of CPWs.

$b = .001\text{mm}$, $h = .35\text{mm}$, $\epsilon_r = 12.9$ (S.I.GaAs), $\epsilon_r' = 6.5(\text{Si}_3\text{N}_4)$,
 $Au = 1.5\mu\text{m}$, $l_A = l_B = .01\text{mm}$, $f = 10\text{GHz}$, Curve A---- $s+2w = 1.64\text{mm}$,
Curve B---- $s+2w = 2.64\text{mm}$, Curve C---- $s+2w = 3.64\text{mm}$.

substrate surface with $\epsilon_r=2.5$ and $h=0.762\text{mm}$. The lengths of the constituent sections in each period were $l_A=0.30\text{mm}$ (with crosstie strip) and $l_B=0.30\text{mm}$ (without crosstie strip). By using the spun-on technique, a $3.0\ \mu\text{m}$ thick DuPont PI-2556 polyimide ($\epsilon_r'=3.5$) layer was coated on the surface of the periodic crossties as the dielectric overlay. After the polyimide was properly cured (125^0C , 15 hours), construction of a crosstie slow-wave CPW was accomplished by attaching the substrate with the CPW and another with the crossties face-to-face. Mechanical pressure was applied to make sure that the two pieces had good contact.

The experimental verification of the slow-wave factor in the crosstie overlay slow-wave CPW was performed by measuring the phase shift using a Hewlett-Packard Network Analyzer. Fig.2.26 is a photograph of the disassembled crosstie overlay slow-wave CPW. Sections of $50\ \Omega$ conventional CPW were connected at the input and output ends. In the measurements, these $50\ \Omega$ CPW's were connected directly to form a calibration reference. The measured values of slow-wave factor are plotted against frequency in Fig.2.27. The measured slow-wave factor of a simple CPW without a crosstie pattern is also shown for comparison. These results indicate slow-wave propagation with a linear dispersion. Measured values of the slow-wave factor are close to the theoretical values shown by the solid line. The cause of the discrepancy includes the existence of an airgap due to the thickness of the crossties. The measured values of the attenuation constant are plotted against frequency in Fig.2.28. The measured attenuation constant of a simple CPW without a crosstie pattern is also shown for comparison. As shown in this figure, the crosstie overlay slow-wave CPW exhibits higher attenuation per unit physical length than the simple

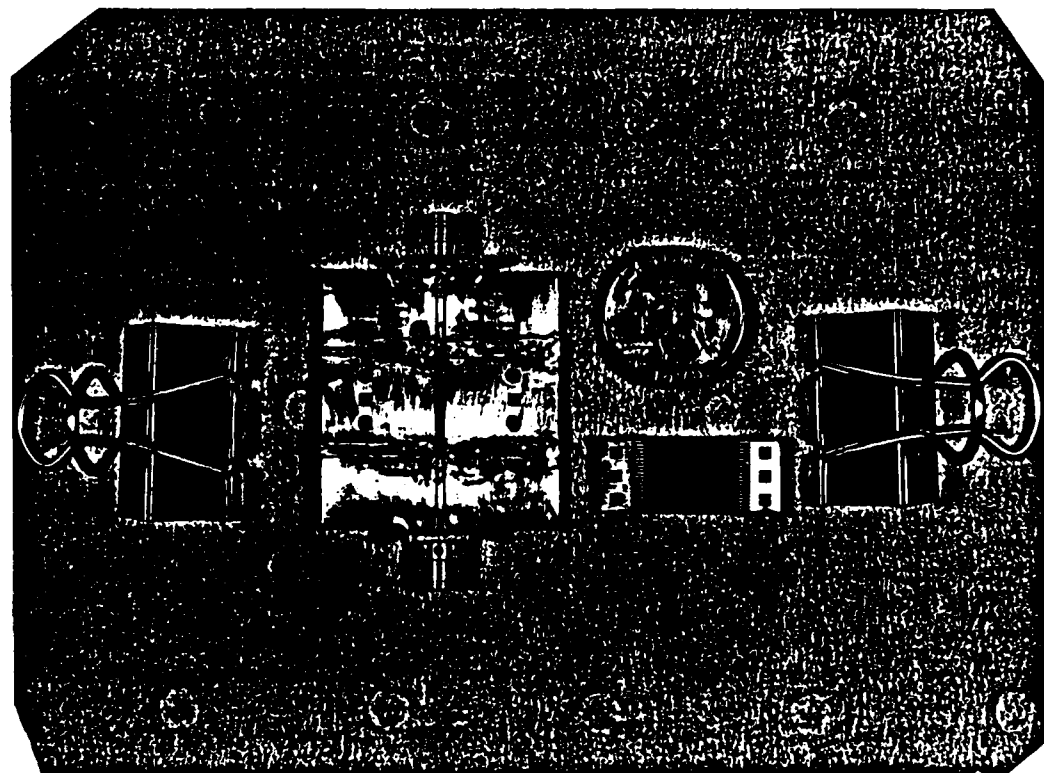


Fig.2.26 Photograph of the disassembled crosstie overlay slow-wave CPW
in experiment.

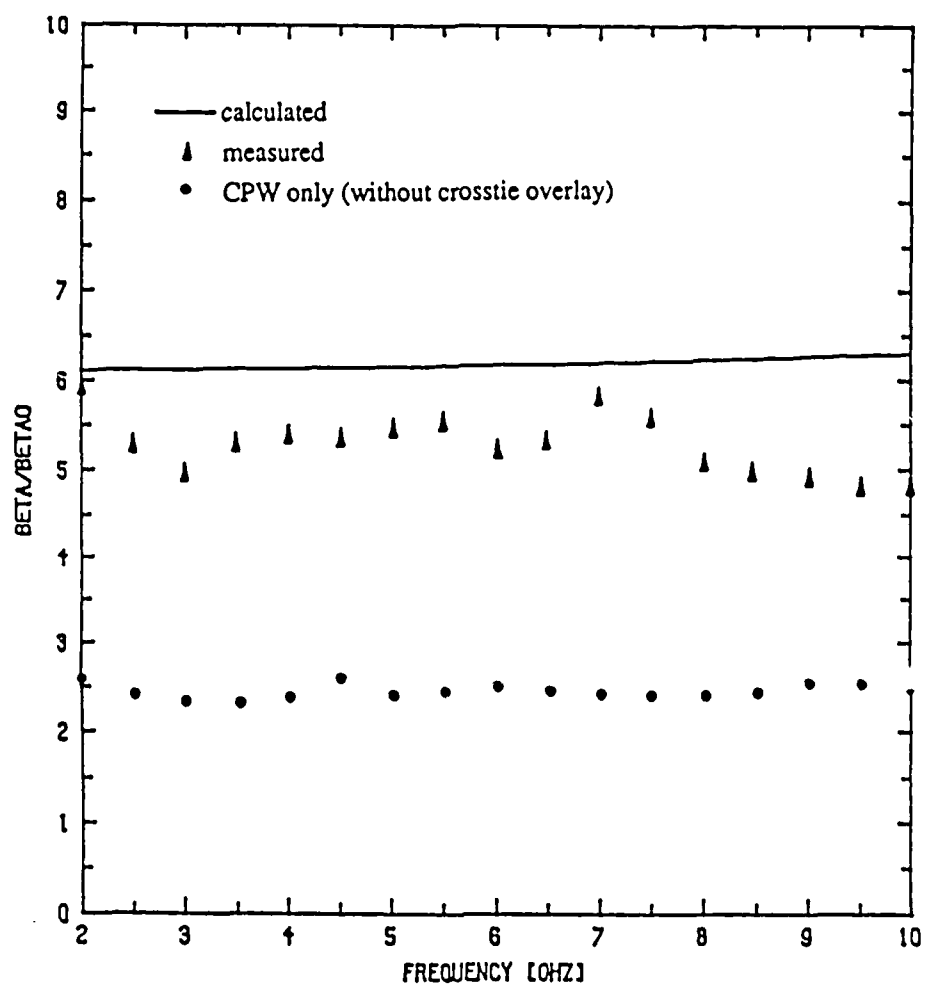


Fig.2.27 Slow-wave factor versus frequency for a crosstie overlay slow-wave CPW.

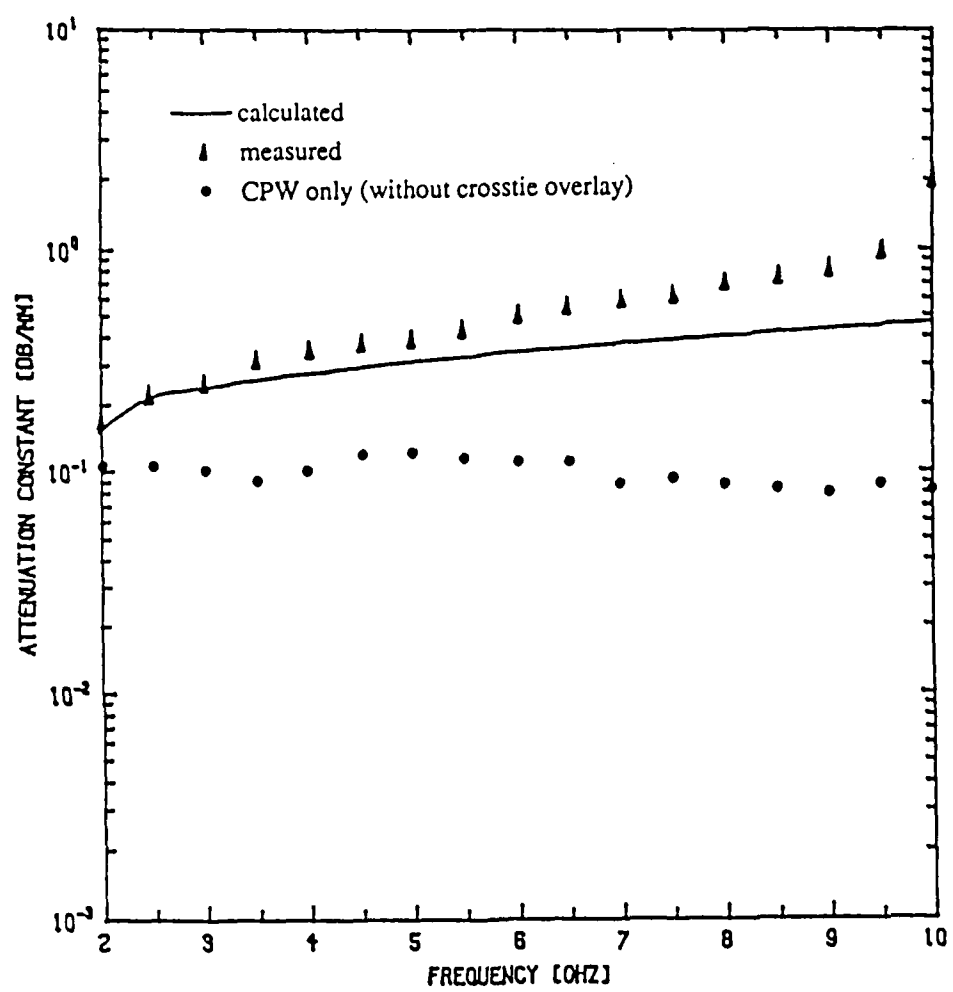


Fig.2.28 Attenuation constant versus frequency for a crosstie overlay slow-wave CPW.

CPW due to the existence of the crosstie conductors. However, the difference is much smaller if the values are compared with respect to the guide wavelength. Measured values of the attenuation constant agree reasonably with the theoretical values shown by the solid line.

From the above-mentioned quantities, the slow-wave propagation along the new crosstie overlay slow-wave CPW has been verified both theoretically and experimentally. From the extensive study carried out in this chapter, the combination of a thicker dielectric overlay, a larger cross-sectional size $s+2w$ of the CPW, and a smaller duty cycle $l_A/(l_A+l_B)$ together with an appropriate value of aspect ratio $s/(s+2w)$ appear to be the viable candidate structure for an optimized crosstie overlay slow-wave CPW implementation.

CHAPTER 3 : A BAND-REJECT GRATING MADE OF CROSSTIE OVERLAY SLOW-WAVE COPLANAR WAVEGUIDES

One of the problems of microwave and millimeter-wave integrated circuits is the lack of high-Q resonators except for a dielectric resonator. In monolithic integrated circuits, dielectric resonators are not compatible with the concept of monolithic integration. Microstrip patches provide a relatively low Q. In this chapter, we investigate the possibility of realizing resonators and oscillators, with a reasonable physical size, by the use of grating structures in a printed circuit form constructed with crosstie overlay slow-wave structures.

It is well known [31] that the electromagnetic wave propagating in a grating structure can be represented in terms of space harmonics with phase constants β_m given by

$$\beta_m = \beta_0 + \frac{2m\pi}{d} , \quad m=0,\pm 1,\pm 2, \dots \quad (3.1)$$

where d is the grating period and β_0 is the phase constant of the dominant ($m=0$) space harmonic determined by the excitation of the grating. If the perturbation due to a unit cell of the grating is small, β_0 is very close to the propagation constant in the unperturbed grating, except in the coupling regions of the frequency spectrum.

Fig.3.1(a) is a typical $k-\beta$ diagram for the $m=0$ (β_0), $m=-1$ (β_{-1}), and $m=-2$ (β_{-2}) forward-traveling space harmonics and the $m=-1$ ($-\beta_{-1}$) backward-traveling fundamental space harmonic propagating in a grating structure. In fact, mode-

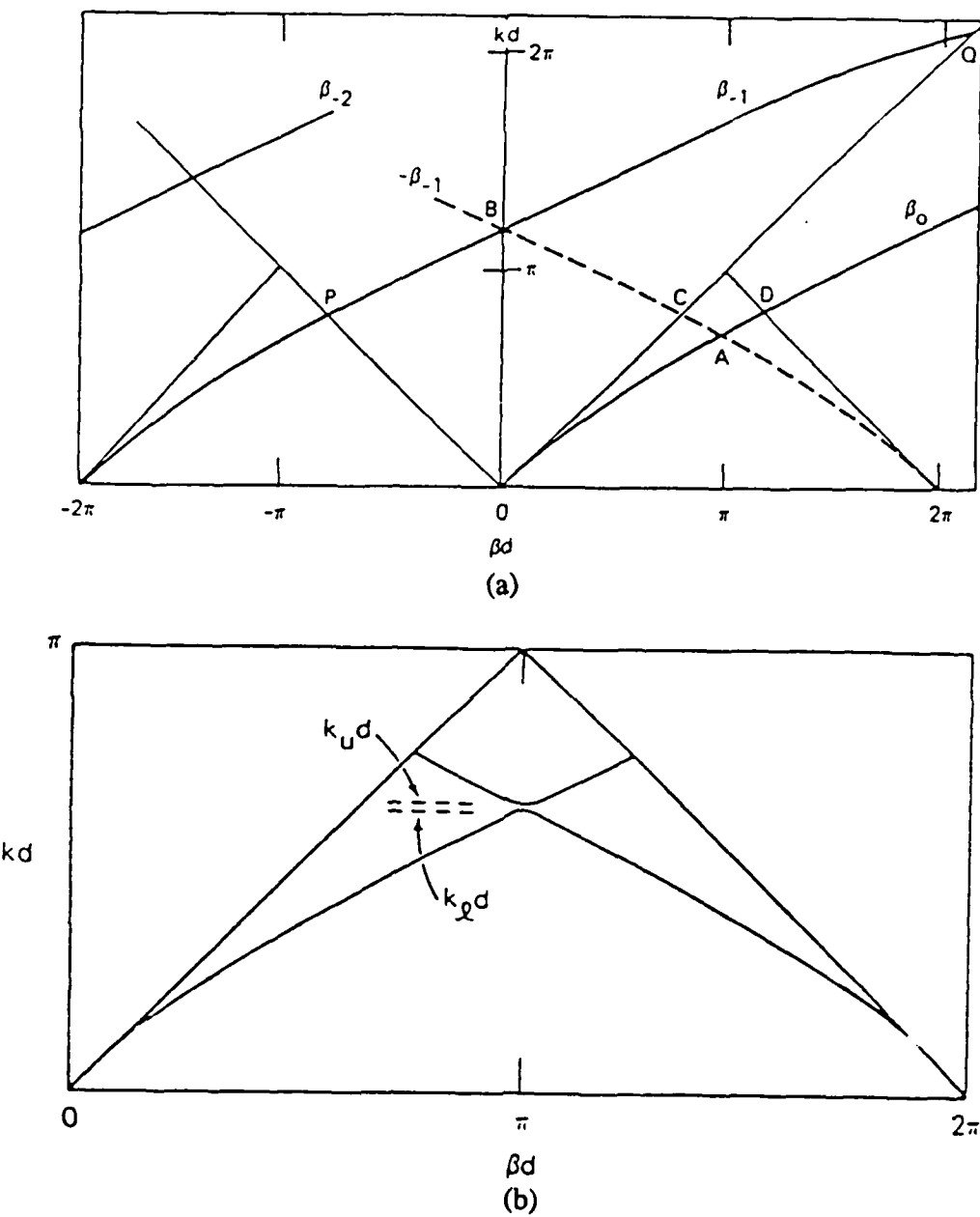


Fig.3.1 K- β diagram of a grating structure. (a) Wave coupling neglected, (b) Surface-wave stopband.

coupling phenomena occur at synchronous points such as A, B, C, and D. The mode-coupling phenomena can be used for deriving the dispersion relations for the grating structure such as the one shown in Fig.3.1(b). Note that if, for a given frequency, the period d is chosen such that $\beta_0 d$ is less than the value at D, no higher space harmonic radiates and the grating supports a surface wave.

When the grating period d and the phase constant β_0 of the fundamental wave satisfy the so-called Bragg reflection condition $\beta_0 d = \pi$ (point A in Fig.3.1(a)), the electromagnetic wave incident on the grating is reflected and the bandstop phenomenon occurs. This stopband results from the mode coupling between the forward-traveling fundamental β_0 and the $m=-1$ harmonic of the backward-traveling fundamental. In the following sections, the frequency-selective distributed Bragg reflection mechanism has been employed to create a compact grating based on the new crosstie overlay slow-wave CPW's as a possible high-Q circuit for application in monolithic microwave and millimeter-wave integrated circuits.

3.1 A DOUBLY-PERIODIC GRATING STRUCTURE AND THE TRANSMISSION-LINE EQUIVALENT CIRCUIT

As shown in Fig.3.2, we create a grating with its period comparable to the guide wavelength from the "uniform" crosstie overlay slow-wave CPW's. This "uniform" line itself is a periodic structure with its period much shorter than the wavelength and is designed as described in Section 2.4. Hence, the band-reject grating is physically a doubly periodic structure [32]. As shown in this figure, one period of the grating consists of two sections of crosstie overlay slow-wave CPW's

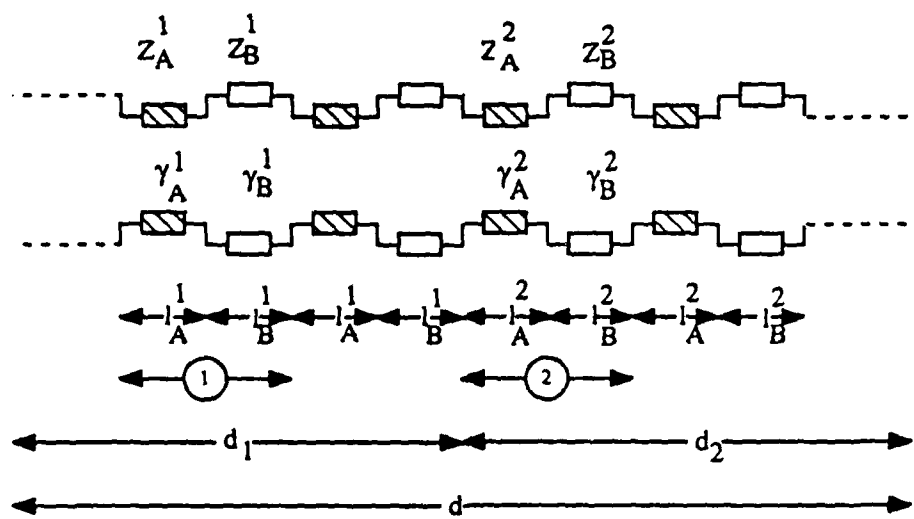
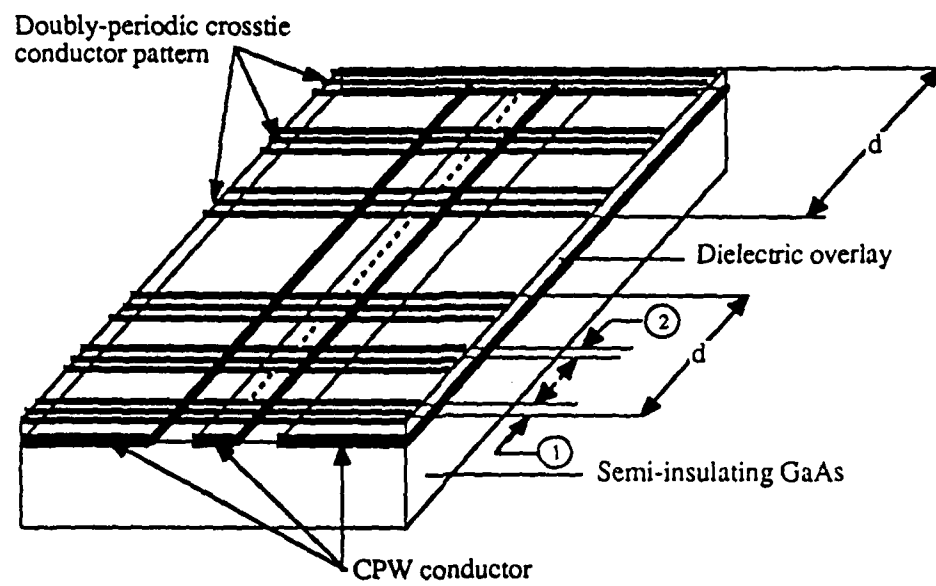


Fig.3.2 Schematic and equivalent circuit of a doubly-periodic band-reject grating.

with different slow-wave factors and characteristic impedances. The slow-wave CPW in Section d_1 comprises Section A and B of lengths l_A^1 and l_B^1 , respectively, while the one in Section d_2 is made of l_A^2 and l_B^2 long sections. Section d_1 contains m periods of $l_A^1+l_B^1$ while d_2 contains n periods of $l_A^2+l_B^2$. Hence, the length of the period of the band-reject grating is $d=d_1+d_2=mx(l_A^1+l_B^1)+nx(l_A^2+l_B^2)$.

To study the band-reject properties of this grating, the same analytical procedures used in calculating the propagation constant and characteristic impedance for the uniform crosstie slow-wave CPW's are used to obtain the transmission characteristics of the constituent sections $l_A^1+l_B^1$ and $l_A^2+l_B^2$ in Fig.3.2. Once the propagation constants and characteristic impedances of the two constituent crosstie slow-wave structures are obtained, appropriate lengths of the two sections d_1 and d_2 are chosen and cascaded to form a period of the band-reject grating. The reflection and transmission performances are then characterized by using the microwave two-port network cascading technique as described in the following section.

3.2 CHARACTERIZATION OF THE REFLECTION AND TRANSMISSION PROPERTIES OF A BAND-REJECT GRATING

The composite normalized transmission matrix of a symmetrical doubly-periodic band-reject grating with $N+1/2$ periods is obtained by cascading the normalized transmission matrices for the constituent sections d_1 and d_2 into the equivalent circuit shown in Fig.3.3 :

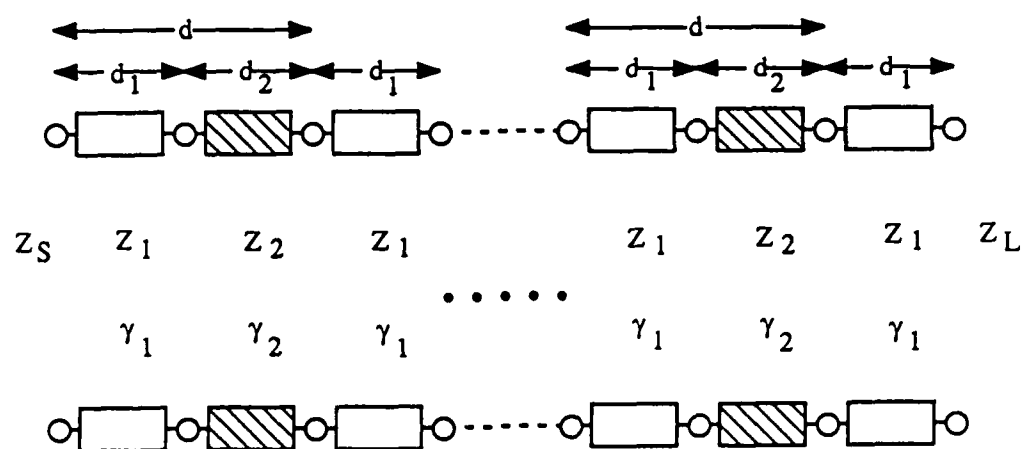


Fig.3.3 Transmission line equivalent circuit for characterizing the transmission and reflection properties of a symmetrical doubly-periodic band-reject grating.

$$\begin{bmatrix} \bar{A}_N & \bar{B}_N \\ \bar{C}_N & \bar{D}_N \end{bmatrix} = \begin{bmatrix} \sqrt{\frac{Z_1}{Z_S}} & 0 \\ 0 & \sqrt{\frac{Z_S}{Z_1}} \end{bmatrix} \left(\begin{bmatrix} \bar{A} & \bar{B} \\ \bar{C} & \bar{D} \end{bmatrix}_1 \begin{bmatrix} \bar{A} & \bar{B} \\ \bar{C} & \bar{D} \end{bmatrix}_{1-2} \begin{bmatrix} \bar{A} & \bar{B} \\ \bar{C} & \bar{D} \end{bmatrix}_2 \begin{bmatrix} \bar{A} & \bar{B} \\ \bar{C} & \bar{D} \end{bmatrix}_{2-1} \right)^N \begin{bmatrix} \bar{A} & \bar{B} \\ \bar{C} & \bar{D} \end{bmatrix}_1 \begin{bmatrix} \bar{A} & \bar{B} \\ \bar{C} & \bar{D} \end{bmatrix}_1 \begin{bmatrix} \bar{A} & \bar{B} \\ \bar{C} & \bar{D} \end{bmatrix}_1 \begin{bmatrix} \bar{A} & \bar{B} \\ \bar{C} & \bar{D} \end{bmatrix}_1 \quad (3.2)$$

where

$$\begin{bmatrix} \bar{A} & \bar{B} \\ \bar{C} & \bar{D} \end{bmatrix}_p = \begin{bmatrix} \cosh \gamma_p d_p & \sinh \gamma_p d_p \\ \sinh \gamma_p d_p & \cosh \gamma_p d_p \end{bmatrix} \quad (p=1,2) \quad (3.2a)$$

$$\begin{bmatrix} \bar{A} & \bar{B} \\ \bar{C} & \bar{D} \end{bmatrix}_{p-q} = \begin{bmatrix} \sqrt{\frac{Z_q}{Z_p}} & 0 \\ 0 & \sqrt{\frac{Z_p}{Z_q}} \end{bmatrix} \quad (p=1,2, q=2,1) \quad (3.2b)$$

γ_1, γ_2 : the complex propagation constants of sections d_1 and d_2 , respectively.

Z_1, Z_2 : the characteristic impedances of sections d_1 and d_2 , respectively.

d_1, d_2 : the lengths of sections d_1 and d_2 , respectively.

Z_S, Z_L : the impedances connected to the input and output ends, respectively.

After the composite normalized transmission matrix is computed, it is converted to a scattering matrix according to the following relationship:

$$[S] = \begin{bmatrix} s_{11} & s_{12} \\ s_{21} & s_{22} \end{bmatrix} = \begin{bmatrix} \frac{\bar{A}_N + \bar{B}_N - \bar{C}_N - \bar{D}_N}{\Delta} & \frac{2(\bar{A}_N \bar{D}_N - \bar{B}_N \bar{C}_N)}{\Delta} \\ \frac{2}{\Delta} & \frac{-\bar{A}_N + \bar{B}_N - \bar{C}_N + \bar{D}_N}{\Delta} \end{bmatrix} \quad (3.3)$$

where $\Delta = \bar{A}_N + \bar{B}_N + \bar{C}_N + \bar{D}_N$

From (3.3) the power insertion loss and return loss are computed by

$$\text{Insertion Loss} = 20 \log_{10} \frac{1}{|s_{21}|} \quad (\text{dB}) \quad (3.4a)$$

$$\text{Return Loss} = 20 \log_{10} \frac{1}{|s_{11}|} \quad (\text{dB}) \quad (3.4b)$$

In addition, in order to learn how the input impedance of the band-reject grating behaves, we apply simple impedance transforms as shown in Fig.3.4 to analyze the resulting structure. For example,

$$\begin{aligned} Z_1 &= Z_1 \frac{Z_L + Z_1 \tanh \gamma_1 d_1}{Z_1 + Z_L \tanh \gamma_1 d_1} \\ Z_2 &= Z_2 \frac{Z_1 + Z_2 \tanh \gamma_2 d_2}{Z_2 + Z_1 \tanh \gamma_2 d_2} \\ &\vdots \\ &\vdots \\ Z_{2N} &= Z_2 \frac{Z_{2N-1} + Z_2 \tanh \gamma_2 d_2}{Z_2 + Z_{2N-1} \tanh \gamma_2 d_2} \\ Z_{in} &= Z_1 \frac{Z_{2N} + Z_1 \tanh \gamma_1 d_1}{Z_1 + Z_{2N} \tanh \gamma_1 d_1} \end{aligned} \quad (3.5)$$

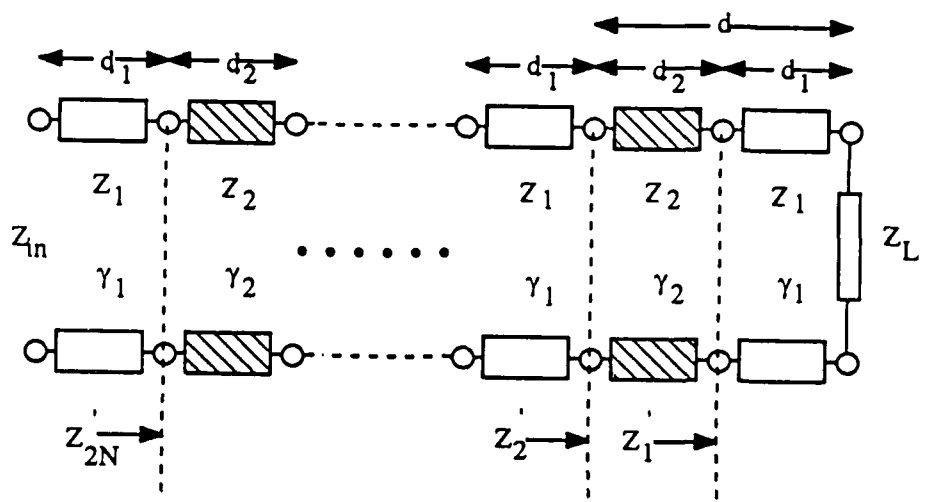


Fig.3.4 Impedance transforms for input impedance calculation for a doubly-periodic band-reject grating.

The stopband center frequency of the band-reject grating should located at the frequency where the imaginary part of the input impedance Z_{in} becomes zero.

3.3 PREDICTED CHARACTERISTICS OF A BAND-REJECT GRATING

Figs.3.5(a)-(c) show the variation of the moduli of the power insertion and return loss versus frequency for the band-reject grating as different numbers of periods are comprised. It is seen that the greater the number of periods, the more sensitive (higher insertion loss as well as narrower stopband width) the power reflectivity becomes with respect to frequency. In addition, by a reason similar to that for the crosstie overlay slow-wave CPW, the band-reject effect of the grating is maximum when the lengths of constituent sections d_1 and d_2 are identical. That maximum insertion loss increases as the dielectric overlay thickness decreases is also found. Figs. 3.6(a) and 3.6(b) give the real part and the imaginary part, respectively, of the input impedance of the band-reject grating with 9.5 periods. Bandstop phenomena occur at the frequency where the imaginary part of the input impedance becomes zero and the real part positive maximum. In the calculations for Figs.3.5(a)-3.6(b), the conductor loss has been neglected.

To study how the wave attenuation due to the conductor loss affects the grating performance, we evaluated the reflection and transmission characteristics of the grating structure in the presence of conductor loss. Based on the incremental inductance approach, the attenuation constants were calculated for every constituent section of the grating. The results have then been used in the calculation of the

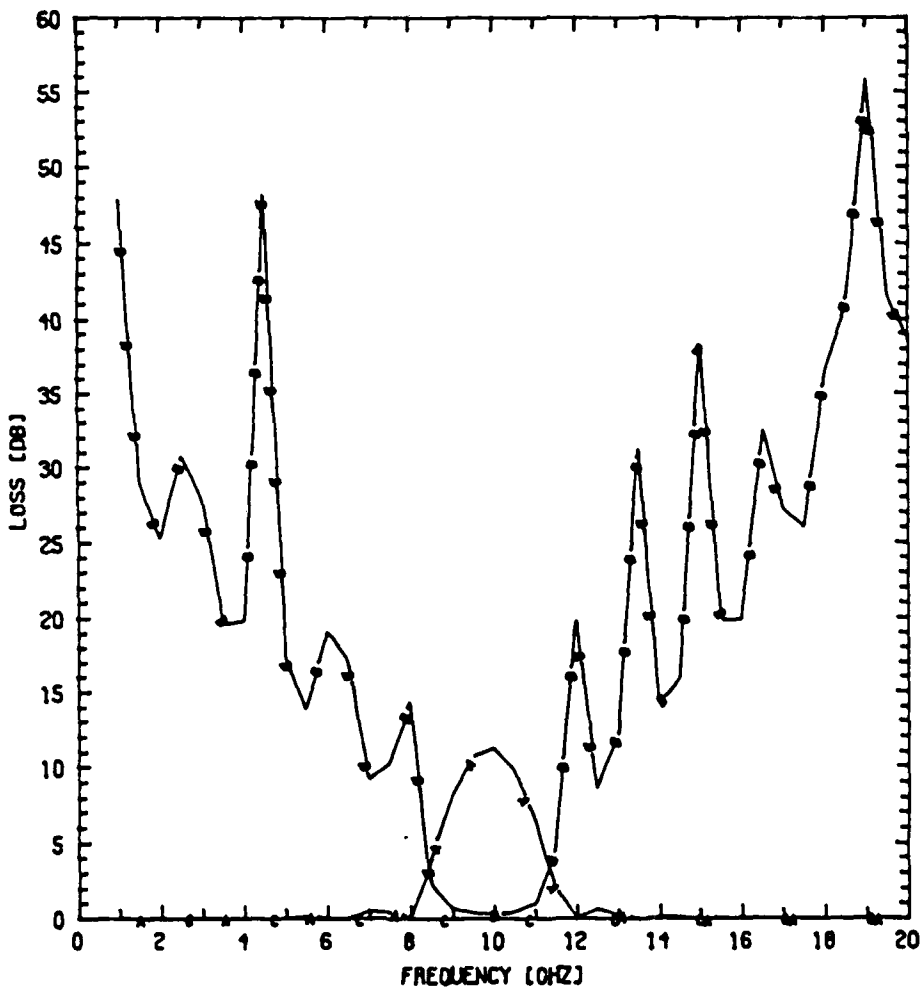


Fig.3.5(a) Insertion loss and return loss of a doubly-periodic band-reject grating with lossless conductors and 5.5 periods.

$s = .15\text{mm}$, $w = .745\text{mm}$, $b = .001\text{mm}$, $h = .35\text{mm}$, $\epsilon_r = 12.9$
 (S.I.GaAs), $\epsilon_r' = 6.5(\text{Si}_3\text{N}_4)$, $Z_S = Z_L = 8.0\Omega$, $l_A^1 = .005\text{mm}$,
 $l_B^1 = .006\text{mm}$, $l_A^2 = .006\text{mm}$, $l_B^2 = .005\text{mm}$, $d_1 = d_2 = .55\text{mm}$, $N = 5$,
 Curve A----Insertion loss, Curve B----Return loss.

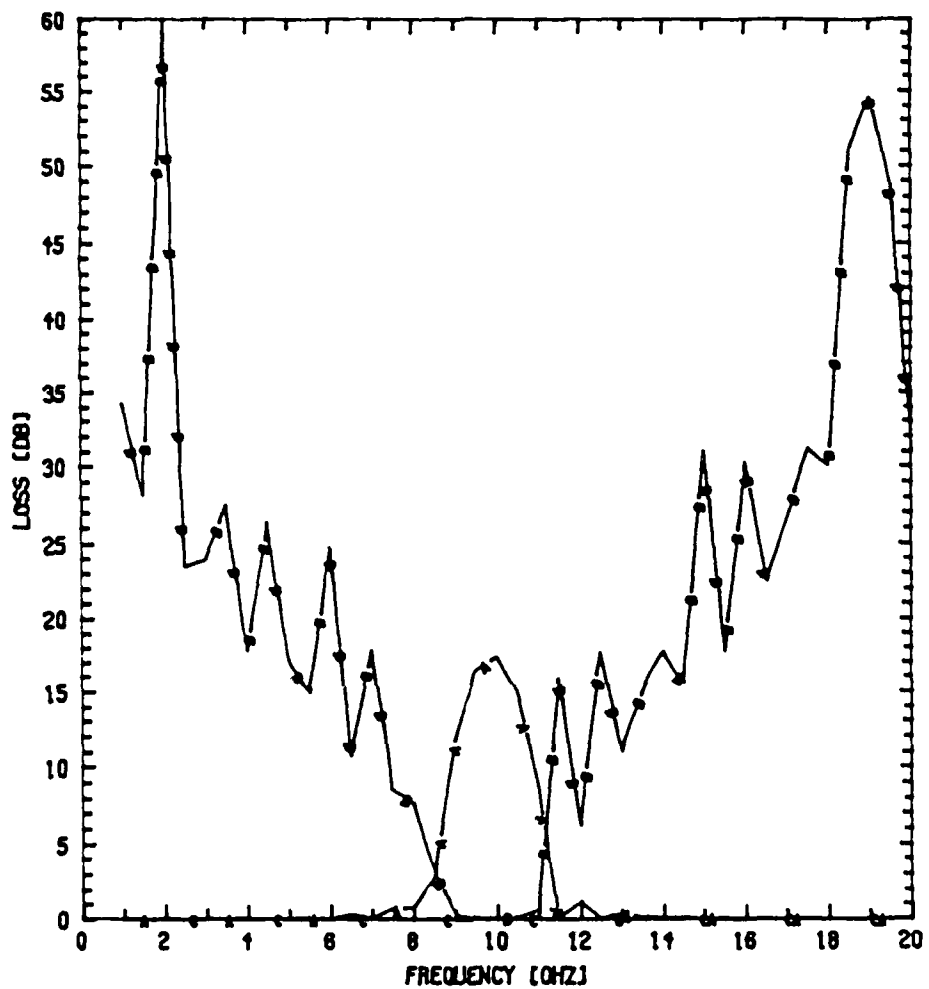


Fig.3.5(b) Insertion loss and return loss of a doubly-periodic band-reject grating with lossless conductors and 7.5 periods.

$s=.15\text{mm}$, $w=.745\text{mm}$, $b=.001\text{mm}$, $h=.35\text{mm}$, $\epsilon_r=12.9$
 (S.I.GaAs), $\epsilon_{r'}=6.5(\text{Si}_3\text{N}_4)$, $Z_S=Z_L=8.0\Omega$, $l_A^1=.005\text{mm}$,
 $l_B^1=.006\text{mm}$, $l_A^2=.006\text{mm}$, $l_B^2=.005\text{mm}$, $d_1=d_2=.55\text{mm}$, $N=7$,
 Curve A---Insertion loss, Curve B---Return loss.

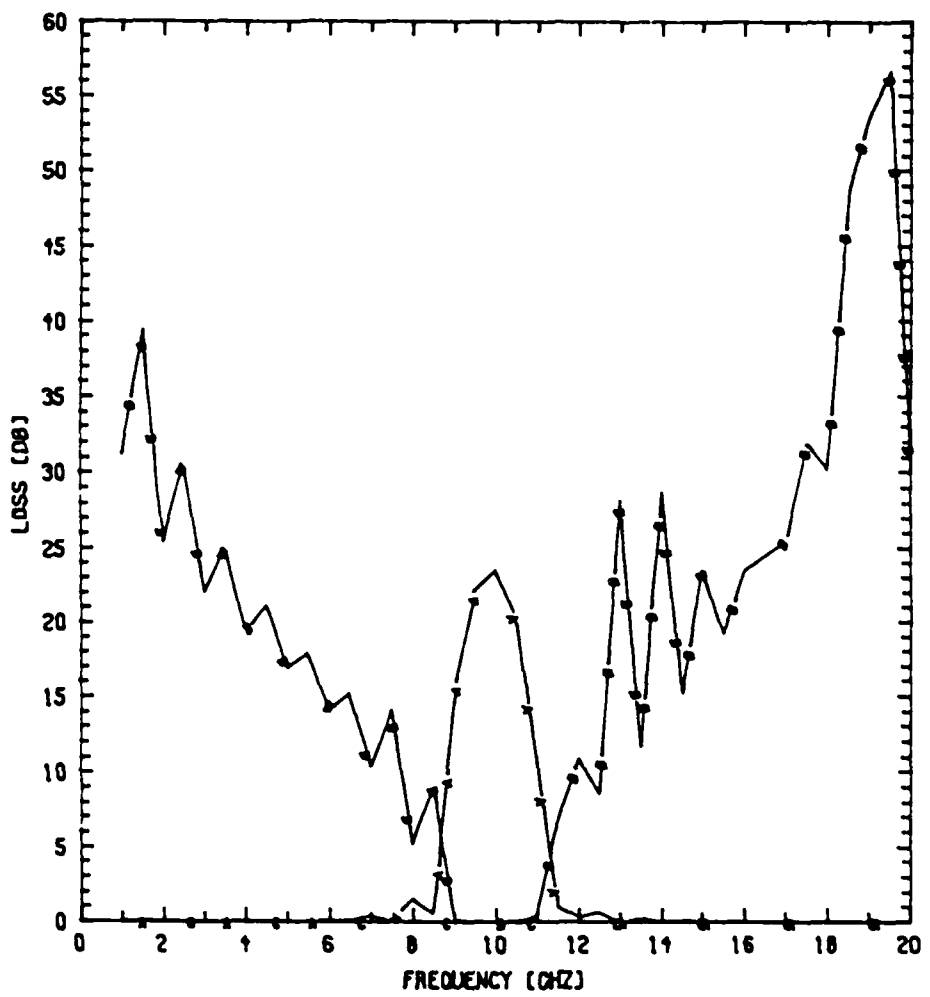


Fig.3.5(c) Insertion loss and return loss of a doubly-periodic band-reject grating with lossless conductors and 9.5 periods.

$s=.15\text{mm}$, $w=.745\text{mm}$, $b=.001\text{mm}$, $h=.35\text{mm}$, $\epsilon_r=12.9$
(S.I.GaAs), $\epsilon_r'=6.5(\text{Si}_3\text{N}_4)$, $Z_S=Z_L=8.0\Omega$, $l_{A1}=.005\text{mm}$,
 $l_{B1}=.006\text{mm}$, $l_{A2}=.006\text{mm}$, $l_{B2}=.005\text{mm}$, $d_1=d_2=.55\text{mm}$, $N=9$,
Curve A---Insertion loss, Curve B---Return loss.

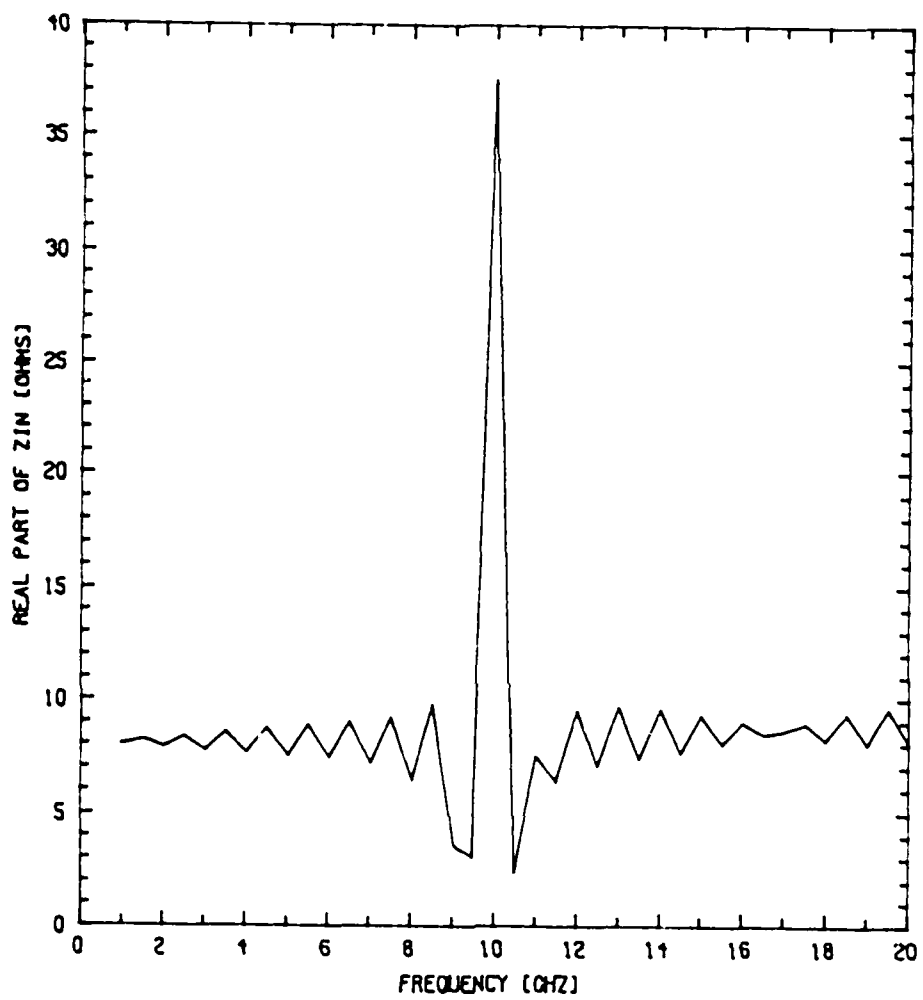


Fig.3.6(a) Real part of the input impedance of a doubly-periodic band-reject grating with lossless conductors and 9.5 periods.

$s = .15\text{mm}$, $w = .745\text{mm}$, $b = .001\text{mm}$, $h = .35\text{mm}$, $\epsilon_r = 12.9$
 (S.I.GaAs), $\epsilon_r' = 6.5(\text{Si}_3\text{N}_4)$, $Z_L = 8.0\Omega$, $l_A^1 = .005\text{mm}$,
 $l_B^1 = .006\text{mm}$, $l_A^2 = .006\text{mm}$, $l_B^2 = .005\text{mm}$, $d_1 = d_2 = .55\text{mm}$.

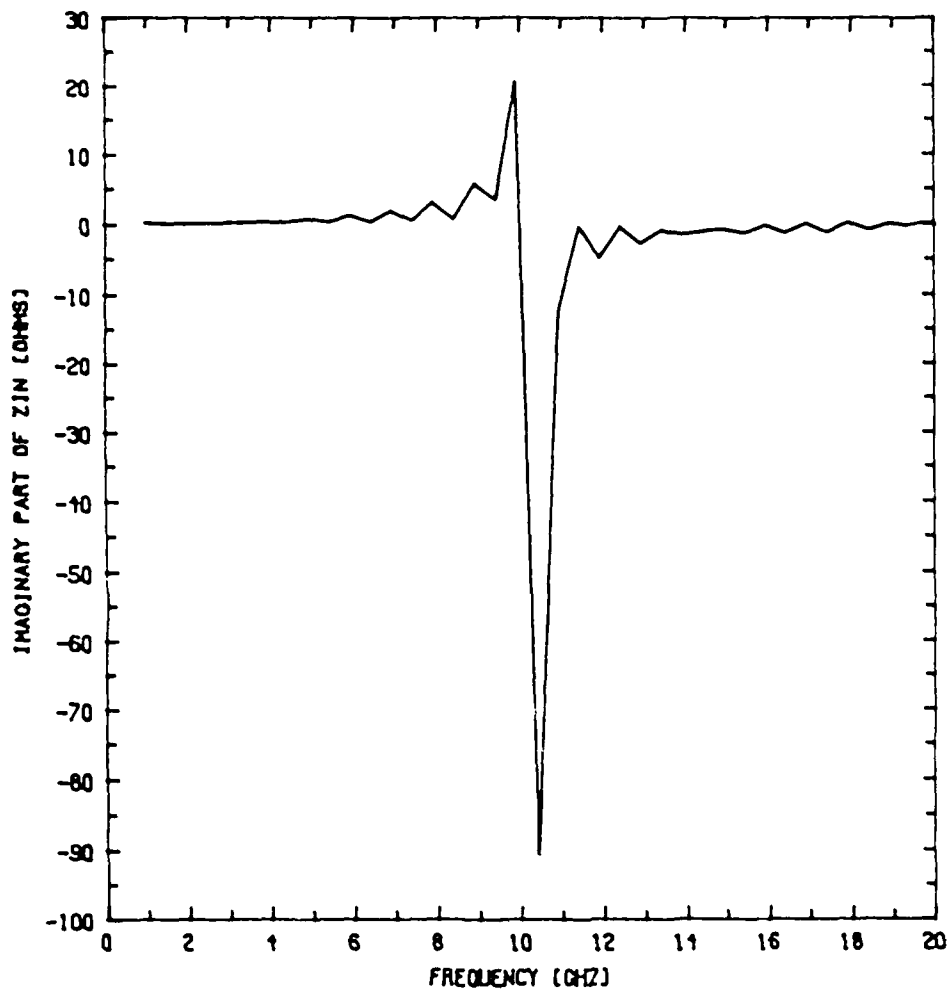


Fig.3.6(b) Imaginary part of the input impedance of a doubly-periodic band-reject grating with lossless conductors and 9.5 periods.

$s = .15\text{ mm}$, $w = .745\text{ mm}$, $b = .001\text{ mm}$, $h = .35\text{ mm}$, $\epsilon_r = 12.9$
 (S.I.GaAs), $\epsilon_r' = 6.5$ (Si₃N₄), $Z_L = 8.0\Omega$, $l_A^1 = .005\text{ mm}$,
 $l_B^1 = .006\text{ mm}$, $l_A^2 = .006\text{ mm}$, $l_B^2 = .005\text{ mm}$, $d_1 = d_2 = .55\text{ mm}$.

reflection and transmission characteristics. Figs. 3.7(a) and 3.7(b) are the insertion and return losses of the band-reject grating with 9.5 periods after taking the conductor loss into account. Due to the conductor loss, the peak reflectivity in the stopband has been reduced but the total insertion loss was increased. Figs. 3.8(a) and 3.8 (b) are the real and the imaginary parts of the grating input impedance after taking the conductor loss into account. It may be noted that the input impedance is not very sensitive to frequency in the passband, and hence broad-band matching with the external circuit may not be difficult to achieve.

3.4 EXPERIMENTAL RESULTS FOR A BAND-REJECT GRATING

As shown in Fig.3.2, we have constructed a doubly-periodic band-reject grating from the "uniform" crosstie overlay slow-wave CPW's. In reference to this figure, the following dimensions have been used : $l_A^1=0.10\text{mm}$, $l_B^1=0.12\text{mm}$, $l_A^2=0.12\text{mm}$ and $l_B^2=0.10\text{mm}$. The Section d_1 contains 17 periods of $l_A^1+l_B^1$ whereas d_2 contains 17 periods of $l_A^2+l_B^2$. Hence, the length of the period d of the band-reject grating is 7.48mm. The Section d_1 has a higher characteristic impedance than the Section d_2 . Following fabrication procedures similar to those for the crosstie overlay slow-wave CPW described in Section 2.8, a 9.5 period long grating with total length 7.106cm (9.5xd) was finally obtained. Fig.3.9 is a photograph of the disassembled band-reject grating. It should be noted that, before the design of the grating, the slow-wave factor is recalculated to include the airgap effect so that the discrepancy between the calculated and measured slow-wave factors is much smaller than the one observed in Fig.2.27.

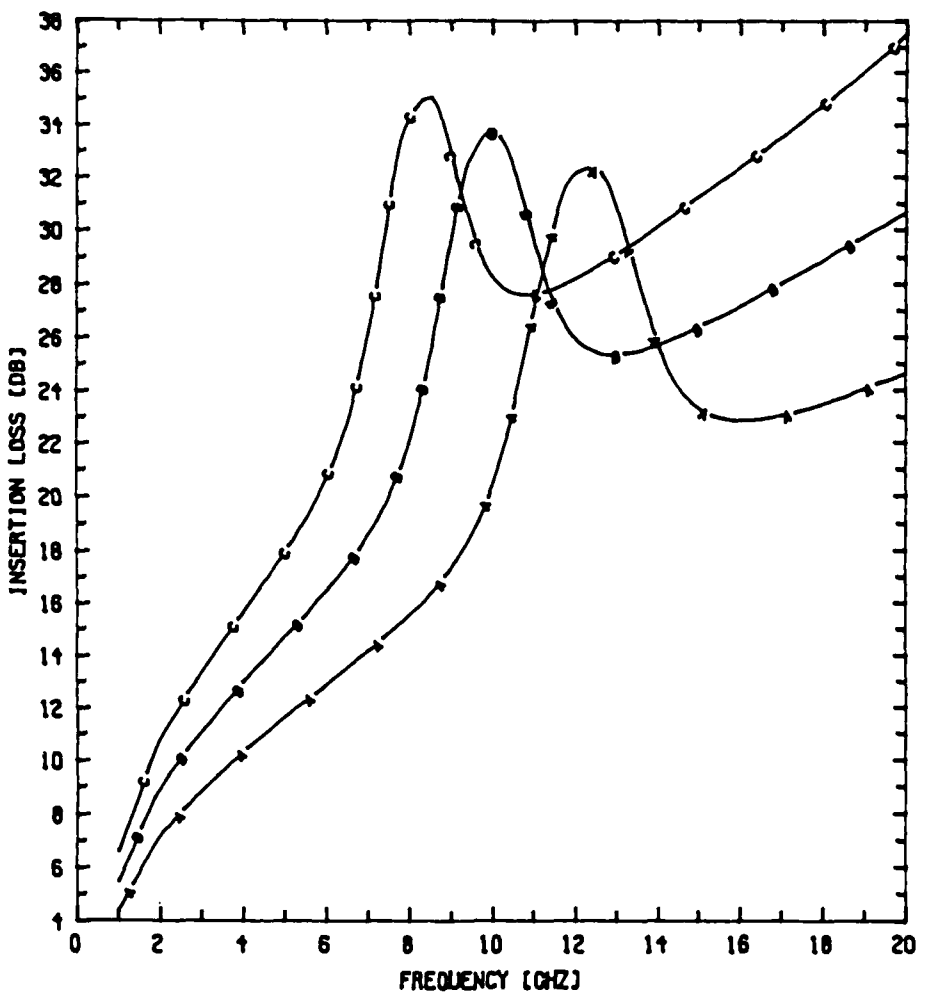


Fig.3.7(a) Insertion loss of a doubly-periodic band-reject grating with lossy conductors and 9.5 periods.

$s = .15\text{mm}$, $w = .745\text{mm}$, $b = .001\text{mm}$, $h = .35\text{mm}$, $\epsilon_r = 12.9$ (S.I.GaAs), $\epsilon_r' = 6.5(\text{Si}_3\text{N}_4)$, $Au = 1.5\mu\text{m}$, $Z_S = Z_L = 8.0\Omega$, $l_A^1 = .005\text{mm}$, $l_B^1 = .006\text{mm}$, $l_A^2 = .006\text{mm}$, $l_B^2 = .005\text{mm}$, Curve A--- $d_1 = d_2 = .44\text{mm}$, Curve B--- $d_1 = d_2 = .55\text{mm}$, Curve C--- $d_1 = d_2 = .66\text{mm}$.

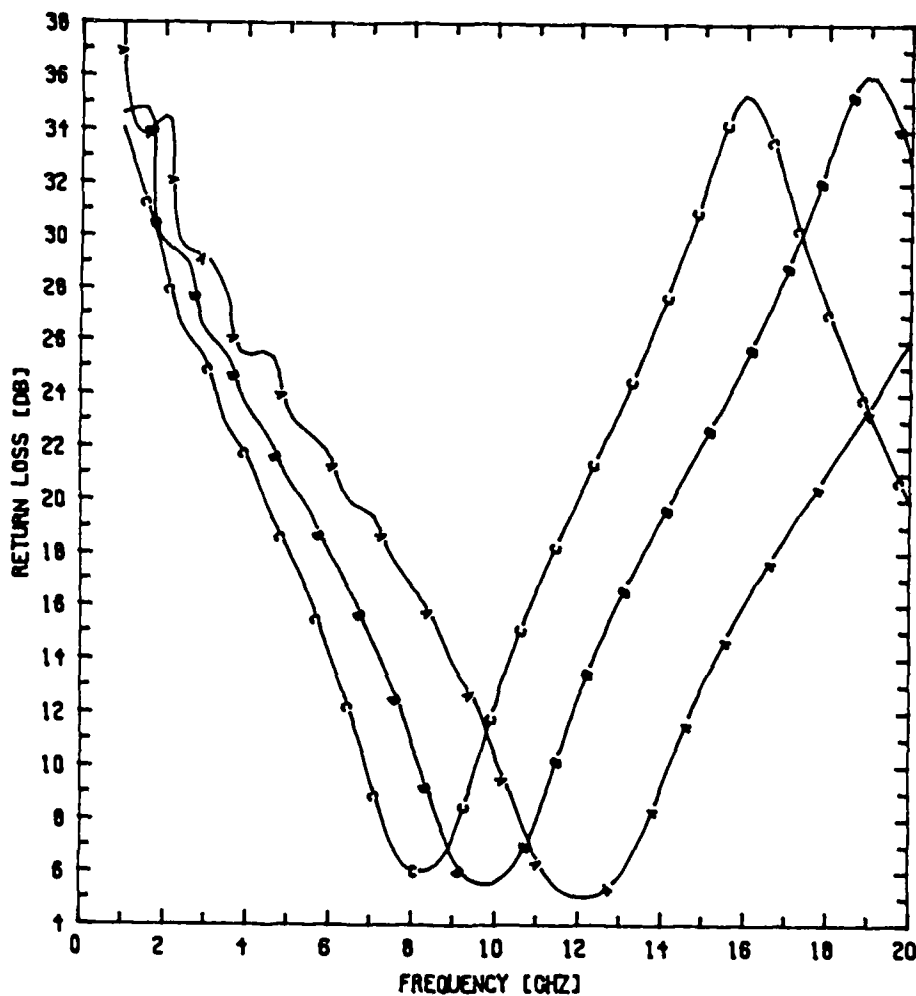


Fig.3.7(b) Return loss of a doubly-periodic band-reject grating with lossy conductors and 9.5 periods.

$s=.15\text{mm}$, $w=.745\text{mm}$, $b=.001\text{mm}$, $h=.35\text{mm}$, $\epsilon_r=12.9$ (S.I.GaAs), $\epsilon_r'=6.5(\text{Si}_3\text{N}_4)$, $\text{Au}=1.5\mu\text{m}$, $Z_S=Z_L=8.0\Omega$, $l_A^1=.005\text{mm}$, $l_B^1=.006\text{mm}$, $l_A^2=.006\text{mm}$, $l_B^2=.005\text{mm}$, Curve A---- $d_1=d_2=.44\text{mm}$, Curve B---- $d_1=d_2=.55\text{mm}$, Curve C---- $d_1=d_2=.66\text{mm}$.

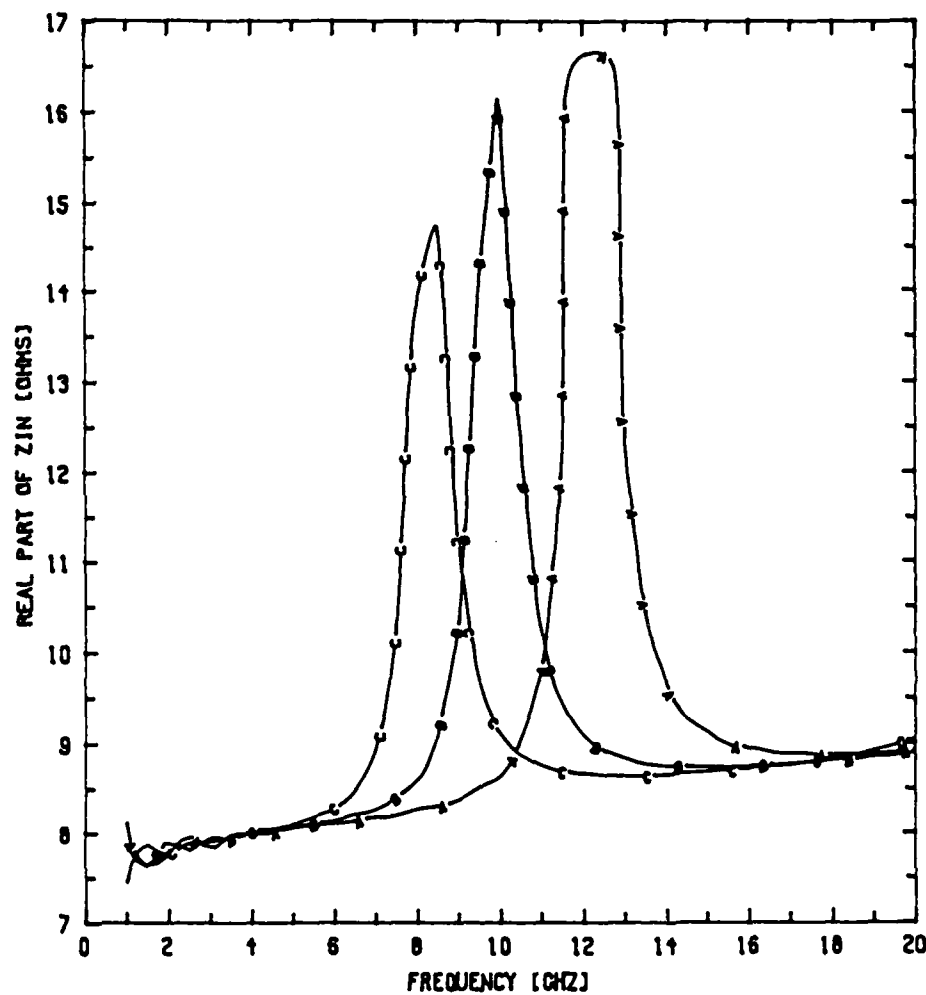


Fig.3.8(a) Real part of the input impedance of a doubly-periodic band-reject grating with lossy conductors and 9.5 periods.

$s=.15\text{mm}$, $w=.745\text{mm}$, $b=.001\text{mm}$, $h=.35\text{mm}$, $\epsilon_r=12.9$
 (S.I.GaAs), $\epsilon_r'=6.5(\text{Si}_3\text{N}_4)$, $Au=1.5\mu\text{m}$, $Z_L=8.0\Omega$, $l_A^1=.005\text{mm}$,
 $l_B^1=.006\text{mm}$, $l_A^2=.006\text{mm}$, $l_B^2=.005\text{mm}$, Curve A----
 $d_1=d_2=.44\text{mm}$, Curve B---- $d_1=d_2=.55\text{mm}$, Curve C----
 $d_1=d_2=.66\text{mm}$.

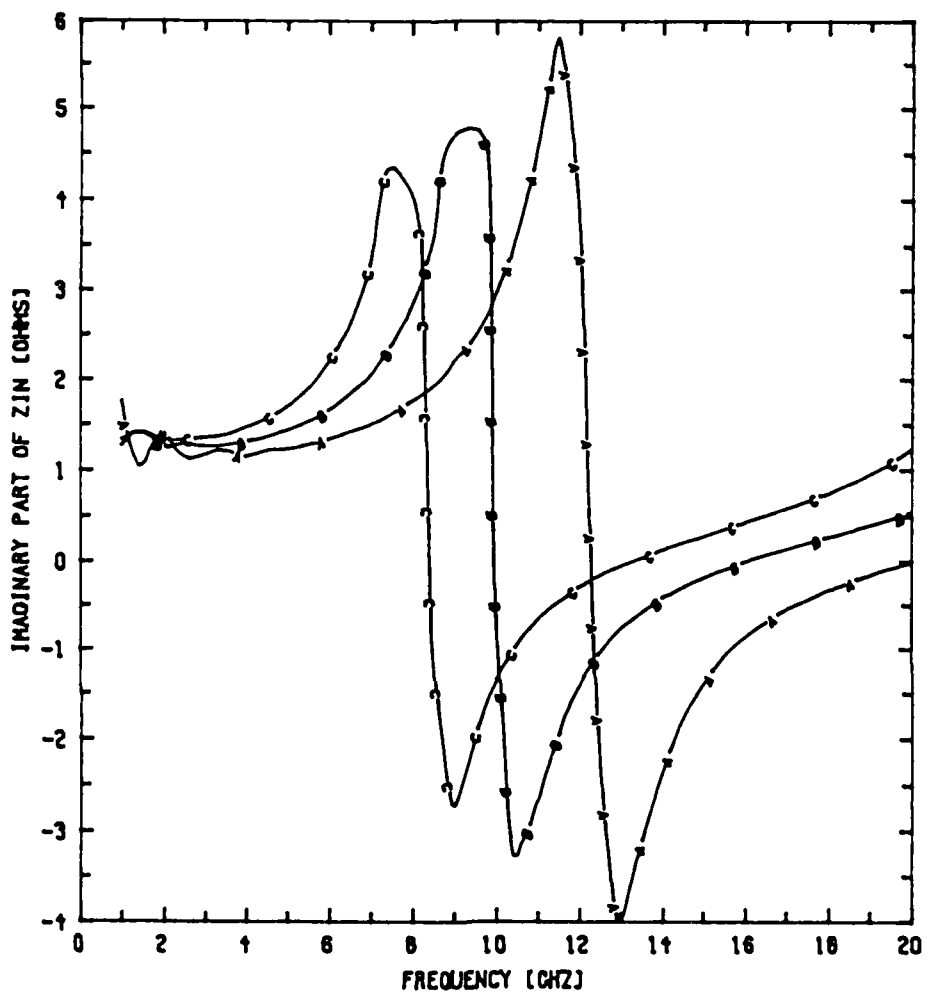


Fig.3.8(b) Imaginary part of the input impedance of a doubly-periodic band-reject grating with lossy conductors and 9.5 periods.

$s=.15\text{mm}$, $w=.745\text{mm}$, $b=.001\text{mm}$, $h=.35\text{mm}$, $\epsilon_r=12.9$
 (S.I.GaAs), $\epsilon_r'=6.5(\text{Si}_3\text{N}_4)$, $\text{Au}=1.5\mu\text{m}$, $Z_L=8.0\Omega$, $l_A^1=.005\text{mm}$,
 $l_B^1=.006\text{mm}$, $l_A^2=.006\text{mm}$, $l_B^2=.005\text{mm}$, Curve A----
 $d_1=d_2=.44\text{mm}$, Curve B---- $d_1=d_2=.55\text{mm}$, Curve C----
 $d_1=d_2=.66\text{mm}$.

In the measurements, a section of 50Ω conventional CPW was used at the input and output ends, respectively, as the test fixture. The same setup as that in the slow-wave factor measurement was exploited for the characterization of grating reflection and transmission properties. Fig.3.10 shows the calculated and the measured values of insertion loss and Fig.3.11 shows the return loss plotted against frequency for the fabricated grating. From these two figures, a band rejection phenomenon can be clearly recognized. The center frequency of the stopband is 4.95 GHz in experiment and 5.03 GHz in theory. The difference is about 1.6 %. The 3-dB bandwidth of the stopband is 0.56 GHz in the experiment and 0.50 GHz from the theory. The difference is caused not only by the errors in fabrication but also by the fact that the junction susceptance between two transmission lines was not taken into account in the theoretical calculation. The Q value inside the stopband is around 8.8 in the experiment and 10 for the theory. The peak insertion loss and the return loss in the stopband are 31 dB and 6 dB in the experiment, 30 dB and 5 dB for the theory, respectively. The slow-wave factor of this band-reject grating is about 4. The physical length of the present device is reduced to no more than 25 % of the length of the conventional grating with the same stop band characteristics.

From the above-mentioned quantities, our theoretical and experimental results are in good agreement. However, the somewhat higher insertion loss in the passband due to the attenuation of whole crosstie slow-wave CPW sections and the discontinuity effects, including radiation loss in the test device, requires further reduction for practical applications.

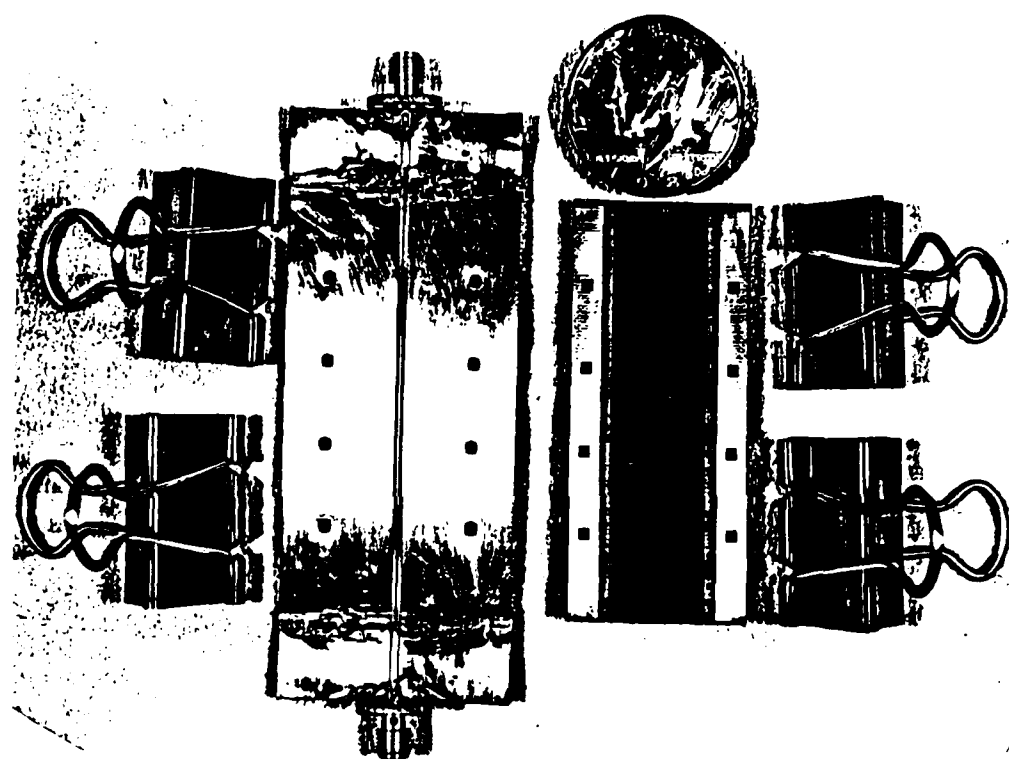


Fig.3.9 Photograph of the disassembled doubly-periodic band-reject grating
in experiment.

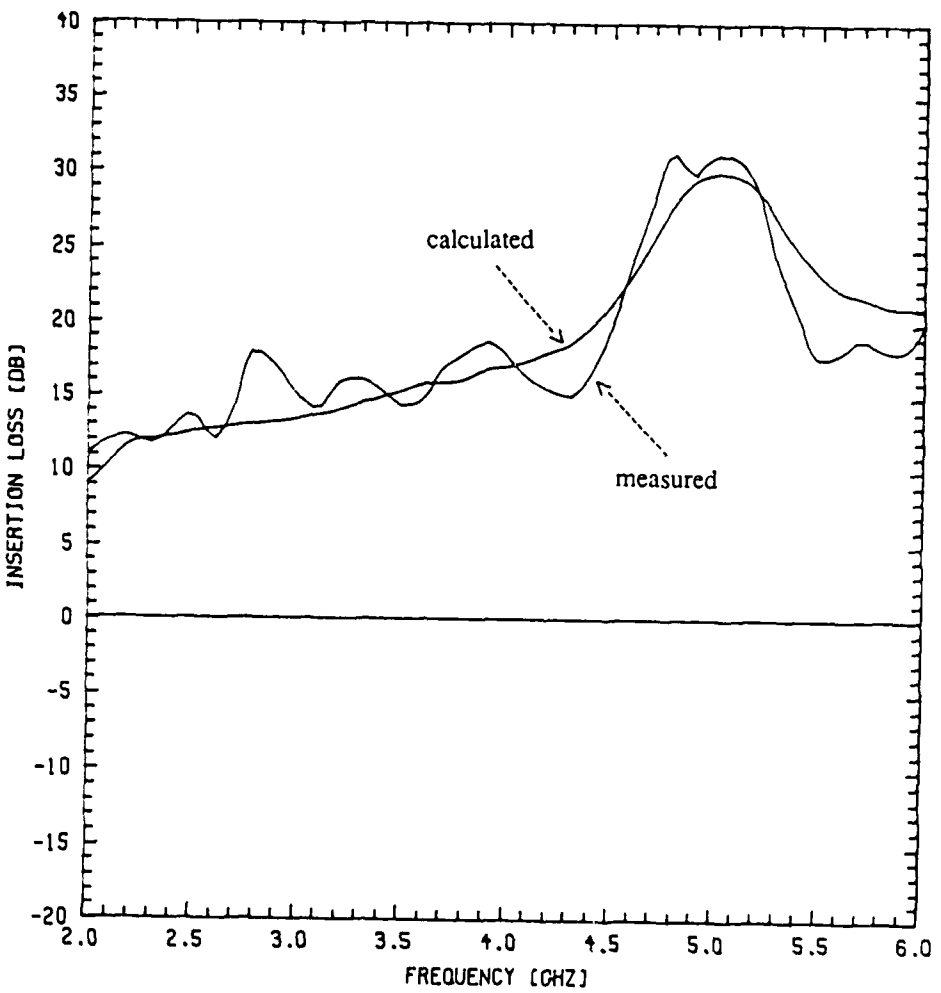


Fig.3.10 Measured and calculated insertion loss for the doubly-periodic band-reject grating.

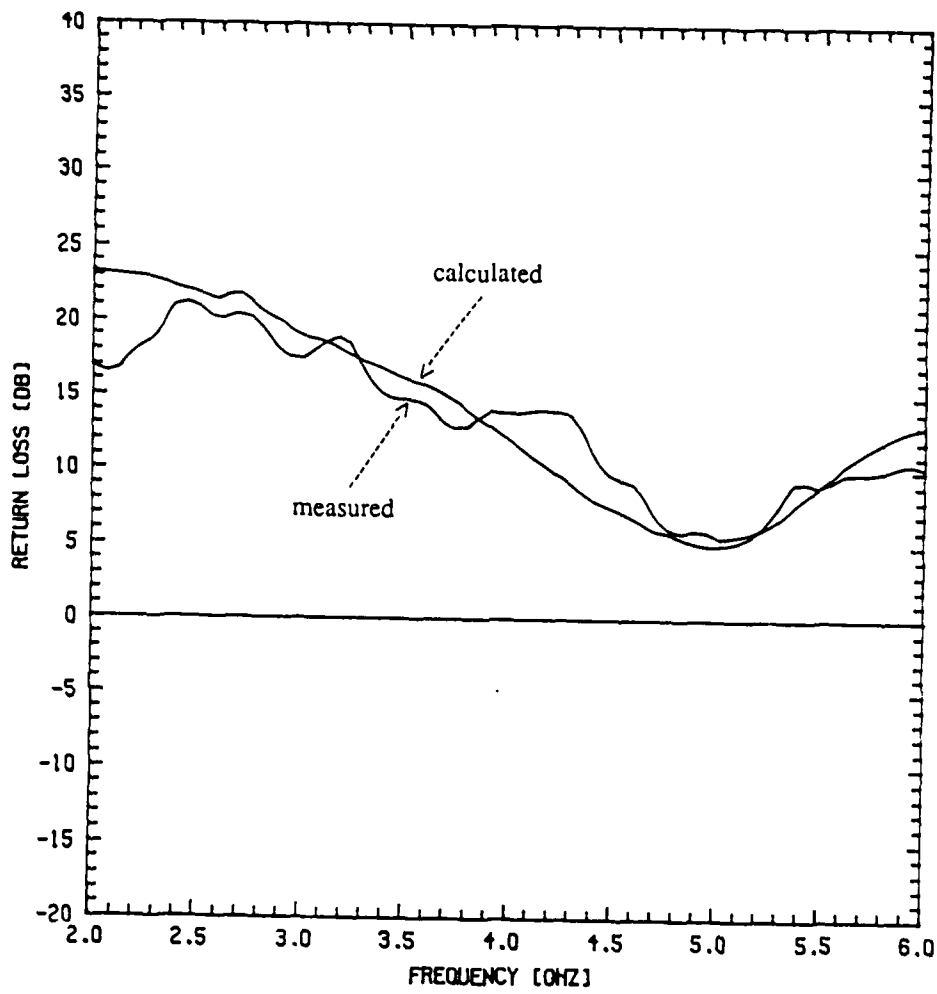


Fig.3.11 Measured and calculated return loss for the doubly-periodic
band-reject grating.

CHAPTER 4 : SLOW-WAVE CHEBYSHEV REFLECTOR DESIGN USING NEW CROSSTIE OVERLAY SLOW-WAVE COPLANAR WAVEGUIDES

Although the frequency-selective band-reject grating created in Chapter 3 can give a strong stopband, their passbands may have ripples which are excessive for many applications. In order to better control the passband ripple at a reasonably low level, we created a slow-wave reflector from the new crosstie overlay CPW's which has a prescribed stopband and also prescribed Chebyshev passbands. Two quarter-wave impedance transformers have been connected to both the input and output ends to facilitate impedance matching with external 50Ω measuring systems. The design procedure is based on a formulation proposed by Cohn [33] for an approximate synthesis of distributed stepped-impedance transformers.

4.1 SYNTHESIS OF SLOW-WAVE CHEBYSHEV REFLECTOR PROTOTYPES

The transmission-line prototype circuit used in the design of a slow-wave Chebyshev reflector is the equal-electrical-length quarter-wave step-impedance filter as shown in Fig.4.1. It is a distributed filter consisting of n cascaded line elements; each element corresponds to a resonator in conventional filter design. The elements, consisting of appropriate lengths of slow-wave structures as shown in Fig.1.4 with the characteristic impedances Z_i ($i=1,2,3,\dots,n$) are assumed to have

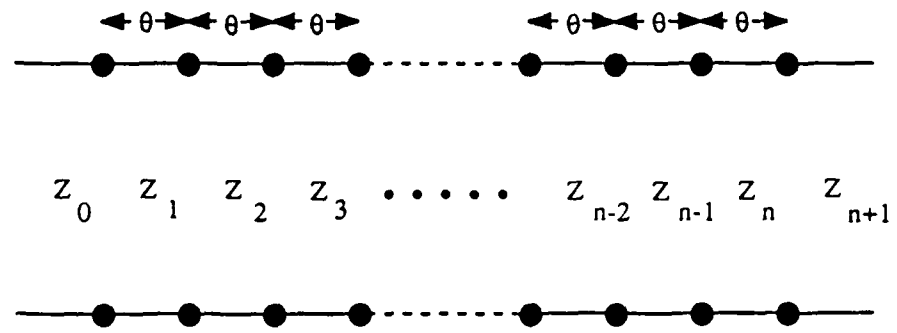


Fig.4.1 Equal-electrical-length step-impedance transmission-line equivalent circuit for slow-wave Chebyshev reflector prototype.

lengths of $L_i = (\lambda_{g0})_i/4$, where $(\lambda_{g0})_i$ is the guide wavelength of the i -th impedance step at the stopband center frequency. The electrical response of this transmission-line structure depends upon the impedances of the unit elements. For electromagnetic waves propagating along the line, the impedance difference between the unit elements yields reflected waves which will accumulate together to cause the band-reject phenomenon to take place at the desired frequencies. Based on Cohn's [33] approximate synthesis procedure for stepped-impedance transformers which considers only the first-order reflection effects, a scheme similar to the one presented in [34] was employed to synthesize a slow-wave Chebyshev reflector prototype with the prescribed characteristics.

Let us regard Fig.4.2 as the attenuation response of the circuit in Fig.4.1. This idealized attenuation response for structures as in Fig.4.1 can be defined in terms of Chebyshev polynomials of degree n , the bandwidth, and the maximum stopband VSWR $S_{max,s}$. The insertion loss (IL) of the circuit in Fig.4.1, if exactly designed for a Chebyshev response, is

$$IL = 10 \log_{10} \left[1 + \frac{\left(S_{max,s} - 1 \right)^2}{4S_{max,s}} \cdot \frac{T_n^2 \left(\frac{\sin \theta}{\sin \theta_1} \right)}{T_n^2 \left(\frac{1}{\sin \theta_1} \right)} \right] \quad (dB) \quad (4.1)$$

where $T_n(x)$ is the Chebyshev polynomial of degree n , $S_{max,s}$ is the maximum stopband VSWR, θ_1 is the electrical length of each section at the lower stopband edge frequency f_1 defined in Fig.4.2, and

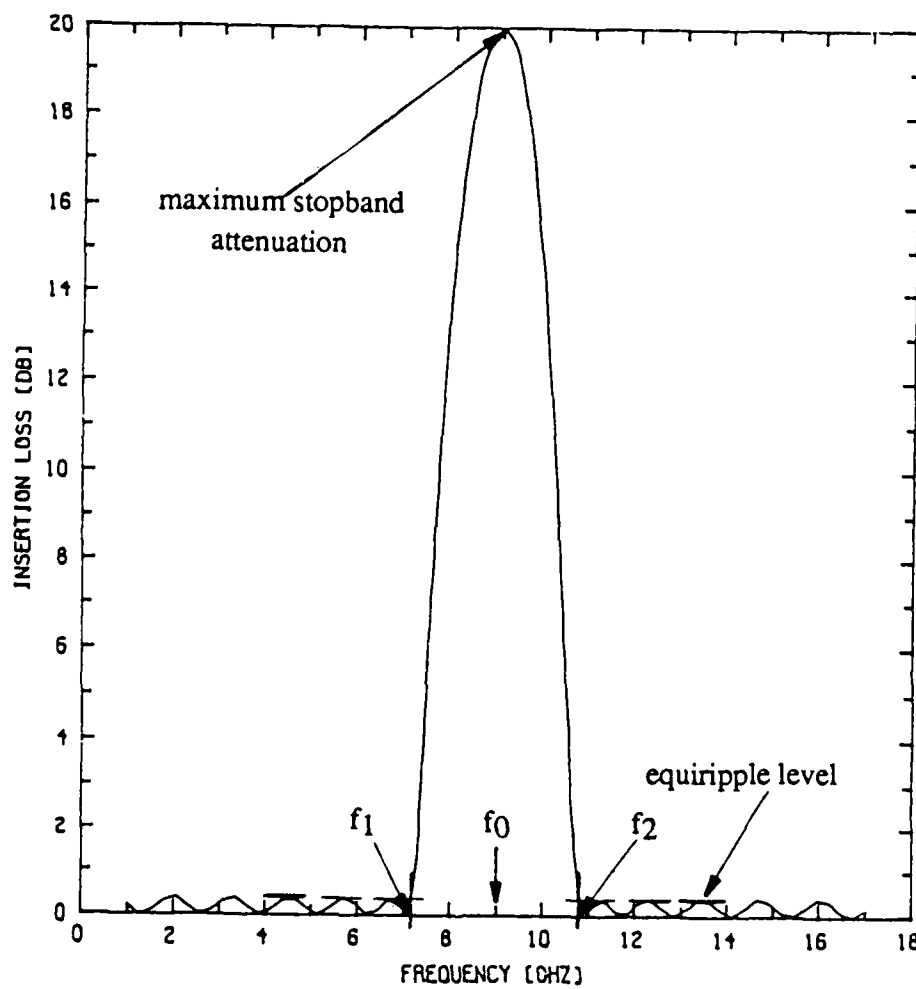


Fig.4.2 Idealized attenuation response for a slow-wave Chebyshev reflector.

$$\theta_1 = \frac{\pi}{2} \cdot \frac{f_1}{f_0}. \quad (4.2)$$

$S_{max,s}$ can be defined as the product of the junction VSWR's

$$S_{max,s} = V_1 V_2 \cdots V_{n+1} \quad (4.3)$$

where V_i is the junction VSWR of the i th junction given by

$$V_i = \left(\frac{Z_i}{Z_{i-1}} \right)^{\pm 1} > 1. \quad (4.4)$$

In this equation, an appropriate sign has to be chosen in order to have V_i greater than one since the Z_i values alternate up and down. Also, θ_1 is related to the equal-ripple bandwidth $(\Delta f)_{er}$ through the bandwidth ratio p

$$p = \frac{f_2}{f_1} = \frac{2 + \frac{(\Delta f)_{er}}{f_0}}{2 - \frac{(\Delta f)_{er}}{f_0}} \quad (4.5)$$

where f_1 and f_2 are the lower and upper stopband edge frequencies, respectively, as shown in Fig.4.2, and

$$(\Delta f)_{er} = \frac{f_2 - f_1}{f_0} \quad (4.6)$$

where f_0 is the center frequency of the stopband. The degree n of the Chebyshev polynomial is the same as the number of sections inserted between the terminating impedances Z_0 and Z_{n+1} in Fig.4.1. We can derive a useful formula for n using $\theta_1, S_{max,s}$, and the maximum passband VSWR denoted by $S_{max,p}$. Calculation of

the insertion loss at $\theta = \theta_1$, using (4.1), gives

$$IL|_{\theta=\theta_1} = 10 \log_{10} \left[\frac{1 + \left(\frac{S_{max,s}-1}{4S_{max,s}} \right)^2}{T_n^2 \left(\frac{1}{\sin \theta_1} \right)} \right] \quad (4.7a)$$

$$= 10 \log_{10} \frac{1}{1 - |\rho_{max,p}|^2} \quad (4.7b)$$

where $|\rho_{max,p}|$ is the magnitude of the maximum passband reflection coefficient and is given by

$$|\rho_{max,p}| = \frac{S_{max,p}-1}{S_{max,p}+1}. \quad (4.8)$$

Equation (4.7b) can also be written in a form similar to (4.7a), that is,

$$IL|_{\theta=\theta_1} = 10 \log_{10} \left(\frac{1 + |\rho_{max,p}|^2}{1 - |\rho_{max,p}|^2} \right). \quad (4.9)$$

After some mathematical manipulation using (4.7a) and (4.9), we finally get the following equation:

$$n = \frac{\cosh^{-1} S}{\cosh^{-1} \left(\frac{1}{\sin \theta_1} \right)} \quad (4.10)$$

where

$$S = \frac{S_{\max,s} - 1}{2\sqrt{S_{\max,s}}} \sqrt{\left(\frac{S_{\max,p} + 1}{S_{\max,p} - 1}\right)^2 - 1}. \quad (4.11)$$

Therefore, if θ_1 , $S_{\max,s}$, and $S_{\max,p}$, or equivalently the fractional bandwidth, the maximum stopband attenuation, and the specified passband ripple size, are given, we can calculate the number of sections to be inserted between the two terminating impedances of Z_0 and Z_{n+1} by the use of (4.10) and (4.11).

Owing to the almost-nondispersive feature of the crosstie overlay slow-wave CPW's, it is noted that the transmission-line prototype having the response given by (4.1) does not include the effects of the stopband-width shrinkage that will occur due to dispersion.

After we have calculated n for given specifications, we need to calculate the junction VSWR's V_i or the normalized section impedances Z_i . For the purpose of an approximate synthesis, as done by Cohn for the case of a step-transformer, we assume that impedance steps are small that the reflection interaction between steps can be neglected in the prototype circuit in Fig.4.2. Then the total reflection coefficient of the reflector prototype referred to at the center of the reflector structure is expressed as follows:

$$\rho = A_1 e^{jn\theta} - A_2 e^{j(n-2)\theta} + \dots + (-1)^n A_{n+1} e^{-jn\theta} \quad (4.12)$$

where the A_i 's are the junction reflection coefficient magnitudes, which are given by

$$A_i = \pm \frac{Z_i - Z_{i-1}}{Z_i + Z_{i-1}} > 0 \quad , \quad \text{for } i=1,2,\dots,n+1. \quad (4.13)$$

The magnitude of the step reflections are assumed to be symmetrical, i.e., $A_1 = A_{n+1}$.

$A_2 = A_n$, etc.. Therefore, for n odd

$$\rho = j \sum_{k=0}^{(n-1)/2} [(-1)^k 2A_{k+1} \sin(n-2k)\theta] \quad (4.14)$$

and for n even

$$\rho = \begin{cases} A_1, & \text{when } n=0 \\ \sum_{k=0}^{(n-2)/2} (-1)^k 2A_{k+1} \cos(n-2k)\theta + (-1)^{n/2} A_{\frac{n+2}{2}}, & \text{when } n \geq 2. \end{cases} \quad (4.15)$$

In order to obtain Chebyshev passbands, ρ in (4.14) or (4.15) is forced to be equal to a Chebyshev polynomial $\alpha T_n(x)$, where α is a constant which need not be explicitly evaluated and

$$x = \frac{\sin\theta}{\sin\theta_1} \quad (4.16)$$

For $n=0, 1$, and 2

$$n=0: \quad \rho = \alpha T_0(x) = \alpha$$

$$= A_1$$

$$\Rightarrow A_1 = \alpha$$

$$n=1: \quad \rho = \alpha T_1(x) = \alpha x$$

$$= j2A_1 \sin\theta = j2A_1 x \sin\theta_1$$

$$\Rightarrow A_1 = \frac{\alpha}{j2 \sin\theta_1}$$

$$\begin{aligned}
 n=2: \quad \rho &= \alpha T_2(x) = \alpha(2x^2 - 1) = 2\alpha x^2 - \alpha \\
 &= 2A_1 \cos 2\theta - A_2 \\
 &= 2A_1(1 - 2x^2 \sin^2 \theta_1) - A_2 \\
 &= -4A_1 x^2 \sin^2 \theta_1 + 2A_1 - A_2 \\
 \Rightarrow A_1 &= -\frac{\alpha}{2 \sin^2 \theta_1}, \quad A_2 = -\frac{\alpha}{\sin^2 \theta_1} + \alpha.
 \end{aligned}$$

We keep going until the desired value of n is reached.

Following the above procedure, we are able to determine the following junction reflection coefficient magnitude ratios:

$$A_1 : A_2 : \dots : A_{n+1} = a_1 : a_2 : \dots : a_{n+1} \quad (4.17)$$

where $a_i = A_i / A_1$. Assuming the impedance steps are small, (4.13) can be written approximately as

$$A_i \approx \pm \frac{1}{2} \ln \frac{Z_i}{Z_{i-1}} > 0. \quad (4.18)$$

Substituting (4.18) into (4.17) and performing some manipulation gives

$$\left| \ln \frac{Z_i}{Z_{i-1}} \right| = \begin{cases} \frac{a_i \left(\ln \frac{Z_1}{Z_0} + \ln \frac{Z_1}{Z_2} + \dots + \ln \frac{Z_n}{Z_{n+1}} \right)}{a_1 + a_2 + \dots + a_{n+1}}, & \text{for } n \text{ odd} \\ \frac{a_i \left(\ln \frac{Z_1}{Z_0} + \ln \frac{Z_1}{Z_2} + \dots + \ln \frac{Z_{n+1}}{Z_n} \right)}{a_1 + a_2 + \dots + a_{n+1}}, & \text{for } n \text{ even} \end{cases}$$

$$\begin{aligned}
 &= \frac{a_i (\ln V_1 + \ln V_2 + \dots + \ln V_{n+1})}{a_1 + a_2 + \dots + a_{n+1}} \\
 &= \frac{a_i \ln(V_1 V_2 \dots V_{n+1})}{a_1 + a_2 + \dots + a_{n+1}} \\
 &= \frac{a_i \ln(S_{\max,s})}{a_1 + a_2 + \dots + a_{n+1}}
 \end{aligned} \tag{4.19}$$

Knowing the a_i by use of the above-mentioned scheme and (4.17), and knowing $S_{\max,s}$, we can then compute all the ratios Z_i/Z_{i-1} by use of (4.19).

As shown above, the normalized impedance of each section is obtained using the first-order approximation, while the number of sections needed is calculated using the exact formula of (4.11). It should be noted that neglecting the higher order reflections in each step as well as the approximation used in (4.18) can introduce some errors in the above designed Z_i/Z_{i-1} ratios. In order to reduce such errors, some modifications have to be made. From (4.1), it can be shown that the input reflection coefficient for an exact Chebyshev bandstop reflector design is

$$\rho_e = \frac{\frac{S_{\max,s}-1}{2\sqrt{S_{\max,s}}} \frac{T_n\left(\frac{\sin\theta}{\sin\theta_1}\right)}{T_n\left(\frac{1}{\sin\theta_1}\right)}}{\sqrt{1 + \frac{(S_{\max,s}-1)^2 T_n^2\left(\frac{\sin\theta}{\sin\theta_1}\right)}{4S_{\max,s} T_n^2\left(\frac{1}{\sin\theta_1}\right)}}} \tag{4.20}$$

The corresponding approximate equation which is consistent with ignoring higher order reflections is

$$\rho_a = \frac{1}{2} \ln(S_{\max,s}) \frac{T_n \left(\frac{\sin \theta}{\sin \theta_1} \right)}{T_n \left(\frac{1}{\sin \theta_1} \right)} \quad (4.21)$$

(Equation (4.21) is analogous to [33, eq.(36)] for the step-transformer case.) A correction was introduced by making the ripple sizes of (4.20) and (4.21) the same at the band edge. By replacing θ_1 with θ_1' in (4.21) and setting $\rho_a|_{\theta=\theta_1'} = \rho_e|_{\theta=\theta_1}$, we get

$$\theta_1' = \sin^{-1} \left[\frac{1}{\cosh \left(\frac{\cosh^{-1} S}{\cosh^{-1} S} \cosh^{-1} \left(\frac{1}{\sin \theta_1} \right) \right)} \right] \quad (4.22)$$

where S is given in (4.11), θ_1 is given in (4.2), and

$$S = \frac{\ln(S_{\max,s})}{S_{\max,p} - 1}. \quad (4.23)$$

Parameter θ_1' calculated using (4.22) is then used in place of θ_1 in (4.16) to generate all the junction reflection coefficients.

Finally, we have to determine the exact length of each line section in order for every section of the reflector to be resonant at the same frequency f_0 (which is the center frequency of the stopband). Referring to Fig.4.1, the length of each line section L_i equals a quarter wavelength at the stopband center frequency f_0 . Hence,

$$\beta_i L_i \Big|_{f=f_0} = \frac{\pi}{2} \quad \text{radians}, \quad i=1,2,\dots,n \quad (4.24)$$

where β_i is the propagation constant of section i at frequency f_0 . Solving (4.24), we obtain the length for each section that bring the entire structure into synchronism at the same frequency f_0 .

4.2 REALIZATION OF A SLOW-WAVE CHEBYSHEV REFLECTOR FROM A TRANSMISSION-LINE PROTOTYPE

Following the procedure depicted in Section 4.1, we have designed a Chebyshev reflector based on crosstie overlay slow-wave CPW's with the following prescribed characteristics :

- .The stopband center frequency=9 GHz
- .The maximum stopband attenuation=20 dB
- .The equiripple level in passbands=0.5 dB
- .The equiripple fractional bandwidth=0.4

After the synthesis of a prototype as shown in Fig.4.1, the number of sections to be inserted between Z_0 and Z_{n+1} is $n=13$. The maximum stopband VSWR is $S_{\max,s}=397.9975$. The maximum passband VSWR is $S_{\max,p}=1.9841$. The junction VSWR's V_i , calculated from (4.19) are shown as follows:

$$V_1=V_{14}=1.8056$$

$$V_2=V_{13}=1.3369$$

$$V_3 = V_{12} = 1.4124$$

$$V_4 = V_{11} = 1.4831$$

$$V_5 = V_{10} = 1.5433$$

$$V_6 = V_9 = 1.5873$$

$$V_7 = V_8 = 1.6105$$

The step impedances of the reflector prototype are:

$$Z_0 = 1.0 \Omega \text{ (input)}$$

$$Z_1 = Z_0 \times V_1 = 1.8056 \Omega$$

$$Z_2 = Z_1 / V_2 = 1.3506 \Omega$$

$$Z_3 = Z_2 \times V_3 = 1.9076 \Omega$$

$$Z_4 = Z_3 / V_4 = 1.2862 \Omega$$

$$Z_5 = Z_4 \times V_5 = 1.9850 \Omega$$

$$Z_6 = Z_5 / V_6 = 1.2506 \Omega$$

$$Z_7 = Z_6 \times V_7 = 2.0140 \Omega$$

$$Z_8 = Z_7 / V_8 = 1.2506 \Omega$$

$$Z_9 = Z_8 \times V_9 = 1.9850 \Omega$$

$$Z_{10} = Z_9 / V_{10} = 1.2862 \Omega$$

$$Z_{11} = Z_{10} \times V_{11} = 1.9076 \Omega$$

$$Z_{12} = Z_{11} / V_{12} = 1.3506 \Omega$$

$$Z_{13} = Z_{12} \times V_{13} = 1.8056 \Omega$$

$$Z_{14} = Z_{13} / V_{14} = 1.0 \Omega \quad (\text{output})$$

As the reflector prototype was obtained, the characteristic impedance of each step was scaled up 12 times to facilitate its realization from the new crosstie overlay slow-wave CPW's. Furthermore, for convenience of measurement, two three-section quarter-wave impedance transformers have been connected to both the input (Z_0) and output (Z_{14}) ends of the reflector so that the problem of impedance matching with external 50Ω measuring systems was eliminated. The designed performances of the quarter-wave impedance transformer are:

.The passband center frequency=9 GHz

.The maximum stopband VSWR=4.167

.The equiripple passband VSWR =1.5

.The equiripple fractional bandwidth=1.0

The characteristic impedance of each impedance step in the quarter-wave impedance transformer was calculated based on Collin's [35] theory as follows:

$$Z_0 = 50 \Omega \quad (\text{input})$$

$$Z_1 = 37.3112 \Omega$$

$$Z_2 = 24.4948 \Omega$$

$$Z_3 = 16.0809 \Omega$$

$$Z_4 = 12.0 \Omega \quad (\text{output}).$$

For a chosen crosstie overlay slow-wave CPW configuration, the propagation constants and the characteristic impedances of each constituent section A (with crosstie strip) and B (without crosstie strip) at the stopband center frequency were calculated by utilizing the spectral domain method. The attenuation constants due to dielectric loss in both sections A and B were assumed negligibly small while the attenuation constants due to ohmic loss were calculated from Wheeler's incremental inductance formula. In the meantime, we assumed that the propagation constants in both sections A and B were not affected by the attenuation due to conductor loss. The information for sections A and B was then used in equation (2.47). The lengths l_A and l_B of the constituent sections A and B for each impedance step were thus determined. It is important that the operating wavelength be sufficiently longer than the period $l (=l_A+l_B)$ of the periodic crosstie overlay CPW so that the structure will simulate a uniform transmission line. Finally, equation (2.43) was used to obtain the guide wavelength at the stopband center frequency ($\lambda_{g0}i$) for each impedance step i , and therefore the length L_i for each impedance step that brings the entire structure into synchronism.

4.3 PRELIMINARY EXPERIMENTAL RESULTS FOR THE SLOW-WAVE CHEBYSHEV REFLECTOR

Referring to Fig.1.4 for experimental simplicity, a monolithic crosstie overlay slow-wave CPW with $s=0.15\text{mm}$, $w=0.745\text{mm}$, $b=0.001\text{mm}$, $h=0.35\text{mm}$, ϵ_r (semi-insulating GaAs, substrate)=12.9, ϵ_r' (Si_3N_4 , dielectric overlay)=6.5 and Au (conductors of CPW and crosstie strips)=0.0015mm has been adopted to serve as the building block of our preliminary slow-wave Chebyshev reflector circuit. Table 4.1 shows details of the values of Z , l_A , l_B and L for each impedance step of the entire circuit. In the experiment which was performed by Texas Instruments Company, Dallas, Texas, first, a CPW pattern was formed by a lift-off technique after a $\text{Ti}/\text{Au}=200\text{\AA}/15000\text{\AA}$ metallic layer was vacuum-evaporated onto a semi-insulating GaAs substrate surface with $\epsilon_r=12.9$ and $h=0.35\text{mm}$ (h is the substrate thickness). The center conductor width of the CPW is $s=0.15\text{mm}$ and the slot width is $w=0.745\text{mm}$. A $1.0\ \mu\text{m}$ thick Si_3N_4 ($\epsilon_r'=6.5$) layer was then coated on the surface of the CPW as the dielectric overlay in a plasma-assisted chemical vapor deposition system. With the same lift-off technique, the metal crossties made of a 15000\AA thick vacuum-evaporated Au layer were finally deposited on the top surface of the Si_3N_4 layer. Fig.4.3(b) is a photograph of the device embedded in a $50\ \Omega$ test jig.

Figs.4.4 and 4.5 show the calculated and the measured insertion loss and return loss, respectively, of the slow-wave Chebyshev reflector. In the calculated curves, the effect of the ohmic loss of the gold conductor (resistivity= $2.35\times 10^{-6}\ \Omega\text{-cm}$) has been included. From these two figures, the center frequency of the stopband is 8.15 GHz in experiment and 8.85 GHz in theory. The difference is about 8%. The

Table 4.1: Detailed information for Z, l_A , l_B and L of the slow-wave Chebyshev reflector and quarter-wave impedance transformers

# of impedance steps lengths	Z (Ω)	l_A (mm)	l_B (mm)	L (mm)
1 (imped. transf.)	37.31	.0039	.0961	1.4
2 (")	24.50	.0093	.0907	1.0
3 (")	16.08	.0199	.0801	0.7
4 (input section)	12.00	.0312	.0688	0.6
5 (Cheby. reflec.)	21.67	.0118	.0882	0.9
6 (")	16.21	.0197	.0803	0.7
7 (")	22.89	.0106	.0894	0.9
8 (")	15.43	.0213	.0787	0.7
9 (")	23.82	.0099	.0901	1.0
10(")	15.01	.0223	.0777	0.7
11(")	24.17	.0096	.0904	1.0
12(")	15.01	.0223	.0777	0.7
13(")	23.82	.0099	.0901	1.0
14(")	15.43	.0213	.0787	0.7
15(")	22.89	.0106	.0894	0.9
16(")	16.21	.0197	.0803	0.7
17(")	21.67	.0118	.0882	0.9
18 (output section)	12.00	.0312	.0688	0.6
19 (imped. transf.)	16.08	.0199	.0801	0.7
20(")	24.50	.0093	.0907	1.0
21(")	37.31	.0039	.0961	1.4

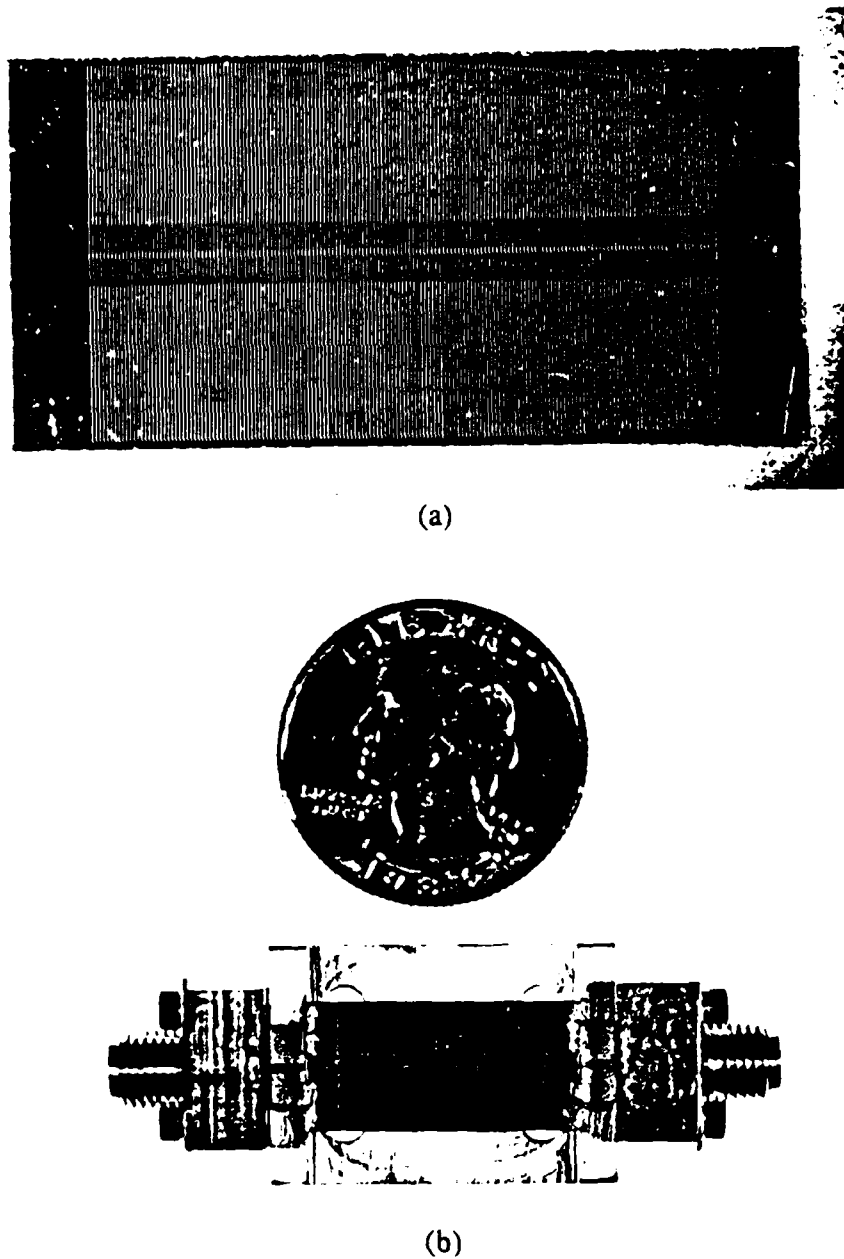


Fig.4.3 Photograph of the slow-wave Chebyshev reflector. (a) Device chip,
(b) Device and test jig.

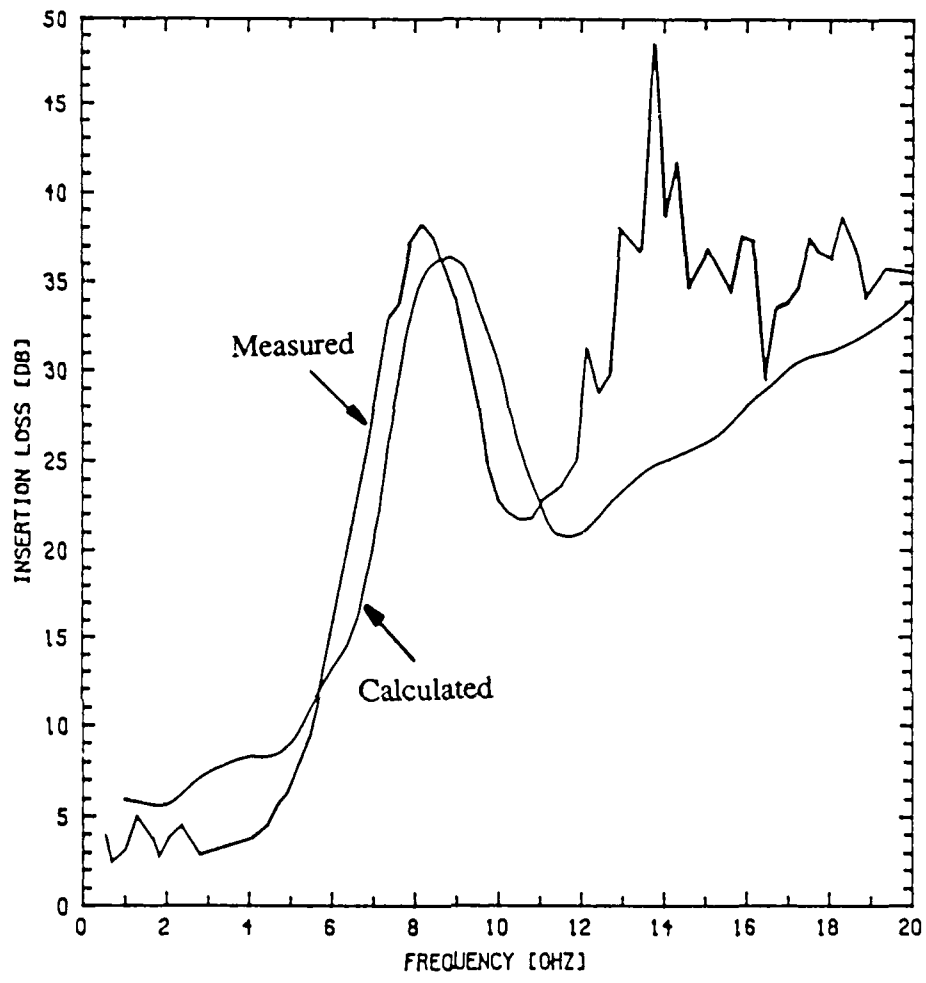


Fig.4.4 Insertion loss of the preliminary slow-wave Chebyshev reflector.

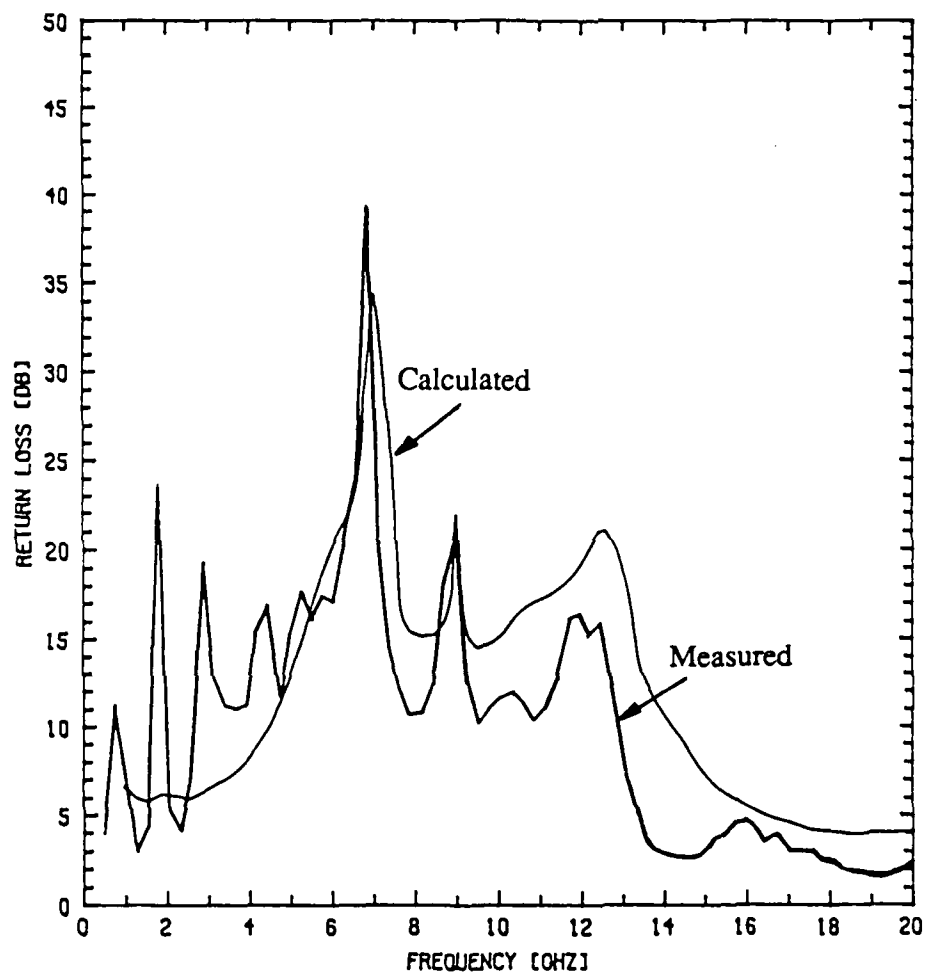


Fig.4.5 Return loss of the preliminary slow-wave Chebyshev reflector.

difference is caused not only by the errors in fabrication but also by the fact that the high order reflections in each impedance step were not taken into account in the calculation of each junction's VSWR. The peak insertion loss in the stopband is 38 dB from the experiment and 35.5 dB from theory. The minimum return loss in the stopband is 11 dB from the experiment and 15 dB from theory. The poor return loss inside the passband comes from the narrow-bandwidth impedance transformers. The slow-wave factor of this reflector at the stopband center frequency is about 10.5. The physical and electrical lengths of the slow-wave reflector are 10.8mm and 19.99 radian, respectively. From the above discussion, our theoretical and experimental results agree reasonably well. However, the detrimental ohmic loss diminishes the usefulness of the reflector. In order to reduce the ohmic loss of the circuit so that a higher Q value can be obtained, a modified crosstie overlay slow-wave CPW is proposed and examined in the following section.

4.4 A MODIFIED CROSSTIE OVERLAY SLOW-WAVE COPLANAR WAVEGUIDE AND ITS APPLICATION TO A NEW SLOW-WAVE CHEBYSHEV REFLECTOR

Although the transmission and reflection characteristic measurements of the slow-wave reflector presented in the last section indicate that a band-reject phenomenon was confirmed, a somewhat high ohmic loss due to the large skin current densities on the surface of the crosstie strips and the center conductor of the

CPW caused degradation of the reflector's performance. In order to reduce ohmic loss to an acceptable level, a modification of the slow-wave CPW presented in Fig.1.4 has been made based on a mechanism similar to that described in [36] which is proposed as the new building block of slow-wave reflector circuits. Figure 4.6 is the schematic of the modified crosstie overlay slow-wave CPW. As shown in Fig.4.6, the same modification can also be applied to the microstrip version. Instead of using a thin dielectric overlay to generate a cascaded chain of large capacitive and inductive sections, a much thicker dielectric overlay and modulated cross-sectional configurations of CPWs in the constituent sections A and B are adopted herein. Since the slow-wave factor in the periodic crosstie overlay CPW mainly depends on $\sqrt{Z_B/Z_A}$ (Z_A and Z_B are the characteristic impedances of the constituent sections A and B, respectively), the large value of the slow-wave factor will be maintained in spite of a much thicker dielectric overlay if different cross-sectional configurations of the CPW in sections A and B are appropriately chosen. The spatial separation of electric and magnetic energies is not changed while the skin current densities flowing on the crosstie strips and center conductor of CPW are reduced. It is conceivable that the new slow-wave reflector proposed here should be able to provide a reasonably short physical length as well as a lower level of attenuation inside the passbands. This is useful for implementation of a possible high-Q circuit in passive monolithic microwave and millimeter-wave integrated circuits.

4.5 PREDICTED CHARACTERISTICS OF THE NEW SLOW-WAVE CHEBYSHEV REFLECTOR

As Fig.4.6 shows, a modified crosstie overlay slow-wave CPW with

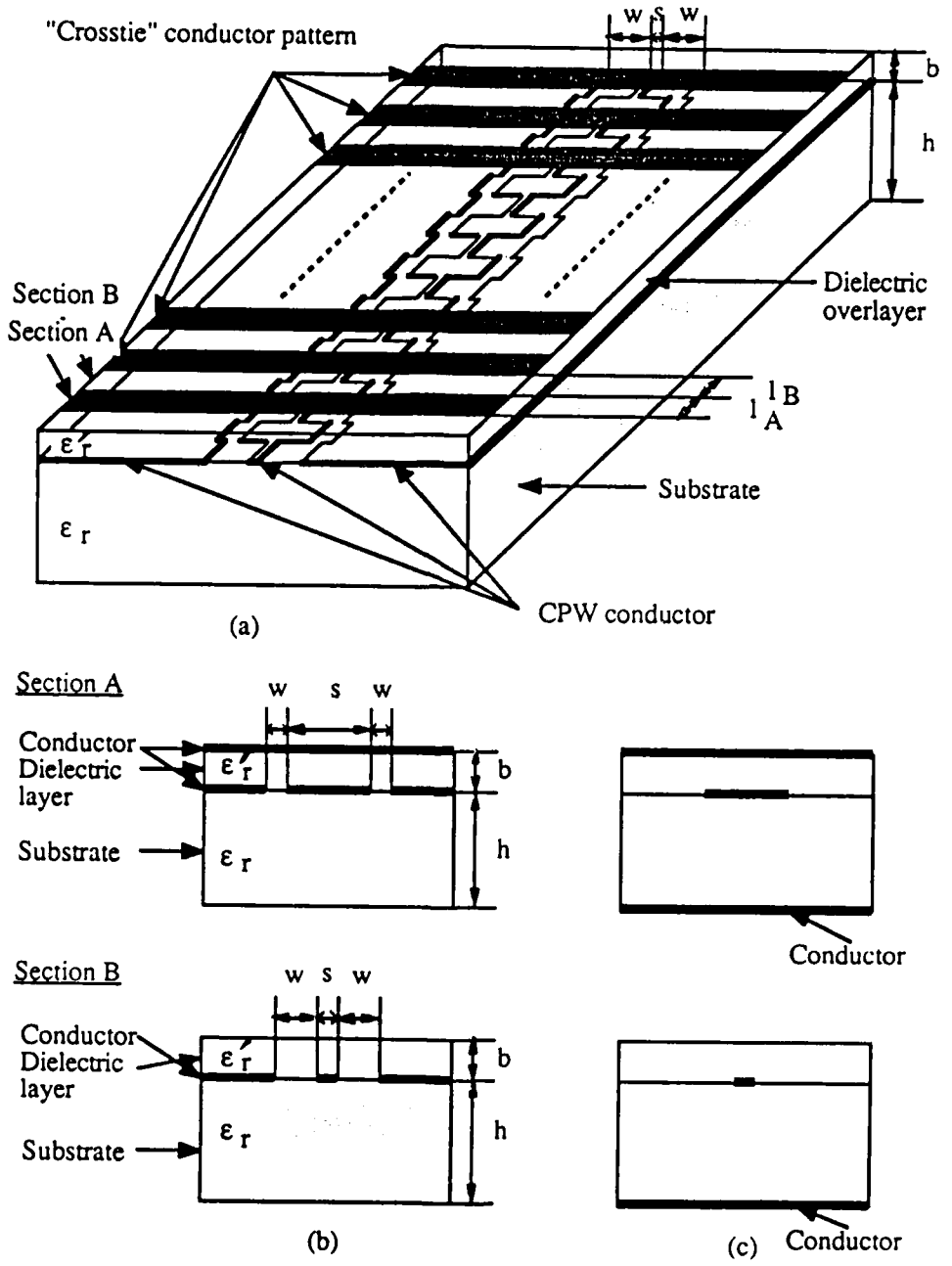


Fig.4.6 Modified crosstie overlay CPW and microstrip slow-wave structures.

(a) CPW, (b) Cross-section of CPW, (c) Cross-section of microstrip.

$s_A=3.0\text{mm}$, $w_A=0.2\text{mm}$, $s_B=0.1\text{mm}$, $w_B=1.6\text{mm}$, $b=0.02\text{mm}$, $h=0.254\text{mm}$, $\epsilon_r=9.7$ (alumina), $\epsilon_r'=3.5$ (polyimide), $\text{Au}=0.004\text{mm}$ is selected as the new building block of our slow-wave Chebyshev reflector circuit. The prescribed characteristics are as follows:

- .The stopband center frequency=5 GHz
- .The maximum stopband attenuation=10 dB
- .The equiripple level in passbands=0.5 dB
- .The equiripple fractional bandwidth=0.25.

After the synthesis of the circuit, the number of required impedance steps is 15. Table 4.2 presents the details of the values of Z , l_A , l_B and L for each impedance step. Fig.4.7 and Fig.4.8 show the predicted insertion loss and return loss, respectively, of the new slow-wave Chebyshev reflector. As Fig.4.7 shows, a somewhat higher ripple size (about 3-4 dB) in the upper passband due to conductor loss could be further reduced by appropriate adjustment of the CPW cross-sectional configuration and dielectric overlay thickness. Fig.4.9 and Fig.4.10 show the real and the imaginary parts, respectively, of the input impedance of the new slow-wave reflector. The load impedance connected to the output end of the reflector is 13Ω . The slow-wave factor of this reflector is about 9. The physical and electrical lengths of the new slow-wave reflector are 24.1mm and 23.46 radian, respectively.

Table 4.2: Detailed information for Z, l_A, l_B and L of the modified slow-wave Chebyshev reflector

# of impedance steps	impedances & lengths	Z (Ω)	l _A (mm)	l _B (mm)	L (mm)
1		21.90	.0227	.0773	1.7
2		18.91	.0284	.0716	1.5
3		22.27	.0221	.0779	1.7
4		18.63	.0291	.0709	1.5
5		22.55	.0216	.0784	1.7
6		18.45	.0295	.0705	1.5
7		22.70	.0214	.0786	1.7
8		18.39	.0296	.0704	1.5
9		22.70	.0214	.0786	1.7
10		18.45	.0295	.0705	1.5
11		22.55	.0216	.0784	1.7
12		18.63	.0291	.0709	1.5
13		22.27	.0221	.0779	1.7
14		18.91	.0284	.0716	1.5
15		21.90	.0227	.0773	1.7

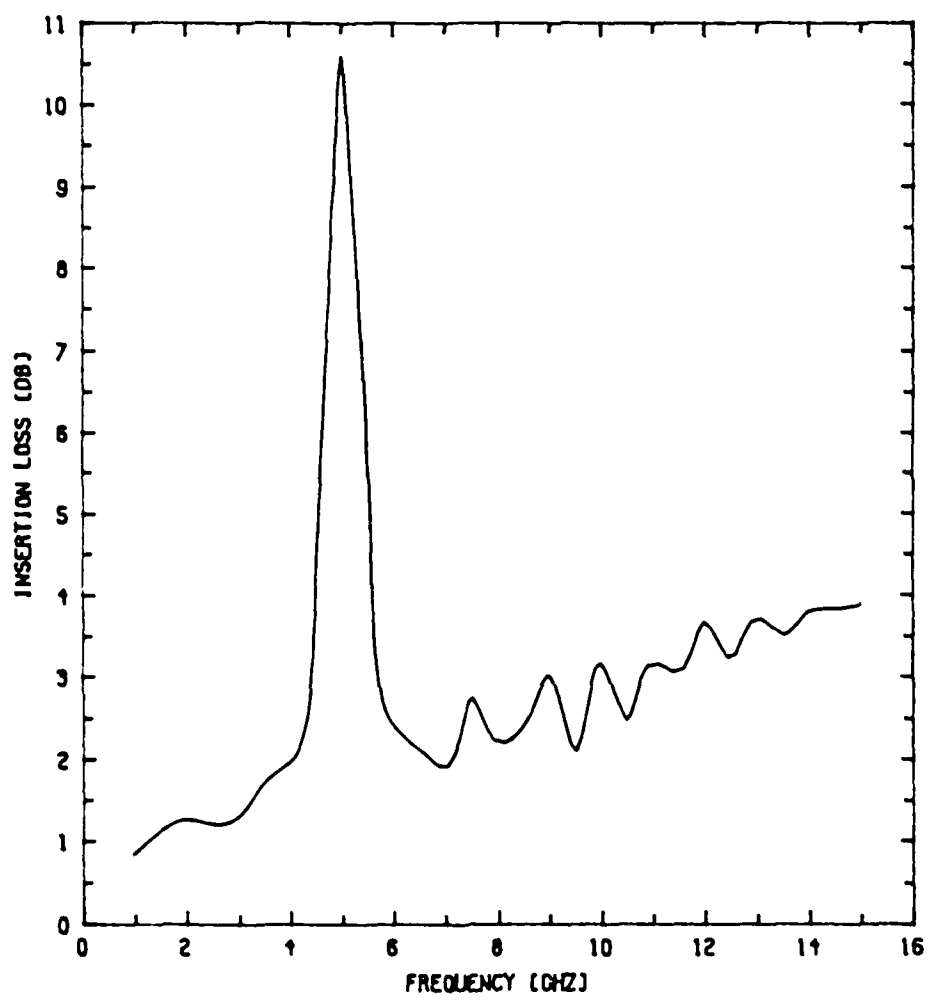


Fig.4.7 Predicted insertion loss of the modified slow-wave Chebyshev reflector.

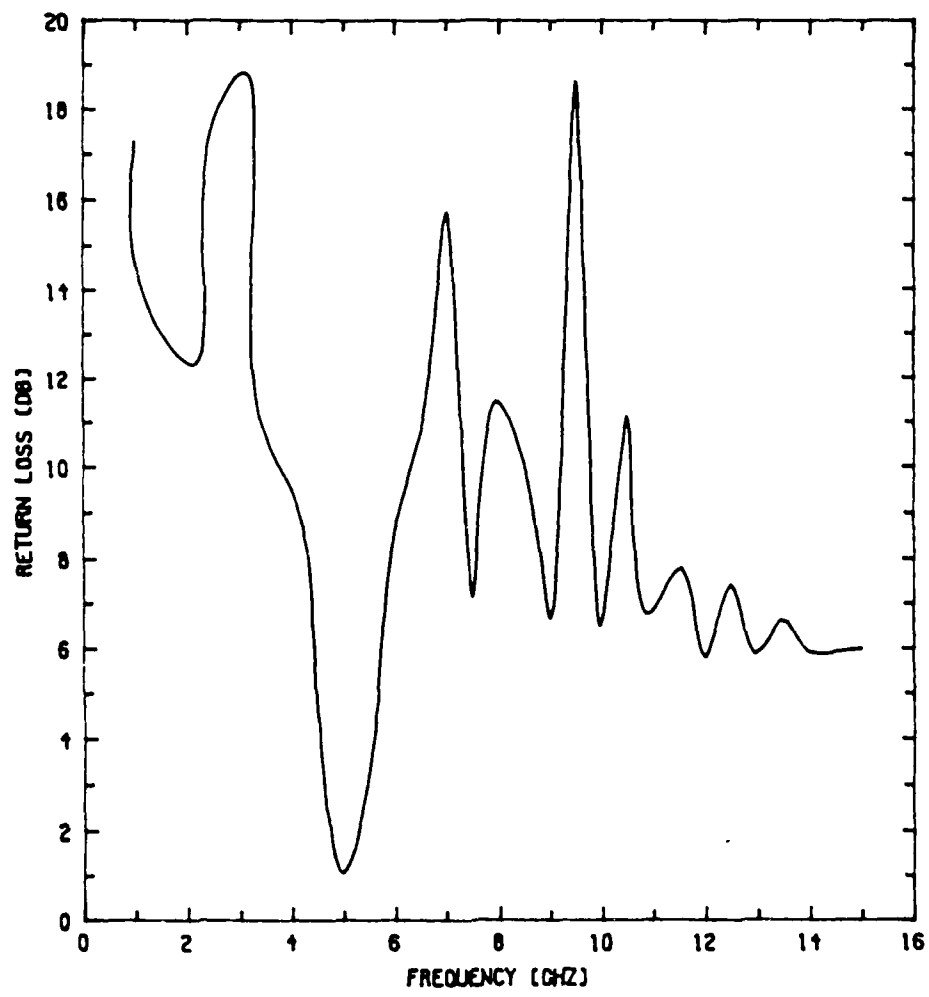


Fig.4.8 Predicted return loss of the modified slow-wave Chebyshev reflector.

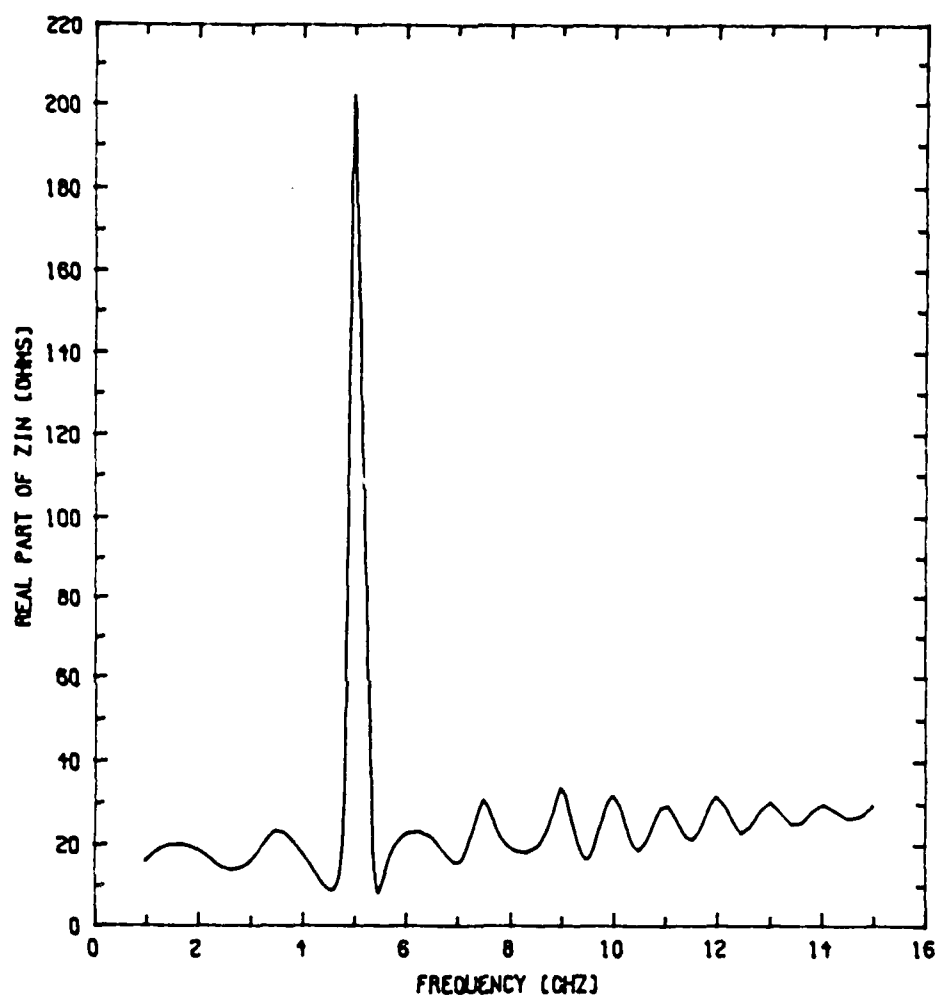


Fig.4.9 Real part of the input impedance of the modified slow-wave Chebyshev reflector.

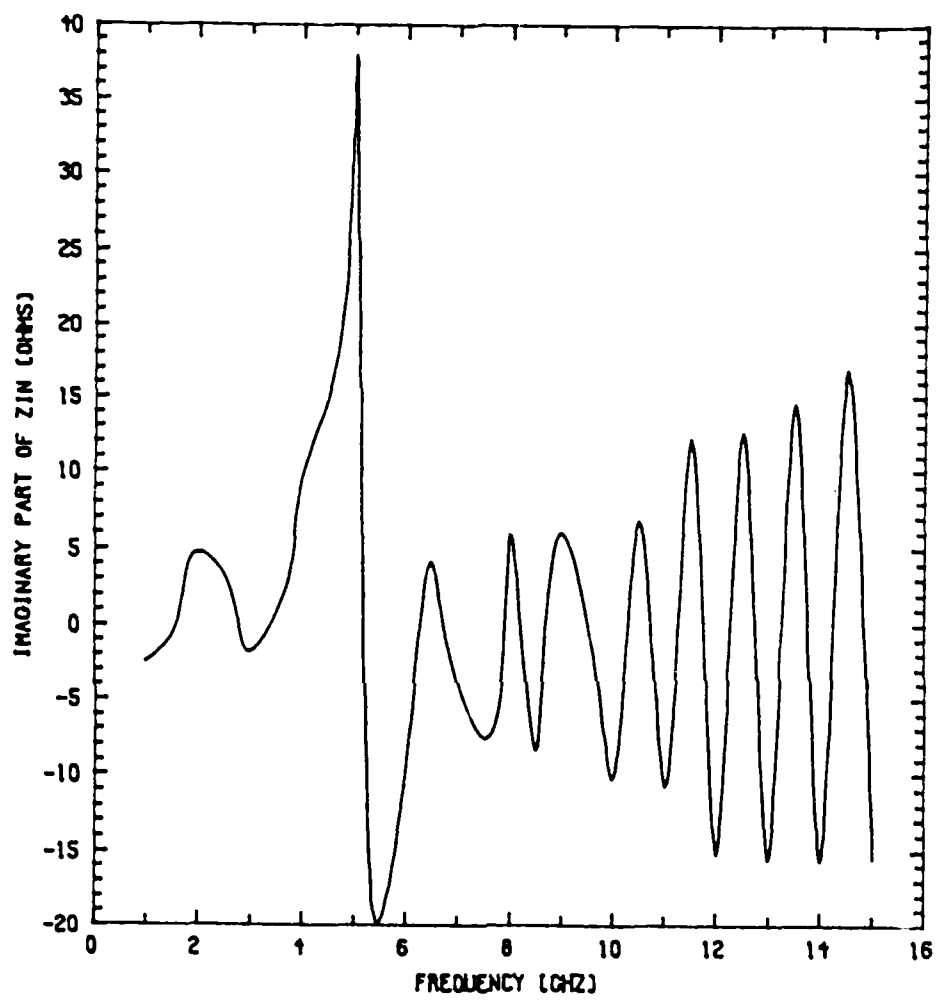


Fig.4.10 Imaginary part of the input impedance of the modified slow-wave Chebyshev reflector.

CHAPTER 5 : CONCLUSIONS

5.1 ACHIEVEMENTS

As a new slow-wave structure for monolithic microwave and millimeter-wave integrated circuits, a crosstie overlay coplanar waveguide was proposed. The ease of fabrication, freedom from dielectric loss, and the feasibility of combining it with other slow-wave mechanisms make it more adaptable for monolithic integration. Similar advantages can also be found in the counterpart microstrip version. The slow-wave propagation along this new structure has been investigated both theoretically and experimentally. The slow-wave factor observed agrees reasonably well with the theoretical prediction. From both results, slow-wave propagation with linear dispersion was conceived. Based on the new slow-wave structure in which the guide wavelength is very small, compact grating structures are found for use as a frequency-selective distributed Bragg reflector (DBR). A doubly-periodic band-reject grating has been created from the DBR's and the band-reject phenomenon was observed as predicted. In order to improve the passband characteristics of the band-reject grating, a monolithic slow-wave Chebyshev reflector was designed and fabricated. Agreement between theory and preliminary experiment has been confirmed. Based on this theory, a new slow-wave reflector with improved characteristics is proposed and examined. A respectable slow-wave factor and a drastic reduction of conductor loss have been obtained. From this work, the proposed new crosstie overlay slow-wave structures are believed to be potentially useful for miniaturization of distributed circuits in GaAs MMIC's, although the

minimization of circuit loss requires further optimization.

5.2 SUGGESTIONS FOR FUTURE RESEARCH

In future research, the new crosstie overlay slow-wave structures are suitable for a number of applications. For instance, (1) By the use of the frequency-selective reflection properties of the band-reject grating, two of the gratings separated by an appropriate distance could be employed as a resonator. Alternatively, two band-reject reflectors can be combined with a 3-dB hybrid to produce a bandpass reflector. (2) A new version of a distributed Bragg reflector (DBR) Gunn oscillator [37] with an intrinsic leaky-wave antenna in a planar circuit form can also be realized from the exploitation of the surface stop band and the leaky-wave stop band of the new crosstie band-reject grating. In addition, if it were possible to incorporate the Schottky slow-wave mechanism as an electronic phase shifter [38] in the grating section, it would be possible to tune the oscillation frequency of the device electronically. This is because in such a grating the propagation constant β can be controlled by the phase shifter, and hence the stopband of the grating can be shifted [39]. (3) In the new crosstie overlay slow-wave CPW's, the propagation constant β and the characteristic impedance Z are approximately proportional to $\sqrt{Z_B/Z_A}$ and $\sqrt{Z_A Z_B}$, respectively. We can thus readily enhance the propagation constant β while maintaining a given characteristic impedance Z . This property can be effectively applied to achieve the simultaneous matching of the phase and the impedance, which is required in the optimum design of traveling-wave electro-optical modulators. Furthermore, the modulation bandwidth of these devices can be very wide due to the

inherently almost-nondispersive properties of the proposed new crosstie overlay slow-wave structures.

BIBLIOGRAPHY

1. R. A. Pucel, "Design considerations for monolithic microwave circuits," IEEE Trans. Microwave Theory Tech., vol.MTT-29, pp.513-534, 1981.
2. H. Hasegawa, M. Furukawa and H. Yanai, "Properties of microstrip line on Si-SiO₂ system," IEEE Trans. Microwave Theory Tech., vol.MTT-19, pp.869-881, 1971.
3. Y. Fukoka, Y. -C. Shih and T. Itoh, "Analysis of slow-wave coplanar waveguide for monolithic integrated circuits," IEEE Trans. Microwave Theory Tech., vol.MTT-31, pp.567-573, 1983.
4. V. M. Hietala, J. R. Kwon and K. S. Champlin, "Propagation on microstructure MIS transmission line on silicon," Millimeter-wave/Microwave Measurements and Standards for Miniaturized Systems Conference, Huntsville, AL, Nov.6-7, 1986.
5. C. M. Krown and R. E. Neidert, "Slow wave monolithic variable phase shifter," 10th Int. Conf. Infrared and Millimeter Waves, Lake Buena Vista, FL, Dec.9-13, 1985, pp.275-276.
6. P. Cheung, D. Fun, D. Miller, C. -K. C. Tzuang, D. P. Neikirk and T. Itoh, "Optically controlled coplanar waveguide millimeter wave phase shifter," 10th Int. Conf. Infrared and Millimeter Waves, Lake Buena Vista, FL, Dec.9-13, 1985, pp.303-304.
7. Y. Fukuoka and T. Itoh, "Slow-wave coplanar waveguide on periodically doped

- semiconductor substrate," IEEE Trans. Microwave Theory Tech., vol.MTT-31, pp.1013-1017, 1983.
8. S. Seki and H. Hasegawa, "Cross-tie slow-wave coplanar waveguide on semi-insulating GaAs substrates," Electronics Letters, vol.17, no.25, pp.940-941, Dec.10, 1981.
9. E. M. Bastida, G. P. Donzelli and N. Fanelli, "Slow-wave approach for monolithic GaAs IC's," 1982 IEEE Microwave and Millimeter-wave Monolithic Circuit Symposium, Dallas, TX, June 18, 1982, pp.23-24.
10. T. Itoh, "Application of gratings in a dielectric waveguide for leaky-wave antennas and band-reject filters," IEEE Trans. Microwave Theory Tech., vol.MTT-25, pp.1134-1138, 1977.
11. M. Tsutsumi, T. Ohira, T. Yamaguchi and N. Kumagai, "Reflection of millimeter waves by a corrugated dielectric slab waveguide," Proceedings of IEEE, vol.68, June 1980, pp.733-734.
12. T. Itoh and F. Hsu, "Distributed Bragg reflector Gunn oscillators for dielectric millimeter-wave integrated circuits," IEEE Trans. Microwave Theory Tech., vol.MTT-27, pp.514-518, 1979.
13. M. Riazat, I. Zubeck, S. bandy and G. Zdasiuk, "Coplanar waveguides used in 2-18 GHz distributed amplifier," 1986 IEEE MTT-s Int. Microwave Symp. Digest, pp.337-338.

14. T. Itoh, "Spectral domain immittance approach for dispersion characteristics of generalized printed transmission lines," IEEE Trans. Microwave Theory Tech., vol.MTT-28, pp.733-736, 1980.
15. T. Itoh and R. Mittra, "Spectral-domain approach for calculating the dispersion characteristics of microstrip lines," IEEE Trans. Microwave Theory Tech., vol.MTT-21, pp.496-499, 1973.
16. T. Itoh and R. Mittra, "Dispersion characteristics of slot lines," Electronics Letters, vol.7, no.13, pp.364-365, 1971.
17. J. B. Knorr and K. Kuchler, "Analysis of coupled slots and coplanar strips on dielectric substrate," IEEE Trans. Microwave Theory Tech., vol.MTT-23, pp.541-548, 1975.
18. R. H. Jansen, "High-speed computation of single and coupled microstrip parameters including dispersion, high-order modes, loss and finite strip thickness," IEEE Trans. Microwave Theory Tech., vol.MTT-26, pp.75-82, 1978.
19. G. I. Zysman and D. Varon, "Wave propagation in microstrip transmission lines," 1969 IEEE MTT-s Int. Microwave Symp. Digest, pp.3-9.
20. R. F. Harrington, Time-Harmonic Electromagnetic Fields (New York: McGraw-Hill, 1961).
21. H. Meinel and B. Rembold, "New millimeter wave fin-line attenuators and switches," 1979 IEEE MTT-s Int. Microwave Symp. Digest, pp.249-252.

22. P. J. Meier, "Integrated fin-line millimeter components," IEEE Trans. Microwave Theory Tech., vol.MTT-22, pp.1209-1216, 1974.
23. R. H. Jansen, "Unified user oriented computation of shielded, covered and open planar microwave and millimeter-wave transmission line characteristics," Microwaves, Opt. Acoust., vol.MOA-1, pp.14-22, January 1979.
24. R. Mittra and S. W. Lee, Analytical Techniques in the Theory of Guided Waves (New York: Macmillan, 1971), pp.4-11.
25. L. P. Schmidt and T. Itoh, "Spectral domain analysis of dominant and high order modes in fin-lines," IEEE Trans. Microwave Theory Tech., vol.MTT-28, pp.981-985, 1980.
26. R. E. Collin, Foundations for microwave engineering (New York: McGraw-Hill, 1972), pp.179-181.
27. H. A. Wheeler, "Formulas for the skin effect," Proceedings of IRE, vol.30, 1942, pp.412-424.
28. R. A. Pucel, et al., "Losses in microstrip," IEEE Trans. Microwave Theory Tech., vol.MTT-16, pp.342-350, 1968. Also see correction in IEEE Trans. Microwave Theory Tech., vol.MTT-16, pp.1064, 1968.
29. G. Ghione and C. U. Naldi, "Coplanar waveguides for MMIC applications: Effect of upper shielding, conductor backing, finite-extend ground planes, and line-to-line coupling," IEEE Trans. Microwave Theory Tech., vol.MTT-35, pp.260-267, 1987.

30. K. C. Gupta, R. Garg and I. J. Bahl, Microstrip lines and slotlines (Artech House, 1979), pp.277-280.
31. R. E. Collin, Foundations for Microwave engineering (New York: McGraw-Hill, 1972), pp.381-383.
32. S. T. Peng, J. M. Dong and L. M. Wang, "Wave interaction in doubly periodic structures," 1985 IEEE MTT-s Int. Microwave Symp. Digest, pp.131-134.
33. S. B. Cohn, "Optimum design of stepped transmission-line transformers," IRE Trans. Microwave Theory Tech., vol.MTT-3, pp.16-21, 1955.
34. D. C. Park, G. L. Matthaei and M. S. Wei, "Bandstop filter design using a dielectric waveguide grating," IEEE Trans. Microwave Theory Tech., vol.MTT-33, pp.693-702, 1985.
35. R. E. Collin, "Theory and design of wide-band multisection quarter-wave transformers," Proceedings of IRE, vol.43, pp.179-185, 1955.
36. E. M. Bastida and G. P. Donzelli, "Periodic slow-wave low-loss structures for monolithic GaAs microwave circuits," Electron. Letters, vol.15, no.19, pp.581-582, 1979.
37. B. S. Song and T. Itoh, "Distributed Bragg reflection dielectric waveguide oscillators," IEEE Trans. Microwave Theory Tech., vol.MTT-27, pp.1019-1022, 1979.
38. H. Jacobs and M. M. Chrepta, "Electronic phase shifter for millimeter-wave

semiconductor dielectric integrated circuits," IEEE Trans. Microwave Theory Tech., vol.MTT-22, pp.411-417, 1974.

39. T. Itoh and A. S. Hebert, "Simulation study of electronically scannable antennas and tunable filters integrated in a quasi-planar dielectric waveguide," presented at the IEEE Int. Microwave Symp., Ottawa, Ont. Canada, June 1978.

END

DATE

FILMED

8-88

DTIC